Phase transformations in cast duplex stainless steels

by

Yoon-Jun Kim

A dissertation submitted to the graduate faculty

in partial fulfillment of the requirements for the degree of

DOCTOR OF PHILOSOPHY

Major: Materials Science and Engineering

Program of Study Committee:
L. Scott Chumbley, Co-major Professor
Brian Gleeson, Co-major Professor
Alan M. Russell
Matthew J. Kramer
Frank E. Peters

Iowa State University

Ames, Iowa

2004

Graduate College
Iowa State University

This is to certify that the doctoral dissertation of

Yoon-Jun Kim

has met the dissertation requirements of Iowa State University

Co-major Professor

Co-major Professor

For the Major Program

TABLE OF CONTENTS

ABSTRACT

Duplex stainless steels (DSS) constitute both ferrite and austenite as a matrix. Such a microstructure confers a high corrosion resistance with favorable mechanical properties. However, intermetallic phases such as sigma (σ) and chi (χ) can also form during casting or high-temperature processing and can degrade the properties of the DSS. This research was initiated to develop time-temperature-transformation (TTT) and continuous-cooling-transformation (CCT) diagrams of two types of cast duplex stainless steels, CD3MN (Fe-22Cr-5Ni-Mo-N) and CD3MWCuN (Fe-25Cr-7Ni-Mo-W-Cu-N), in order to understand the time and temperature ranges for intermetallic phase formation. The alloys were heat treated isothermally or under controlled cooling conditions and then characterized using conventional metallographic methods that included tint etching, and also using electron microscopy (SEM, TEM) and wavelength dispersive spectroscopy (WDS). The kinetics of intermetallic-phase ($\sigma + \chi$) formation were analyzed using the Johnson-Mehl-Avrami (JMA) equation in the case of isothermal transformations and a modified form of this equation in the case of continuous cooling transformations. The rate of intermetallic-phase formation was found to be much faster in CD3MWCuN than CD3MN due mainly to differences in the major alloying contents such as Cr, Ni and Mo. To examine in more detail the effects of these elements of the phase stabilities, a series of eight steel castings was designed with the Cr, Ni and Mo contents systematically varied with respect to the nominal composition of CD3MN. The effects of varying the contents of alloying additions on the formation of intermetallic phases were also studied computationally using the commercial thermodynamic software package, *Thermo-Calc*. In general, σ was stabilized with increasing Cr addition and

χ by increasing Mo addition. However, a delicate balance among Ni and other minor elements such as N and Si also exists. Phase equilibria in DSS can be affected by local composition fluctuations in the cast alloy. This may cause discrepancy between thermodynamic prediction and experimental observation.

CHAPTER 1: GENERAL INTRODUCTION

Duplex stainless steels (DSS) constitute a set of steels possessing a nearly equal amount of the ferrite (δ-Fe) and austenite (γ-Fe) phases as a matrix. Commercial duplex stainless steels originated in 1933 when the J. Holtzer Company, a French firm, mistakenly made an alloy containing 20%Cr-8%Ni-2.5%Mo rather than the target alloy of 18%Cr-9%Ni-2.5%Mo. Upon investigation of the new alloy, which consisted of a high volume fraction of ferrite in an austenite matrix, it was found that it possessed high intergranular corrosion resistance under various environments. Firms in other countries, such as Sweden and the United States, started to research and produce DSS beginning from the 1940's.

The austenite+ferrite matrix is attainable by combining various phase stabilizing elements. Cr and Mo are effective ferrite stabilizers, producing a wide ferrite field in phase diagrams. In general, stainless steels having ferrite as the predominant phase have excellent corrosion resistance due to the high solubility of Cr in ferrite. On the other hand, Ni and N, which are effective austenite stabilizers, increase the austenite region in Fe-based systems and are known to improve mechanical properties. Thus, a structure including high Cr, Mo, Ni and N will produce a favorable combination of mechanical properties and high corrosion resistance. The effect produced by these alloying elements on corrosion resistance is indicated by the pitting resistance equivalent number (*PREN*) as shown in Eq. 1. The higher the *PREN* the better the predicted corrosion properties of a DSS. Alloys having a *PREN* greater than 40 are categorized as superduplex grade DSS (Fig. 1).

$$PREN = \%Cr + 3.3 \times \%Mo + 17 \times \%N \qquad \text{Eq. 1}$$

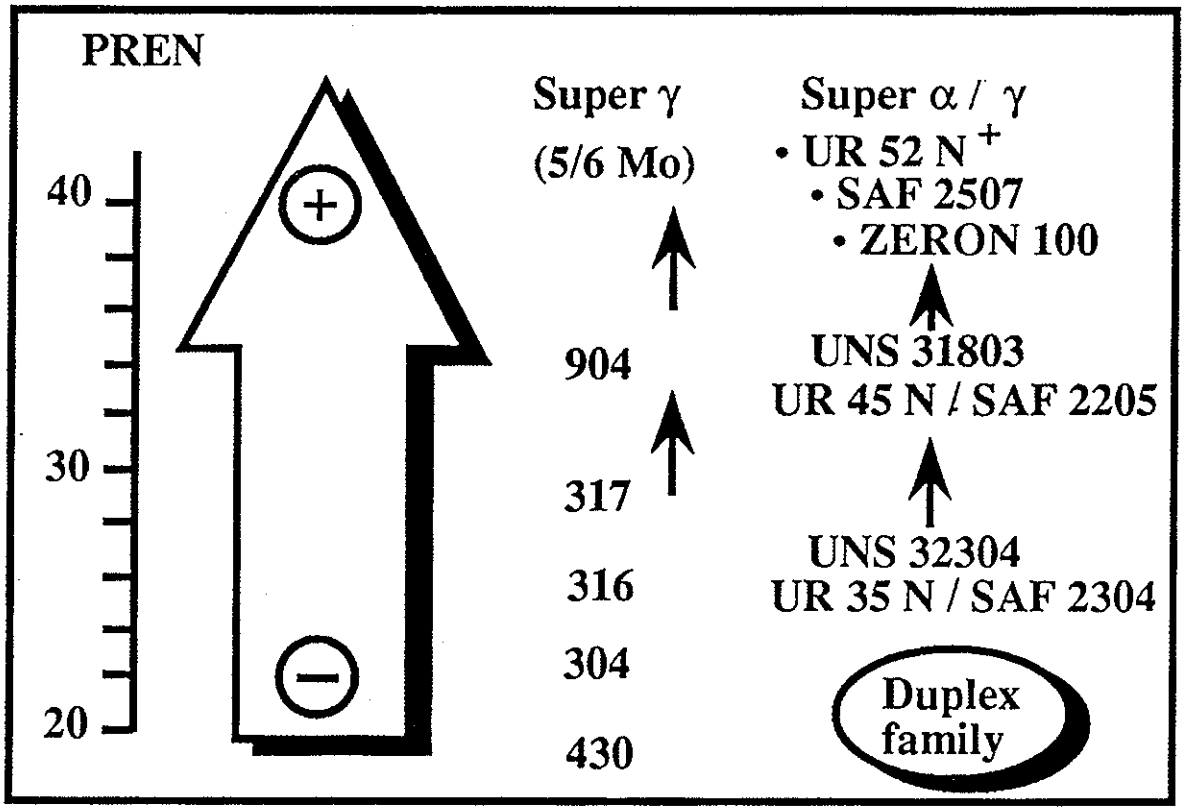

Fig. 1. Nominal PREN values for different stainless steels. [1]

DSS alloys are widely used for their high corrosion resistance in severe corrosive aqueous environments at service temperatures up to about 800°C. Both wrought and cast DSS alloys are available depending on the application. A tremendous amount of literature has been published regarding the phase transformation behavior, alloying element effects, corrosion resistance and mechanical properties of wrought DSS. However, even though cast DSS are used in many applications, they have been the subject of little research. It should be expected that the phase equilibria are different in the cast and wrought alloys due to differences in their nominal compositions.

The research undertaken in this study was to develop time-temperature-transformation (TTT, also known as isothermal transformation or IT) diagrams and continuous-cooling-transformation (CCT) diagrams for two types of cast DSS alloys, designated CD3MN and CD3MWCuN by the Alloy Casting Institute (ACI). Phase transformations in these alloys follow a nucleation and growth mechanism that is diffusion controlled. The transformation kinetics and phase constituents that occur as a result of quenching followed by isothermal holds were examined and directly measured by optical analysis using standard metallographic techniques. The phase transformation kinetics for both isothermal hold and continuous cooled alloys were analyzed from the experimental data using Johnaon-Mehl-Avrami (JMA) analysis.

The effects of alloying elements on the phase transformations during heat treatment were interpreted with the aid of the commercial thermodynamic package, *Thermo-Calc*. *Thermo-Calc* enables one to determine phase equilibria of metallic systems by using the appropriate thermodynamic databases included in the package.

CHAPTER 2: LITERATURE REVIEW

2.1. Phase Equilibria and Properties of Iron-based Alloys

2.1.1. Iron-Carbon Alloys (Fe-Fe_3C Metastable System)

The iron-carbon alloy system represents the basis of steels. The reasons for the importance of carbon steels are that they are easily and inexpensively produced and possess a favorable mixture of mechanical properties such as strength, toughness, and ductility by means of casting, machining and heat treating. Such a combination of properties and inexpensive price makes carbon steels attractive in industries and markets. However, the crucial disadvantage of plain-carbon steels is their poor corrosion resistance. Corrosion can be slowed by painting, enameling, or by appropriate alloying additions, such as Cr. When added to a level greater than about 10.5 wt.%, Cr protects steels from oxidation ("rust") by forming a continuous, Cr-rich passive layer on the metal surface.

The iron-carbon binary phase diagram is shown in Fig. 2. Pure iron is able to form in three allotropic variants: alpha (α), gamma (γ), and delta (δ). Alpha and delta iron have a body-centered cubic (BCC) lattice structure. They are conventionally called δ *ferrite* or α *ferrite* depending on the mode of formation. The γ-Fe phase has a face-centered cubic (FCC) lattice structure and is conventionally called *austenite*. The crystallographic properties of the different allotropic forms of iron are summarized in Table 1.

Carbon atoms occupy interstitial sites in the BCC ferrite and FCC austenite unit cells, and carbon solubility is directly related to hardening of steels. The intermetallic compound Fe_3C is called *cementite* and exists at 6.67 wt.%C with negligible solubility limits.

Cementite has an orthorhombic lattice structure and is brittle and hard. An invariant reaction known as the eutectoid reaction results in the formation of a lamellar α+Fe_3C structure during cooling. This two-phase mixture is referred to as *pearlite*. Since the pearlitic structure consists of soft ferrite and hard cementite layers, favorable mechanical properties can be obtained.

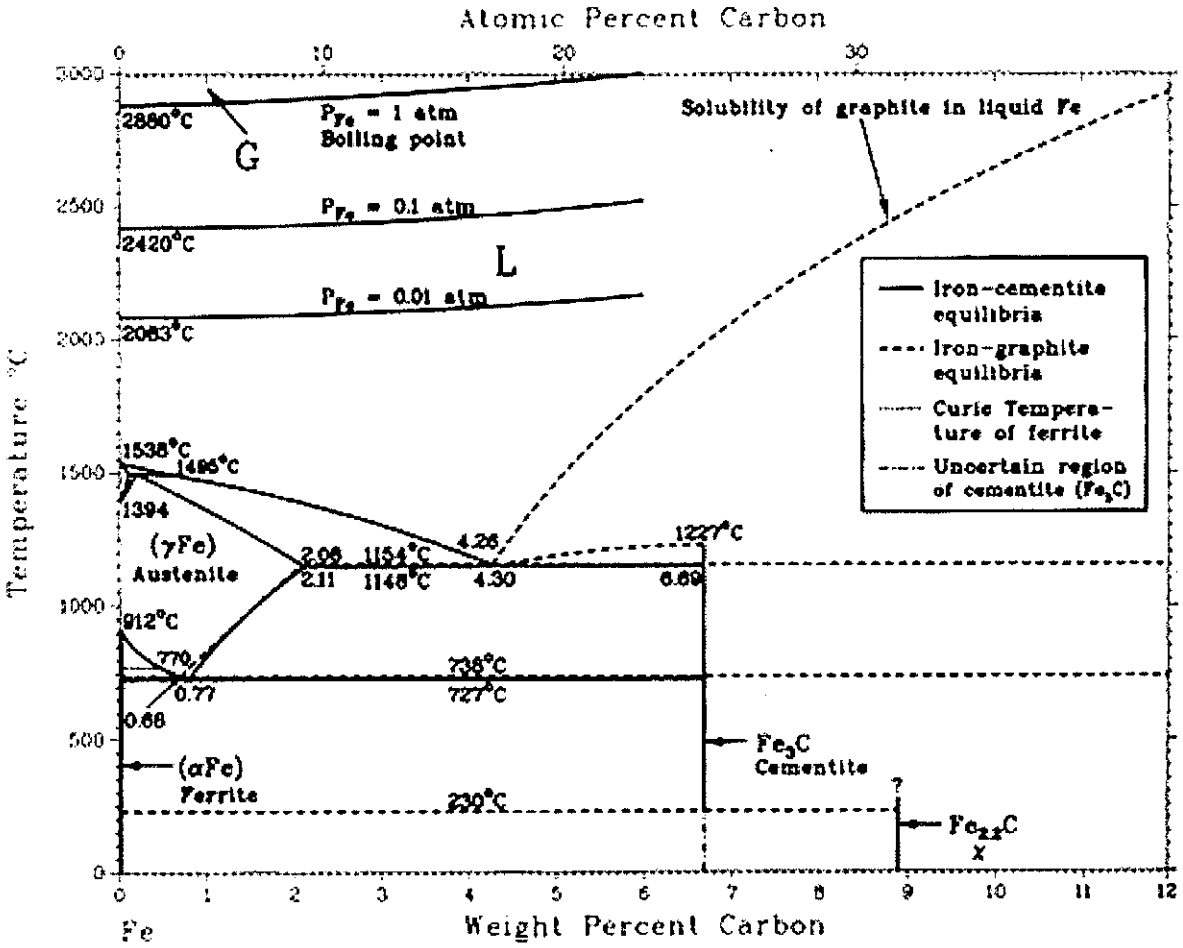

Fig. 2. Fe-C phase diagram. [3]

Table 1. Crystallographic properties of pure iron. [2]

Allotropic Forms	Crystallographic Form	Unit Cube Edge, Å	Temperature Range
Alpha	BCC	2.86 (70°F)	Up to 910°C
Gamma	FCC	3.65 (1800°F)	910-1403°C
Delta	BCC	2.93 (2650 °F)	1403-1535°C
Density, 7.868 g/cm^3	Melting point, 1535°C	Boiling point, 3000°C	

2.1.2. Effects of Alloying Additions on Iron-Carbon Alloys

The addition of alloying elements to the iron-carbon system affects the stability of the phases. Additions such as Cr, Si, Al, and Mo are called ferrite stabilizers since they promote ferrite phase formation over wider composition and temperature ranges than what are found in the Fe-C system. At the same time, the austenite region is contracted, i.e. the γ loop shrinks. The gamma loop is seen in the Fe-Cr phase diagram in Fig. 3. In contrast, elements such as C, Ni, Mn and N promote austenite formation and are called austenite stabilizers. The effect of Ni on the stability of the iron phases is shown in the Fe-Ni phase diagram in Fig. 4.

Zener and Andrews [4] described phase stabilizing effects in terms of thermodynamic variables. The ratio of alloying element concentrations in the α-phase (C_α) to that in the γ-phase (C_γ) follows an Arrhenius-type relationship (Eq. 2).

$$\frac{C_\alpha}{C_\gamma} = \beta e^{\Delta H / RT}, \text{ i.e. } \ln\frac{C_\alpha}{C_\gamma} = \frac{\Delta H}{RT} + \ln\beta \qquad \text{Eq. 2}$$

where β is a constant and ΔH is the enthalpy change, which is equal to the heat absorbed per unit of solute dissolving in the γ-phase minus the heat absorbed per unit of solute dissolving in α-phase, i.e., $\Delta H=H_\gamma-H_\alpha$. ΔH is positive for ferrite stabilizers since H_γ is greater than H_α. In this case, a γ-loop is introduced. For the austenite stabilizers, if H_γ is smaller than H_α, ΔH becomes negative, and the γ-region is expanded. Basic phase diagrams in terms of ΔH are illustrated in Figs. 3 and 4. The relative contribution to the phase-forming strength is shown in Fig. 5.

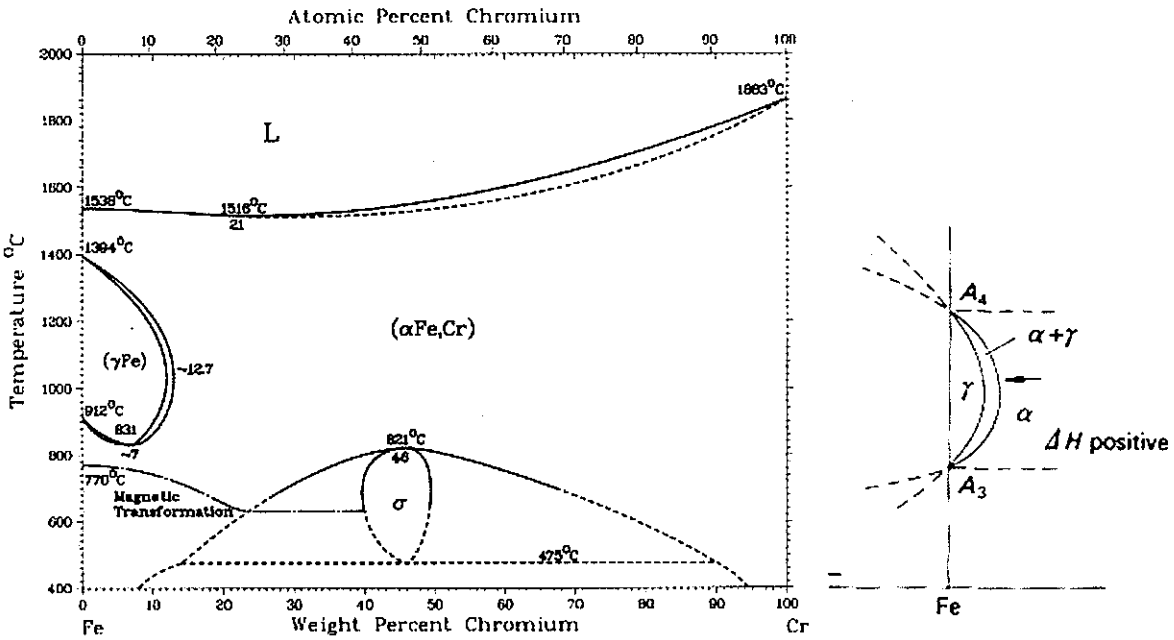

Fig. 3. Fe-Cr phase diagram and enlarged view of gamma loop.[3]

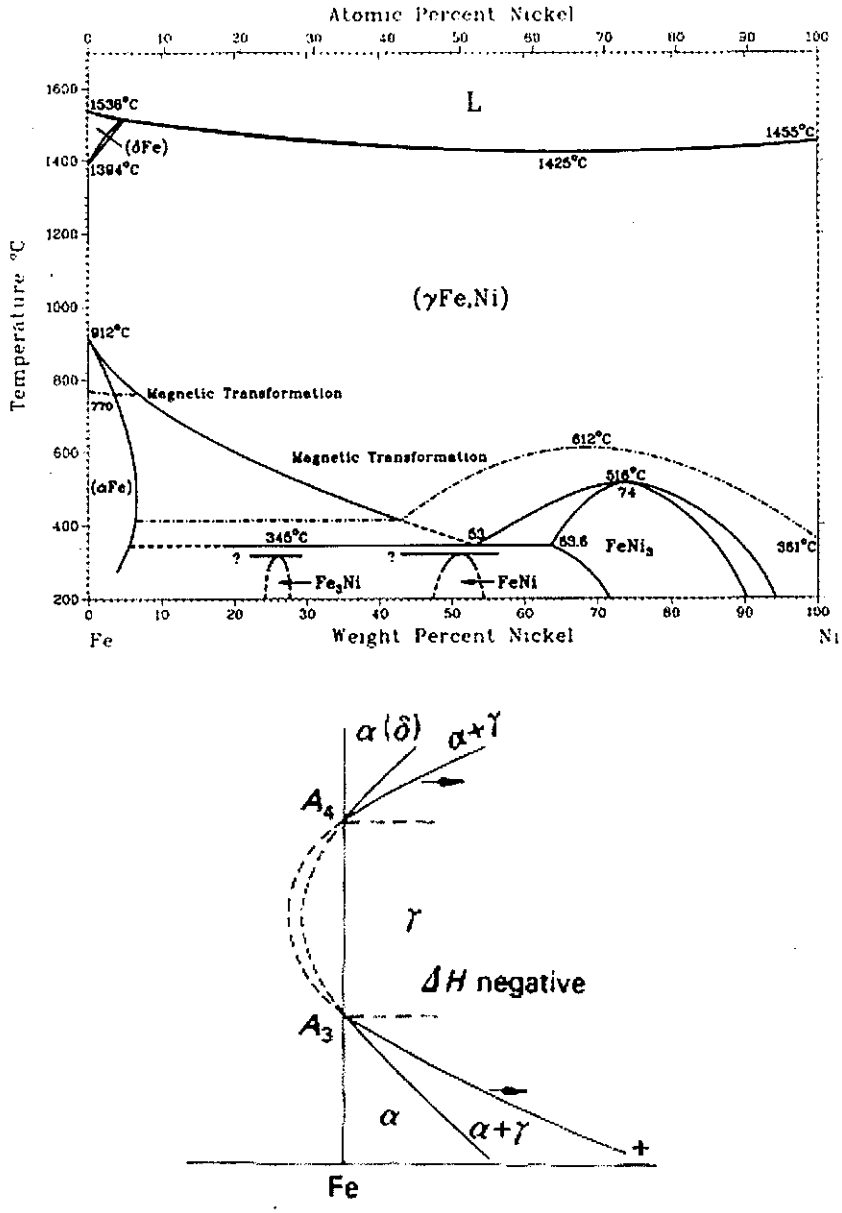

Fig. 4. Fe-Ni phase diagram and enlarged view of expanded gamma region.[3]

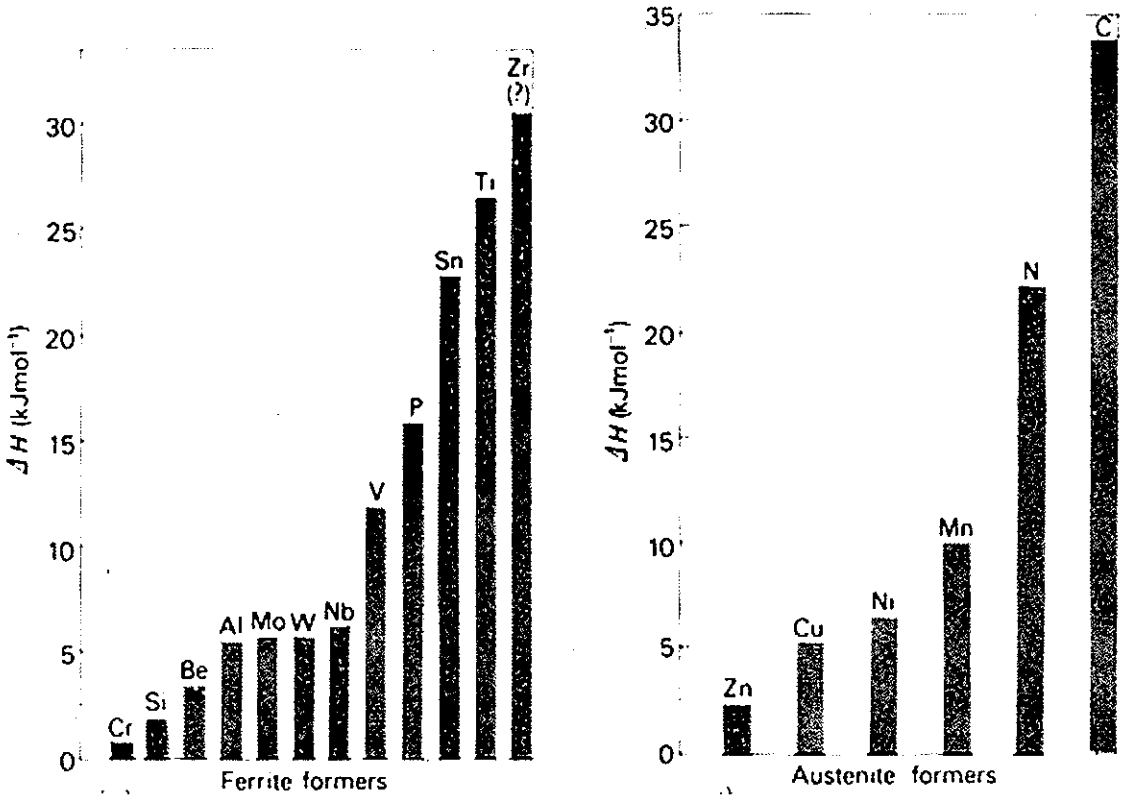

Fig. 5. Relative strength of alloying elements as ferrite formers and austenite formers.[4]

2.1.3. Stainless Steels

Stainless steels are defined as steels that contain a Cr content greater than 10.5 wt.% (Fig. 6).[5] Chromium plays an important role in making the iron surface passive by forming a Cr-rich surface oxide film that protects the underlying metal from corrosion. Stainless steels may solidify in either austenitic or ferritic microstructures, or a combination of the two. Intermetallic compounds (e.g., σ phase) or carbides (e.g., $(Fe, Cr)_{23}C_6$, $(Fe, Cr)_7C_3$) may form at intermediate temperature ranges.

Stainless steels are categorized into four groups on the basis of composition and crystal structure: ferritic, austenitic, martensitic and duplex stainless steels. In order to

control crystal structure, the effect of ferritic and austenitic stabilizing alloying elements should be taken into account on the basic iron-chromium system.

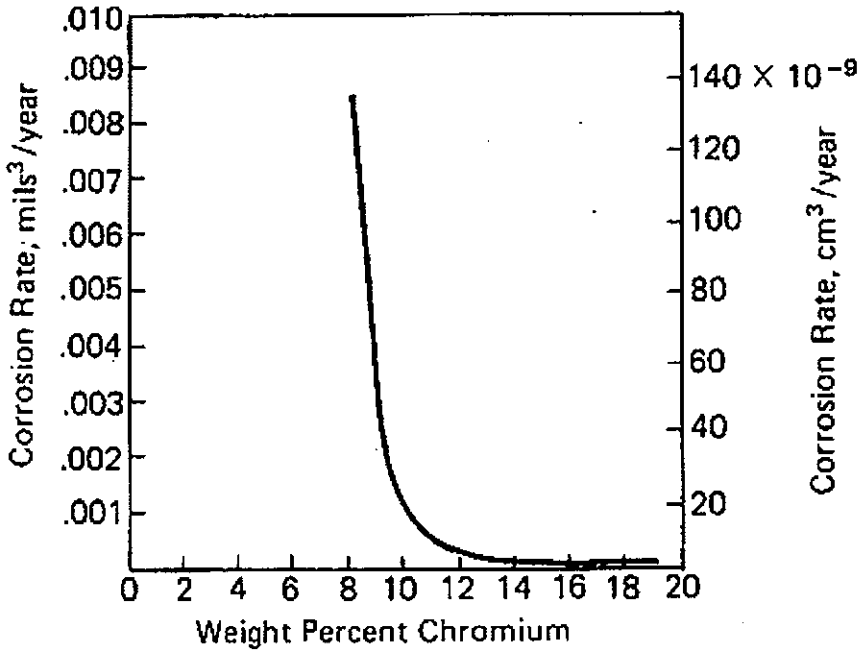

Fig. 6. Corrosion rate profile with respect to Cr contents.[5]

2.1.3.1. Ferritic Stainless Steels

Ferritic stainless steels have the BCC ferrite crystal structure as the matrix and exhibit ferromagnetism, similar to pure iron at room temperature. These alloys contain from 12wt% to 30wt% Cr with small amounts of minor alloying elements such as C, Mo, Si, Al, and Ti. Since carbon is an austenite stabilizer (Fig. 5) and forms brittle carbides, the carbon content usually remains below 0.12wt%.[2, 5] In order to improve corrosion resistance, or other properties such as weldability, other elements are added in small amounts.

The advantage of ferritic stainless steels having relatively high Cr-contents is their excellent corrosion resistance under atmospheric, stress induced, and oxidizing environments. However, conventional ferritic stainless steels are generally restricted in use due to poor weldability and low ductility. Furthermore, neither heat treatment nor cold working is able to harden ferritic stainless steels. A new generation of ferritic stainless steels, frequently referred to as the superferritics, has been developed by reducing C and N contents. In addition to high corrosion properties, these alloys have good ductility, formability and weldability.

2.1.3.2. Austenitic Stainless Steels

Austenitic stainless steels generally contain 16 to 25%Cr and up to around 35%Ni. This type of alloy is so named because their structure is FCC as is γ-iron. Such a structure is obtained by adding a strong austenite stabilizer, typically Ni, to the Fe-Cr system as a ternary element.

Adding austenite stabilizers, such as C, N, and Mn, can produce austenitic stainless steels that possess outstanding mechanical properties at both cryogenic and elevated temperatures. Figure 7 shows the yield strength of an austenitic steel (annealed Fe-18Cr-10Ni alloy) for various C+N contents as a function of temperature. Austenitic alloys can not be hardened by heat treatment, but do harden by cold working. However, high carbon contents can result in Cr-rich carbides forming at grain boundaries during slow cooling from annealing temperatures. Such a grain-boundary precipitation process in a stainless steel is generally referred to as sensitization which results in accelerated intergranular corrosion. The critical sensitizing temperature range is from 850 down to 400°C.

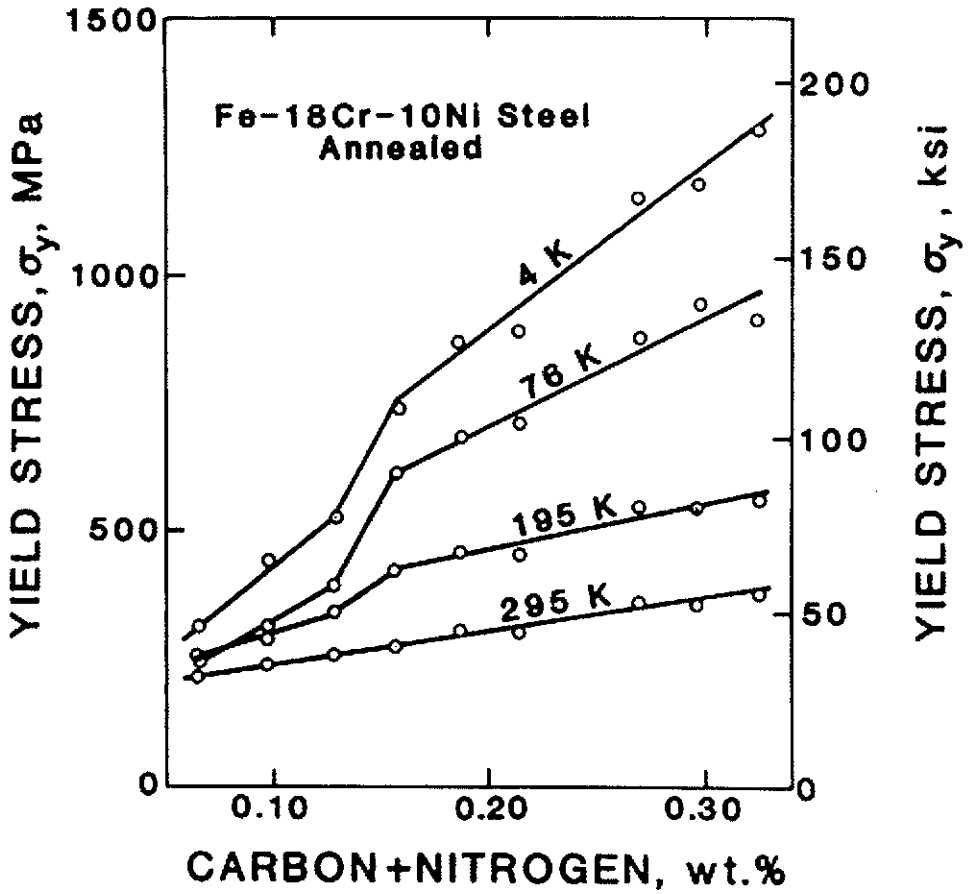

Fig. 7. Effect of carbon and nitrogen on yield strength in the austenitic alloy.[8]

2.1.3.3. Duplex Stainless Steels

Duplex stainless steels consist of a ferrite and austenite phase mixture. The major alloying elements are chromium, nickel, and molybdenum, and these enable the amount of ferrite and austenite phases to be balanced to approximately a 50-50 phase percent mixture. Duplex stainless steels solidify 100% ferrite. Upon cooling from the melting temperature the

ferrite starts to partially decompose into austenite that nucleates and grows first at the grain boundaries of ferrite, following favorable crystallographic orientations inside of the grains. As the temperature lowers the ferrite content decreases as austenite increases, and carbides and several intermetallic phases may be present. Figure 8 (a) and (b), respectively, represent microstructures of a wrought and cast duplex stainless steel with the same composition of Fe-22Cr-5.5Ni-3Mo-0.15N. The wrought steel exhibits a ferrite matrix with austenite islands aligned to a certain orientation. However, the microstructure of the cast steel contains a ferrite matrix with austenite islands of various morphologies.

The properties of duplex stainless steels are intermediate between the ferritic and austenitic stainless steels due to the presence of dual phases. The metallurgy, properties, alloying effects, and phase equilibria of duplex stainless steels will be discussed in detail later in this chapter.

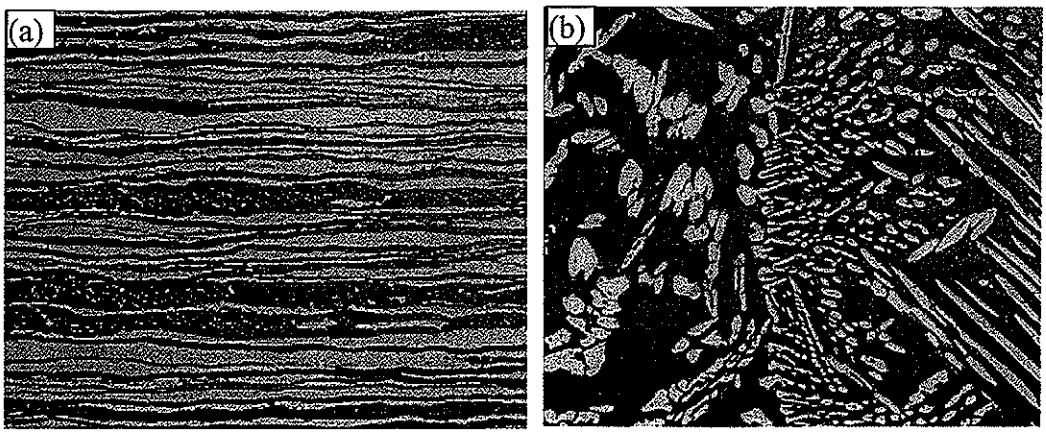

Fig. 8. (a) Microstructures of a wrought duplex stainless steel, parallel to rolling direction, and (b) the cast counterpart duplex stainless steel.[6]

2.2. Basics of Solid State Phase Transformations

2.2.1. Factors Affecting Phase Transformations

2.2.1.1. Diffusion

Since most phase transformations in solids depend upon atomic movement, diffusion is the most fundamental concept for understanding the morphologies and the kinetics of solid phase transformations. In 1855, Adolf Fick developed equations governing diffusion that are now known as Fick's 1st and 2nd laws of diffusion, Eq. 3 and 4, respectively. Both laws show the relationship between diffusion and concentration gradients.

$$J = -D\frac{dc}{dx} \qquad \text{Eq. 3}$$

$$\frac{\partial c}{\partial t} = \frac{\partial}{\partial x}\left(D\frac{\partial c}{\partial x}\right) \qquad \text{Eq. 4}$$

In these equations, D is the diffusion coefficient with typical units cm^2/s. The diffusion coefficient is generally proportional to temperature and the inverse of the atomic weight. Equation 4 is applicable to the situation where the concentration gradient changes with time and position.

The diffusion rate is sensitive not only to the concentration gradient but also to defects in materials such as grain boundaries, dislocations, and vacancies. Thus, the diffusion coefficient varies with defect concentration as well as temperature. Surface and grain boundaries are more open structures, and the resistance to atom migration is expected to be less than inside the lattice.

Vacancies play an important role when considering substitutional diffusion. In order to diffuse one lattice point to another, vacancies must be moving in the direction opposite to that of atomic diffusion. For substitutional diffusion in a binary alloy system, the sum of the A species, B species and vacancy fluxes must equal zero. In 1948, L. S. Darken[9] suggested an equation for binary interdiffusion behavior. The total flux of A atoms becomes as shown in Eq. 5.

$$J_A' = -D_A \frac{\partial c_A}{\partial x} + v c_A = -(X_B D_A + X_A D_B) \frac{\partial c_A}{\partial x} = \tilde{D} \frac{\partial c_A}{\partial x} \qquad \text{Eq. 5}$$

where $\tilde{D}=X_B D_A+X_A D_B$ is called the interdiffusion coefficient.

2.2.1.2. Precipitate Nucleation

The first step of a phase transformation, called the nucleation process, is the formation of small groups of atoms into stable nuclei. The driving force for nucleation is the change in the Gibbs free energy of the system. Three different types of free energy change can be associated with the nucleation process. Firstly, the volume free energy (ΔG_V) of the system is reduced with the creation of nuclei having volume V. Secondly, since nuclei create new interfaces in contact with a supersaturated matrix, the area A of new interface increases the free energy of the system by its surface energy, γ. Thirdly, the strain field between the matrix and nuclei due to misfit of those two phases produces a volumetric strain energy (ΔG_s), which increases the free energy of the system. The destruction of defects such as grain boundaries, stacking faults and dislocations during heterogeneous nucleation process can decrease the free energy of the system by ΔG_d. Defects are energetically and kinetically

favored places to form nuclei. Addition of the above contributions gives the total free energy change of the system as,

$$\Delta G = -V(\Delta G_v - \Delta G_s) + A\gamma - \Delta G_d \qquad \text{Eq. 6}$$

For a given undercooling below the equilibrium transformation temperature, ΔT, heterogeneous nucleation tends to take place at a higher rate than homogeneous nucleation. This can in part be understood in terms of rates of diffusion, as discussed in the previous section. Since grain boundaries are fast diffusion paths compared to the lattice, atoms can move and form a nucleus easier than inside lattice. Figure 9 shows the ratio of the activation energy for grain boundary nucleation versus homogeneous nucleation with respect to the angle between a grain boundary and a nucleus.

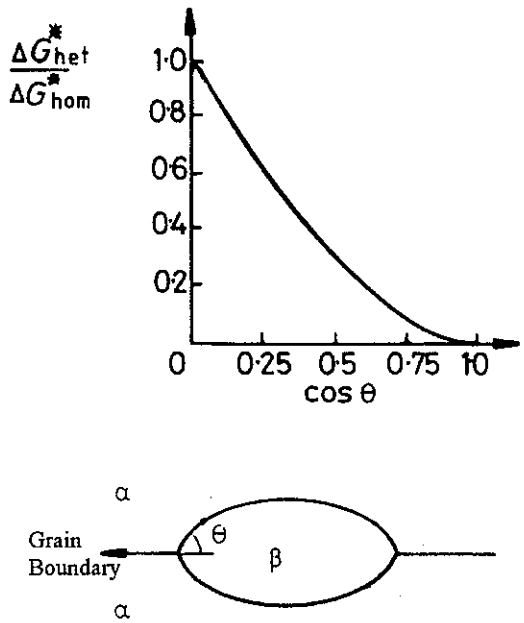

Fig. 9. The ratio of activation energy with respect to the angle between a grain boundary and a nucleus.[12, 13]

2.2.1.3. Precipitate Growth

Once a stable nucleus forms it starts to grow by gaining more atoms. Accordingly, the growth rate depends on the diffusion of atoms through the surrounding media. Like the nucleation process, growth is driven by the amount of undercooling from its equilibrium temperature and the rates of diffusion, with diffusion rate often being a more critical factor than undercooling. The maximum growth rate is usually obtained at undercooling temperatures higher than those producing the maximum nucleation rate, as illustrated in Fig. 10.

In solid state transformations, precipitates often grow along preferred orientations. The direction of growth depends on the coherency of the interface between two phases, since coherent or semicoherent interfaces have low mobility while incoherent interfaces have a high mobility. Growing along preferred directions produces distinctive final morphologies such as disk- or plate-like shapes.

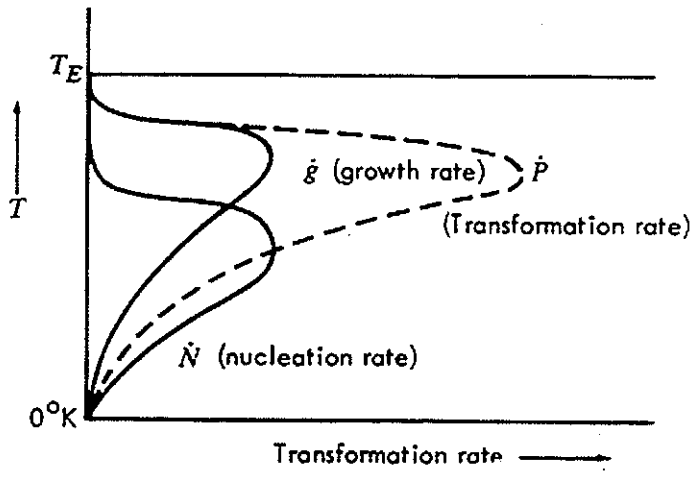

Fig. 10. Location of the maximum growth rate.[10]

2.2.2. Transformation Kinetics

2.2.2.1. Time-Temperature-Transformation (TTT) Diagrams

The total rate of transformation will essentially depend on the nucleation and growth rates. Since the diffusion rate and degree of undercooling play critical roles in determining transformation rate, the total time required for the phase transformation follows C-shape curves in temperature versus time plots (Fig. 11). This type of transformation diagram is commonly referred to as a time-temperature-transformation (TTT) diagram. Since TTT diagrams predict the transformed fraction of a phase with respect to time at a fixed temperature, they are also called isothermal transformation (IT) diagrams. The fastest transformation rate is located in the minimum time intercept on the TTT curve which is referred to as the nose of the curve.

In general, the rate of the phase transformation is determined not only by the rates of nucleation and growth, but also by the density and distribution of nucleation sites, the overlap of diffusion fields from adjacent transformed volumes, and the impingement of adjacent transformed volumes. The empirical equation for transformed fraction at some fixed temperature, which takes into account all these effects, is given as,

$$f = \frac{V}{V_e} = 1 - \exp(-kt^n) \qquad \text{Eq. 7}$$

where f is fraction transformed, k is a reaction constant in min^{-n}, which is sensitive to temperature due to the dependence of nucleation and growth rates, and the exponent n is a dimensionless constant that depends on the combination of nucleation and growth mechanisms for the transformation in question. In order to obtain the transformed volume fraction (f), it is necessary to find the equilibrium volume percent (V_e) at the temperature of

interest. Extremely long-time anneals were therefore needed to determine V_e. The data were then fit to Eq. 7 with the n and k in this equation determined on the basis of the following equations:

$$n = \frac{\ln \dfrac{\ln(1 - V_1 / V_e)}{\ln(1 - V_2 / V_e)}}{\ln t_1 / t_2} \qquad \text{Eq. 8}$$

$$k = \frac{-\ln(1 - V_1 / V_e)}{t_1^n} \qquad \text{Eq. 9}$$

where t_1 and t_2 are isothermal hold times 1 and 2, respectively, and V_1, V_2, *and* V_e are volumes for times t_1, t_2 and equilibrium, respectively. Typical values of n are listed in Table 2. This equation is called the Johnson-Mehl-Avrami (JMA) equation or, more shortly, the Avrami equation. The Avrami equation provides a good phenomenological description of solid state transformation kinetics, and is applicable for most solid-state phase transformations.

TTT curves can be constructed by plotting the changes that occur in material properties, or by direct observation of the amount of transformed material after holding for various times and quenching. In either method, samples are heated to a homogenizing temperature for sufficient time for the structure to reach equilibrium, then quenched to a particular transformation temperature and held at that temperature for a desired duration. At completion, the samples are quenched to room-temperature and then prepared metallographically for microstructural analysis. The volume fraction transformed can be

counted either manually using test grids (e.g. see ASTM E562) or automatically by employing computer software. TTT curves can be determined for all temperatures by employing the Avrami Equation (Eq. 7) with the substitution of numerical volume fractions (Fig. 12) obtained experimentally.

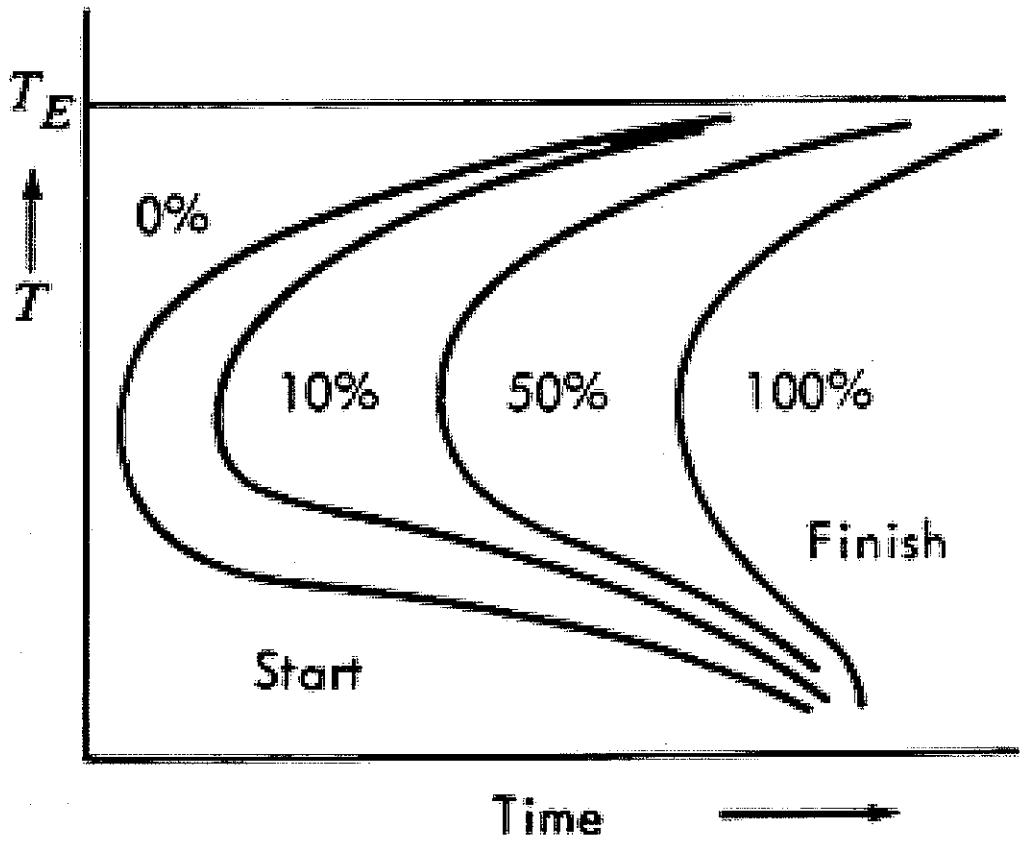

Fig. 11. Typical TTT curves.[10]

Table 2. Typical *n* values under various phase transformation conditions.[14]

(a) Polymorphic changes, discontinuous precipitation, eutectoid reactions, interface controlled growth, etc.

Conditions	n
Increasing nucleation rate	>4
Constant nucleation rate	4
Decreasing nucleation rate	3-4
Zero nucleation rate (saturation of point sites)	3
Grain edge nucleation after saturation	2
Grain boundary nucleation after saturation	1

(b) Diffusion controlled growth.

Conditions	n
All shapes growing from small dimensions, increasing nucleation rate	>2.5
All shapes growing from small dimensions, constant nucleation rate	2.5
All shapes growing from small dimensions, decreasing nucleation rate	1.5-2.5
All shapes growing from small dimensions, zero nucleation rate	1.5
Growth of particles of appreciable initial volume	1-1.5
Needles and plates of finite long dimensions, small in comparison with their separation	1
Thickening of long cylinders (needles) (e. g. after complete end impingement)	1
Thickening of very large plates (e. g. after complete edge impingement)	0.5
Precipitation on dislocations(very early stages)	≈ 0.67

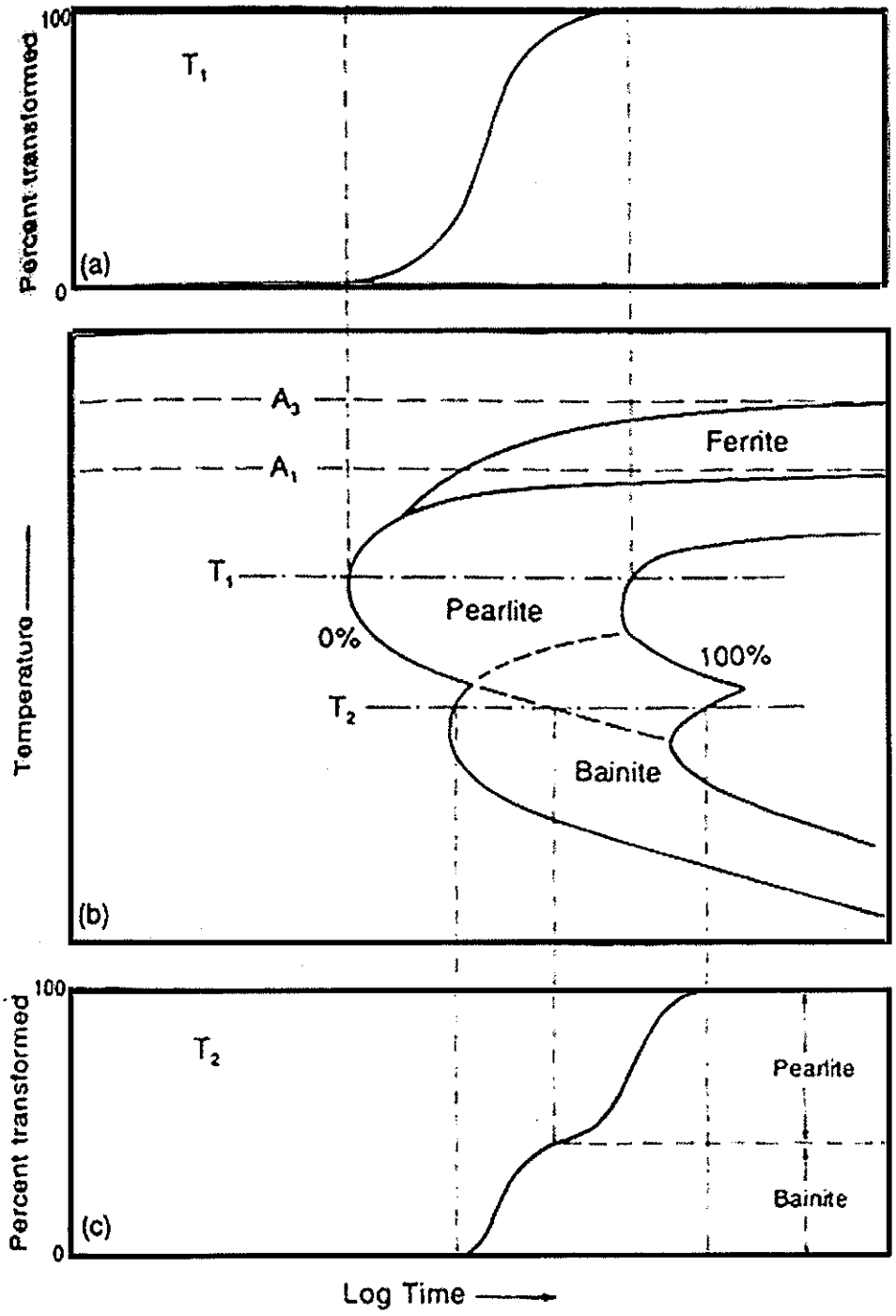

Fig. 12. Construction of TTT curves.[15]

In addition to the microstructural changes, changes in material properties due to phase transformations, such as specific volume, electrical resistivity, and magnetic permeability may be used to deduce TTT curves. The most commonly used techniques are dilatometry and differential thermal analysis (DTA)[15]. Dilatometry is an in-situ thermal analysis method for recording volume changes. Since the thermal expansion coefficients ($\alpha = \frac{1}{V}\left(\frac{dV}{dT}\right)$) of different phases usually vary, a plot showing thermal expansion as a function of temperature will have different slopes as phases form and/or disappear. Electrical properties of materials such as electrical resistivity and electrical conductivity can also be used to measure phase constituents of a material. Studies employing electrical resistivity (ρ) measurements have been used to investigate isothermal phase transformation kinetics[16]. The effective electrical resistivity ρ_e in Fig. 13 is written as,

$$\rho_e = \frac{\rho(t) - \rho_i}{\rho_s - \rho_i} \qquad \text{Eq. 9}$$

where ρ_i and ρ_s are the initial and final resistivity values, respectively, and $\rho(t)$ is the resistivity at some time, t. An example of curves showing dilatometry and resistivity analyses are provided in Fig. 13. Note that if two phases are transformed in the same time ranges, there should be an onset (T_s' point in Fig. 13 (a)) appearing on the curve. Alternatively, electrical conductivity (σ) is reciprocally related to electrical resistivity. The general model[17] for electrical conductivity in a multiphase system is given as,

$$\sigma_{eff}^{n} = \sum_{i=1}^{m} f_i \sigma_i \qquad \text{Eq. 10}$$

where n represents the situation of perfect alignment of the individual phases, with n=1 (upper limit) occurring when the phases are aligned in sheets parallel to the direction of applied current.

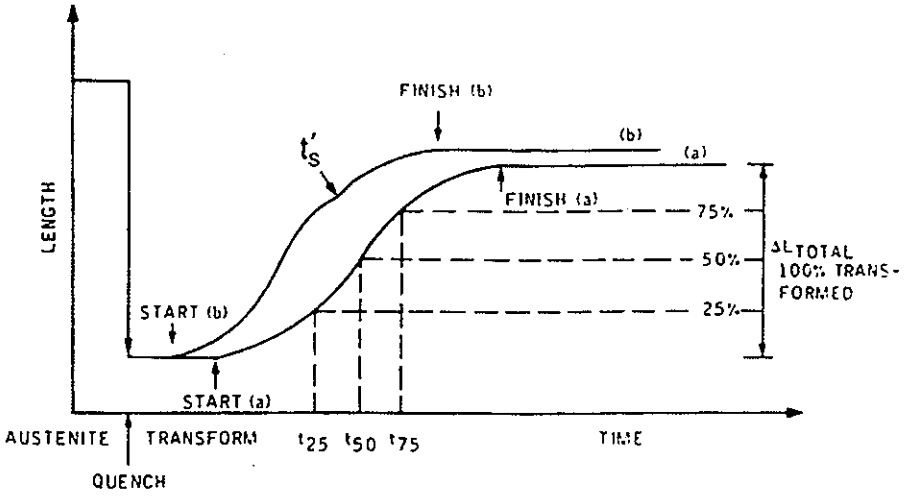

(a)

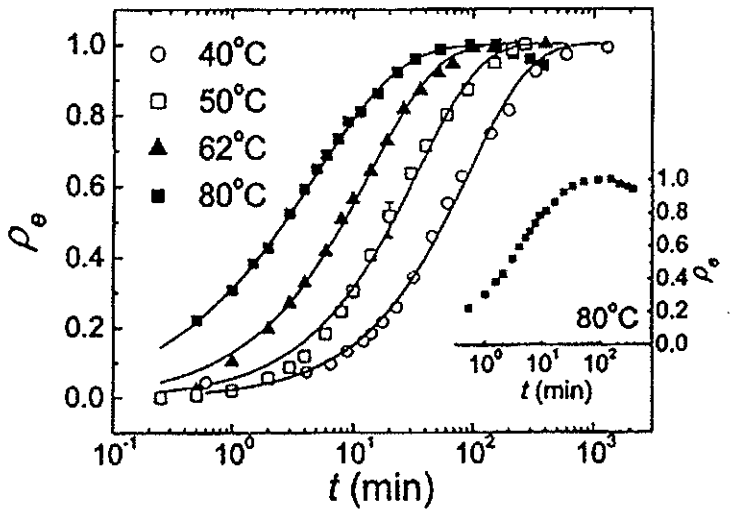

(b)

Fig. 13. Phase transformation profiles from (a) dilatometry[15] and (b) electrical resistivity measurement.[16]

2.2.2.2. Continuous-Cooling-Transformation (CCT) Diagrams

Unlike isothermal transformation curves which depend only upon fixed temperatures, continuous cooling transformation (CCT) diagrams are concerned with both transformation time and temperature under certain cooling rates. Accordingly, CCT diagrams are extremely useful for commercial heat treatments and in welding industries. An example of how control of the microstructure can be achieved through various cooling rates is illustrated in Fig. 14.

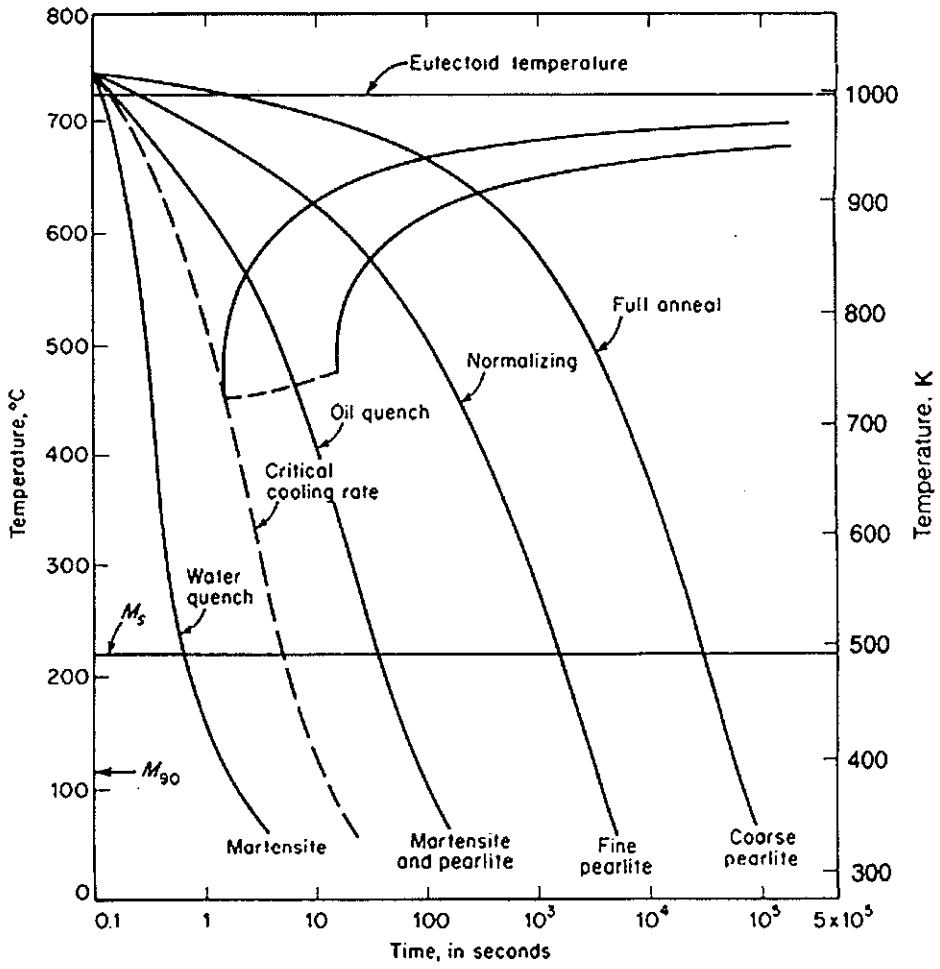

Fig. 14. Control of microstructure by varying cooling rates.[18]

Based on the additivity rule[19], Wilson *et al.*[20] modified the Avrami equation (Eq. 7) for a continuous cooling situation. The modified equation (Eq. 12) is given as,

$$V_i = V_{mi}\left[1 - \exp\left\{-k_i\left(t_i' + \Delta t_i\right)^{n_i}\right\}\right] \qquad \text{Eq. 12}$$

where t_i' is a fictitious time, $t_i' = \left(\frac{\ln(1 - V_{i-1}/V_{mi})}{-k_i}\right)^{1/n_i}$, n_i and k_i are from an Avrami plot at the temperature i, and V_{mi} is the maximum or equilibrium volume fraction at the temperature i. The fictitious time (t_i') indicates the time required to reach the transformed volume fraction at the beginning of a temperature step, i. At a temperature step i, the phase transformation behavior is approximated to be the same as an isothermal transformation, and therefore directly follows the Avrami equation from t_i' through $t_i'+\Delta t$. Equation 12 is further discussed in Chapter 6. Another approximated model for the transformation of austenite to bainite was proposed by Venkatraman *et al.*[22] The volume fraction transformed has a relation,

$$f = 1 - \exp\left\{-\left(t/\tau\right)^n\right\} \qquad \text{Eq. 13}$$

where τ is a time constant which equals $\tau_0 \exp(-Q/RT)$, and n is from the time exponent in the Avrami equation, which can be determined by experiments with other constants, τ_0 and Q. Both of the above models presume site saturation at the nucleation stage. That is, nucleation occurs only at the very beginning of the transformation process.

The most commonly used experimental technique for the determination of CCT curves is dilatometry. The transformation times and temperatures can be produced by performing a series of cooling experiments with changing cooling rates. A CCT diagram can be determined by comparison of metallographic observations to the data from dilatometry

experiments. An example of the construction of CCT curves by dilatometry is shown in Fig. 15(a).

It is reported[24-26] that thermomechanical testing can be applicable to measuring the transformation times and temperatures during cooling of a specimen. Thermomechanical tests are based on the idea that when a phase transformation occurs in a specimen, a strain field is induced. If a phase transformation takes place during cooling at a given cooling rate, either a stress-strain curve or a stress-temperature curve may deviate from the ideal curves as in a strain-free material. An ideal stress-temperature curve and deviation from ideality due to microstructural evolution are shown in Fig. 15 (b) and (c) during continuous cooling compression (CCC) tests. The new phase fraction formed (f_{new}) can be calculated from a CCC curve as,

$$f_{new} = strain(\varepsilon) - \frac{stress(\sigma)}{regressed \quad slope} \qquad \text{Eq. 14}$$

It is reported that this type of test, rather than dilatometry, is useful to predict CCT curves for hot rolling products.

(a)

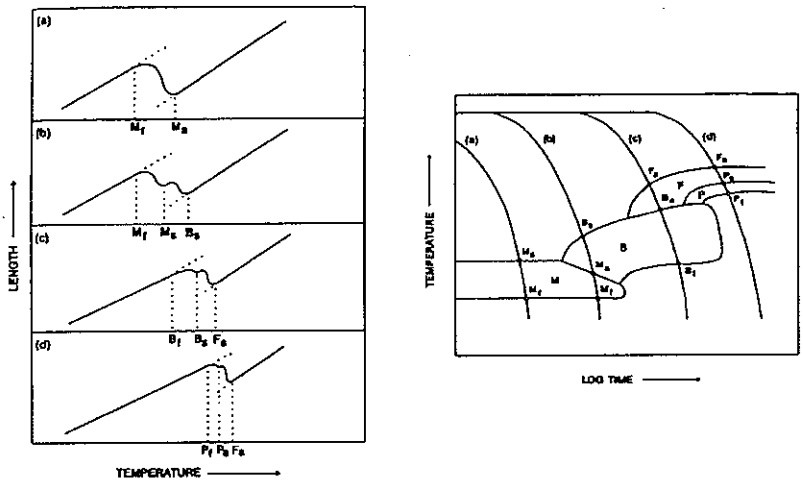

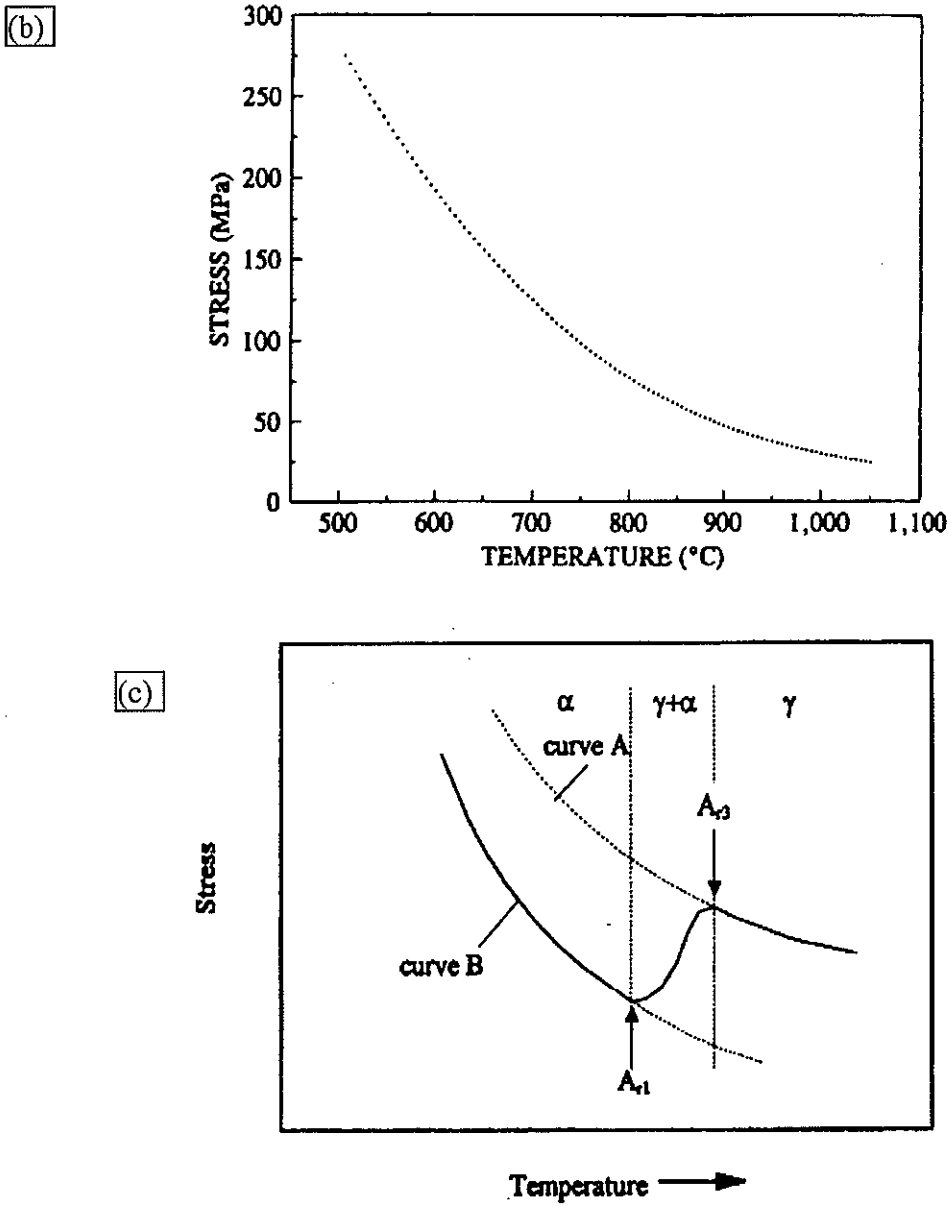

Fig. 15. Construction method of CCT diagram by (a) dilatometry[23], and thermomechanical test: (b) ideal stress-temperature curve[25] and (c) the case of the presence of a second phase[26].

2.3. Metallurgy and Properties of Cast Duplex Stainless Steels

2.3.1. Designations of Cast Stainless Steels

Cast duplex stainless steels CD3MN and CD3MWCuN are designated in accordance with the Alloy Casting Institute (ACI) standards. Alternative designations are, UNS J92205 or ASTM A 890/A 890M 99 Grade 4A for CD3MN and UNS J93380 or ASTM A 890/A 890M 99 Grade 6A for CD3MWCuN. The grade designations of cast stainless steels most commonly follow the ACI standards. The first letter of the designation indicates the service condition, which can be either liquid corrosion service (C) or high temperature service (H). Corrosion resistant castings are used in aqueous environment at temperatures below approximately 650°C, and heat resistant castings are suitable for service temperature above approximately 650°C. The second letter loosely denotes the chromium and nickel contents in the alloy (Fig. 16). The number following the first two letters indicates maximum carbon content in 100 times percentage. Heat resistant alloys usually have a higher carbon content than corrosion resistant alloys. Additional alloying elements are included as a suffix following the carbon content. CD3MN and CD3MWCuN refer to alloys for corrosion-resistant service and are the 30Cr-5Ni type with a maximum carbon content of 0.03% and containing molybdenum and nitrogen in the case of the former and molybdenum, tungsten, copper and nitrogen in the case of the latter. Other designations commonly used for CD3MN and CD3MWCuN and their wrought counter parts are shown in Table 3.

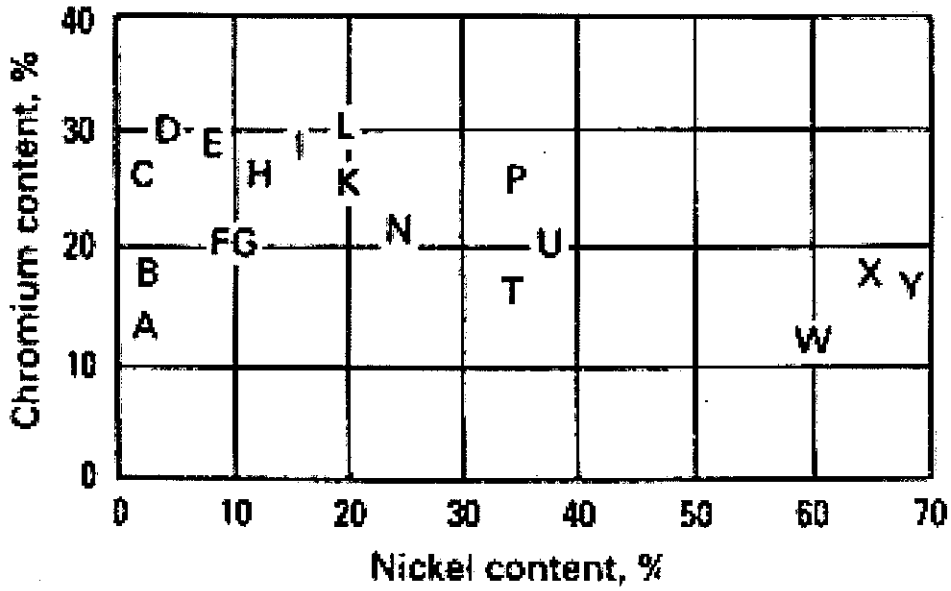

Fig. 16. Cr and Ni contents in ACI standard grades.[6]

Table 3. Materials and their standard designations.[27]

ACI Standard	Wrought Counterparts	UNS	Designations	
			ASTM	UNS
CD3MN	SAF 2205	S31803	A890-4A	J92205
CD3MWCuN	Zeron 100	S32760	A890-6A	J93380

2.3.2. Microstructure

DSS have primary (δ and γ_1) and secondary (secondary austenite (γ_2), σ, χ, carbides, nitride, etc.) phases. Secondary austenite (γ_2) has the same crystal structure as primary austenite (γ_1), however, the lattice parameter and the formation temperature are slightly

different from γ_1. In spite of the differences the properties of γ_1 and γ_2 are essentially identical. Austenite is known to improve mechanical properties, for example fracture toughness[27], and is beneficial to DSS performance.

Secondary phases are usually in the form of intermetallics, which reduce mechanical and corrosion properties. The phases most deleterious to mechanical and corrosion properties are the Cr and Mo rich intermetallic phases, since their formation removes significant amounts of these elements from the matrix. [27,31,55] The σ phase has a tetragonal lattice structure and higher Cr content than the matrix δ and γ phases. The nucleation of σ is usually observed at the interphase boundary between δ and γ. Formation of such a phase causes depletion in Cr content of the primary phases. Similarly, precipitation of the high Mo content intermetallic phase χ may detrimental to the performance of DSS.

Since the intermetallic phases take Cr and Mo from the primary phases, those elements can be depleted near interphase boundaries of γ and δ. This phenomenon may reduce pitting corrosion resistance.[58] Intermetallic phases are usually brittle, so that they are harmful for impact toughness.[1,29] Therefore, the existence of such phases degrades both corrosion and mechanical properties and much research had been done investigating embrittlement due to these phases.[31,55] Higher molybdenum encourages the formation of χ, reported to be more brittle than σ phase.[31]

Carbon content in DSS is usually very low (less than 0.03 wt.%). Carbide formation, which generally embrittles steels, typically does not affect the mechanical properties of DSS but is reported to play a role in the formation of dual phase morphology with γ_2 or σ.[39]

Nitrides, for example Cr_2N, can be formed in many DSS. The formation mechanism and orientation relationship of such a phase with the primary phases has been reported.[54]

The stability of a given secondary phase usually depends on Fe, Cr, Mo and Ni contents in the steel. The effect of alloying elements on the formation of those phases is indicated in Fig. 17.

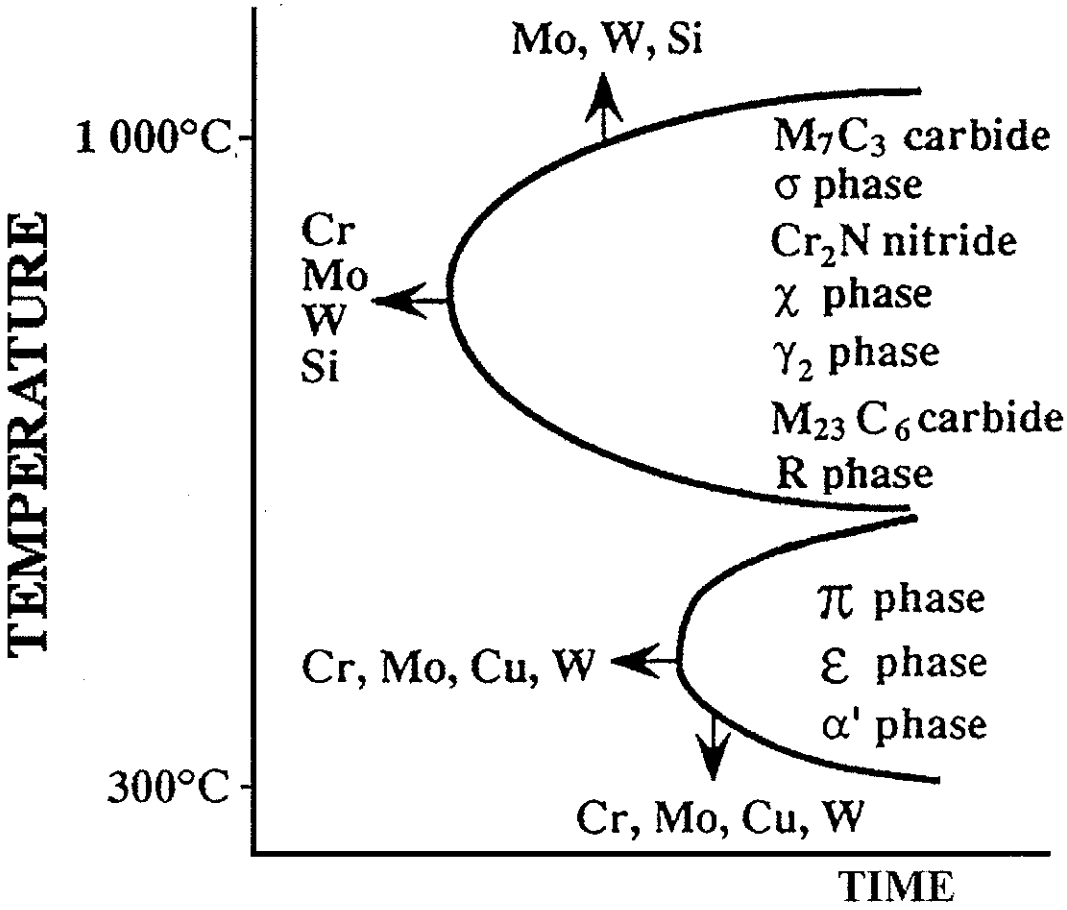

Fig. 17. Secondary phases in duplex stainless steels and the effects of alloying elements on the location and shape of TTT curve for these phases. After reference 28.

2.3.3. TTT and CCT Diagrams of Duplex Stainless Steels

Many transformation diagrams of wrought duplex stainless steels have been published. The TTT diagram for the U50 alloy (Fig. 18) is considered as a standard TTT diagram, and is commonly used by DSS casters. Josefsson *et al.*[34] found that the nose of the sigma phase curve on a TTT diagram is shifted to lower temperatures and longer times after solution heat treatment at a higher temperature (1300°C), as shown in Fig. 19. TTT diagrams of UR45N and Zeron 100 alloys, which are the wrought counterparts of CD3MN and CD3MWCuN, respectively, are seen in Fig. 20. More TTT and CCT diagrams of DSS are presented in Figs. 21 and 22. No transformation diagrams are known to exist for cast DSS alloys.

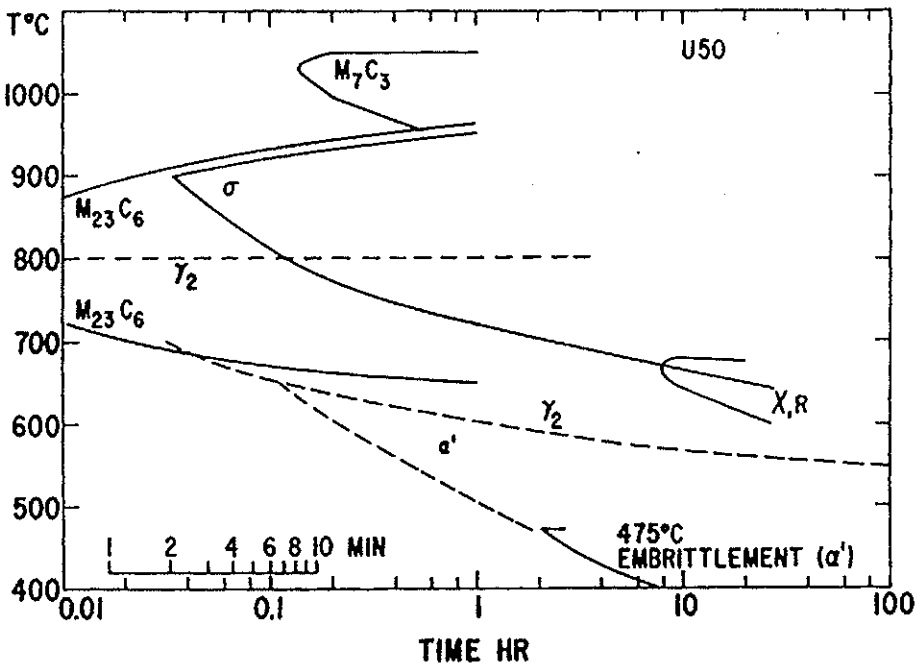

Fig. 18. TTT diagram of U50 alloy.[32, 33]

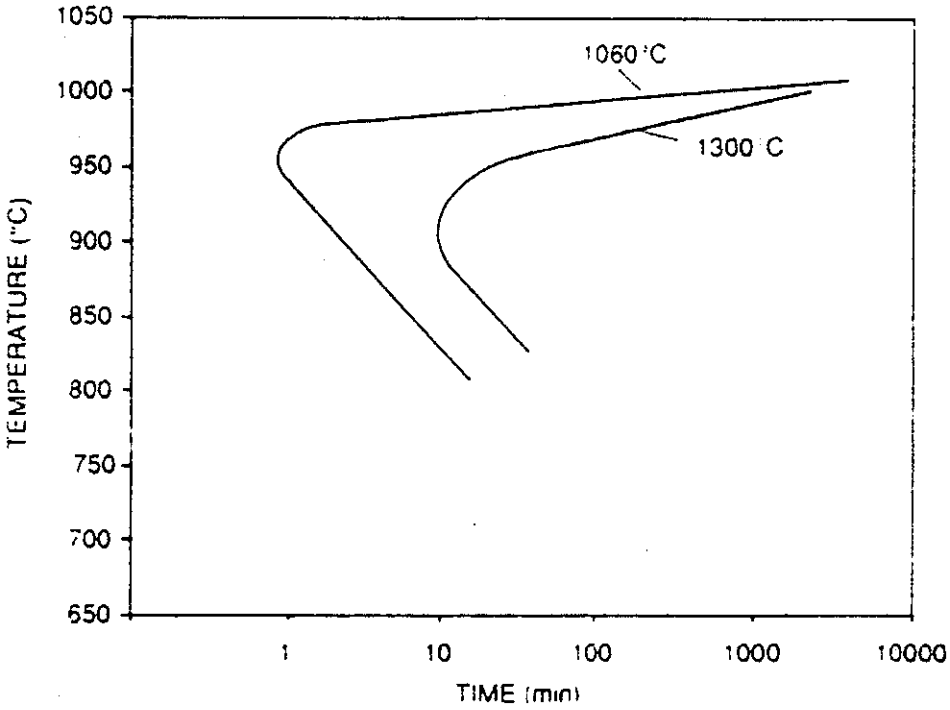

Fig. 19. Effect of solution heat treatment temperatures (1060°C and 1300°C) on the nose of sigma phase transformation curves.[34]

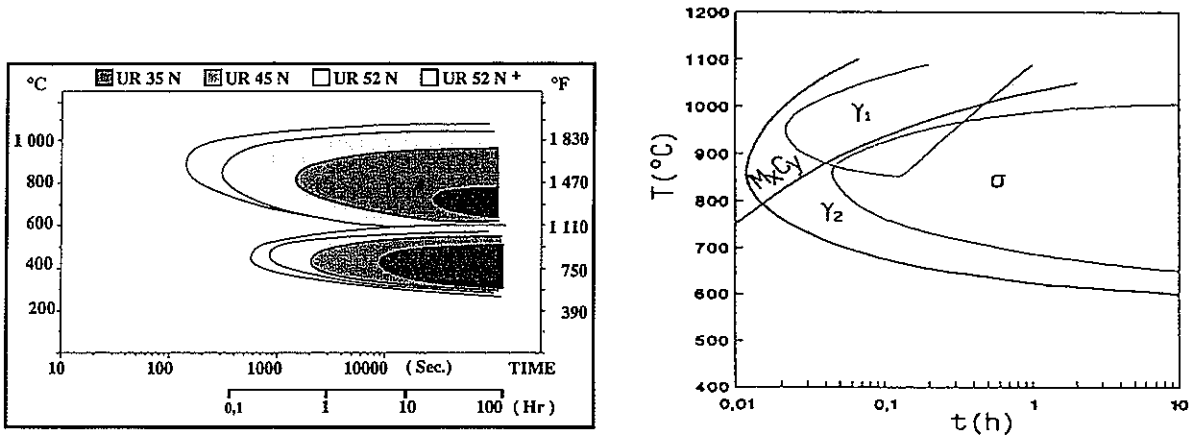

(a) (b)

Fig. 20. TTT diagrams of (a) UR45N [28] and (b) Zeron100™.[35]

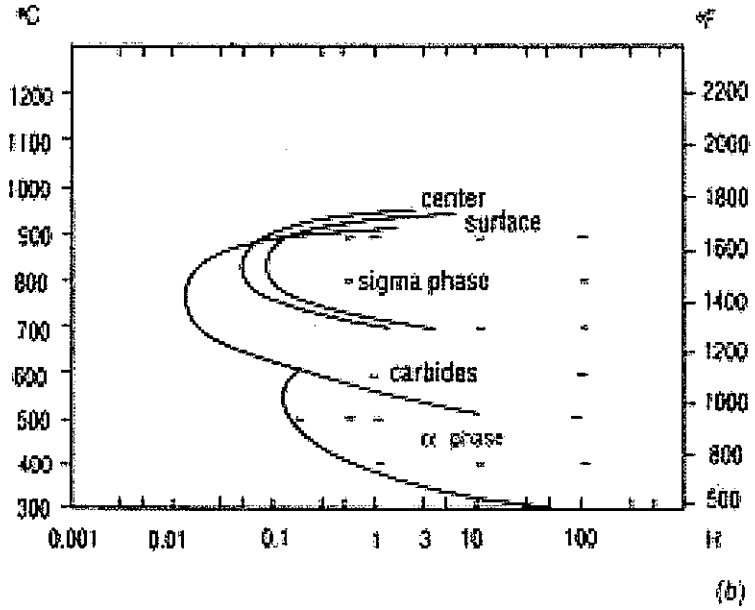

(a)

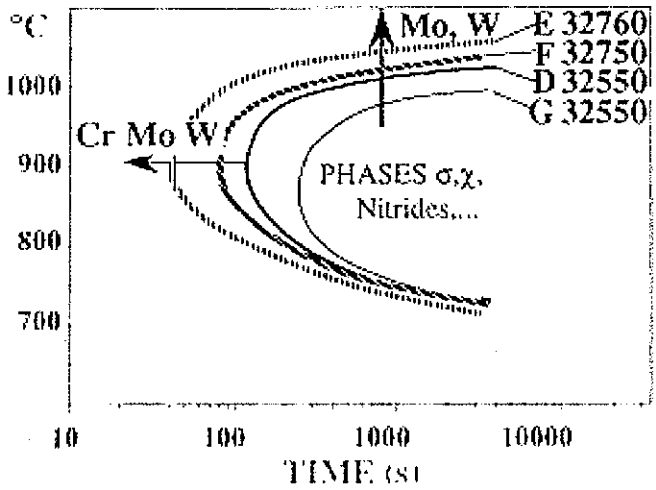

	Cr	Mo	N	
D	25	3.7	. 25	1.5 Cu
E	25	3.7	. 22	.6Cu.7W
F	25	3.8	. 28	-
G	25	3	. 18	1.5 Cu

(b)

Fig. 21. TTT diagrams of duplex stainless steels; (a) UR52N [30], (b) various DSS superimposed.[1]

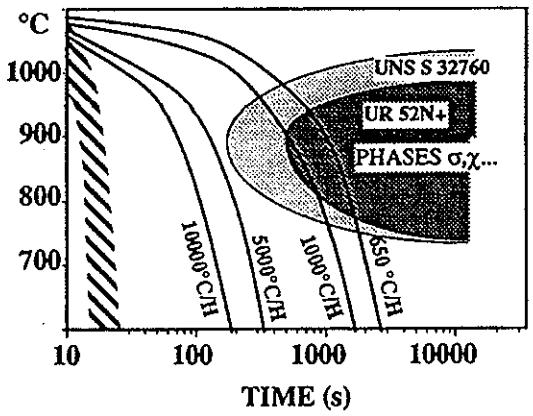

(a)

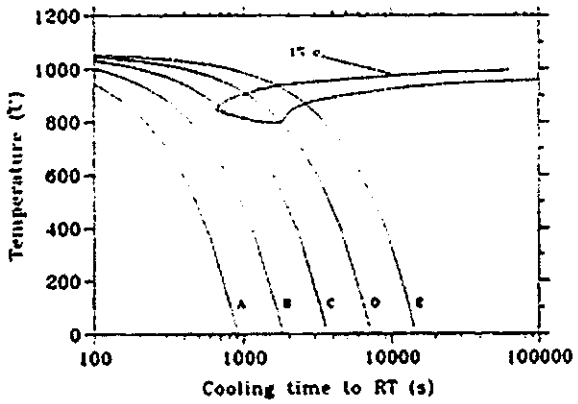

(b)

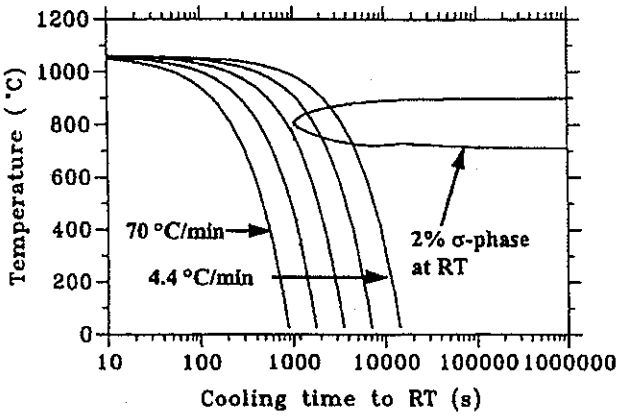

(c)

Fig. 22. CCT diagrams of sigma phase precipitates in duplex stainless steels; (a) S32760 and UR52N[28], (b) SAF2507[34], (c) 29Cr-6Ni-2Mo-0.38N super DSS alloy.[29]

CHAPTER 3. PROJECT AIMS

Based upon the literature survey presented here, the specific aims of this dissertation study can now be formulated. The goal of this study will be to develop TTT and CCT diagrams of cast DSS with a comprehensive understanding of the phase transformation behaviors. Determination of both types of diagrams will be achieved using various heat treatments followed by extensive characterization of the samples using methods such as optical and electron microscopy. The transformation behavior will be further analyzed using an existing thermodynamic software package, *Thermo-Calc*. This package will be used to aid in the interpretation of the determined TTT and CCT diagrams from the standpoint of understanding the effects of alloy composition on the times and temperatures for the various phase transformations and in understanding the transient nature of the observed phase equilibria.

CHAPTER 4: EXPERIMENTAL PROCEDURES

4.1. Sample Preparation

4.1.1. TTT Samples

CD3MN alloys denoted as $4A_1$, $4A_2$ and $4A_3$ were received from two separate commercial suppliers. CD3MWCuN alloys denoted as $6A_1$ and $6A_2$ were supplied from only a single supplier. Although the suppliers and batches are different, their chemical compositions are quite similar, as listed in Table. 4. Samples were provided in the form of keel bars of approximate dimensions 3 x 4 x 35*cm*. Small coupons about 4*mm* thick were sliced from sections of the bars by electrical discharge machining (EDM). A 3*mm* diameter hole was drilled at the top of each coupon in order to attach a wire for suspending the coupons inside the vertical furnace and salt bath. For long-time heat treatments some samples were encapsulated in quartz tubes filled with Ar gas in order to reduce the extent of oxidation. Encapsulated samples were somewhat smaller, having EDM prepared dimensions of about 4*mm*×6*mm* ×18*mm*.

Cast DSS alloys were received in the solution heat-treated condition from the foundaries. $4A_1$ samples were solution annealed between 1162°C and 1135°C for 1 hour and then subsequently water quenched. $4A_2$, $6A_1$, $6A_2$ samples were annealed at 1176°C for 4 hours, furnace cooled to 1079°C, and held for 1 hour and then water quenched.

All samples were re-heated to 1100°C at which the ratio of ferrite to austenite is predicted to be 50:50 vol.%.[36] This preheat treatment was done for 30 minutes, with the assumption being that the foundry heat treatment was sufficient to dissolve and homogenize

the structure, such that the follow-on treatment was simply to produce a common starting ferrite / austenite ratio.

Table 4. ASTM standard and measured compositions in wt.% of the steels used in this study.

	ASTM (CD3MN)	$4A_1$	$4A_2$	$4A_3$	ASTM (CD3MWCuN)	$6A_1$	$6A_2$
C	0.03_{max}	0.026	0.029	0.026	0.03_{max}	0.034	0.028
Mn	1.50_{max}	0.81	0.60	0.47	1.00_{max}	0.59	0.80
Si	1.00_{max}	0.66	0.65	0.57	1.00_{max}	0.87	0.75
P	0.04_{max}	0.014	0.025	0.024	0.03_{max}	0.023	0.03
S	0.020_{max}	0.0065	0.022	0.002	0.025_{max}	0.011	0.011
Cr	21.0-23.5	22.10	22.12	22.00	24.0-26.0	24.53	24.68
Ni	4.5-6.5	5.44	5.45	5.50	6.5-8.5	7.33	7.38
Mo	2.5-3.5	2.91	2.98	2.82	3.0-4.0	3.62	3.54
Cu	1.00_{max}	0.152	0.225	0.194	0.5-1.0	0.668	0.918
W	-	-	0.063	0.059	0.5-1.0	0.757	0.752
N	0.10-0.30	0.17	0.15	0.14	0.20-0.30	0.23	0.29
Fe	Bal.	Bal.	Bal.	Bal.	Bal.	Bal.	Bal.

A salt pot was used for short-term heat treatments. A Cylindrical alumina crucible was used for holding the salts. The salts used for the experiments were barium-chloride-based mixtures provided from Heat Bath Company, Indian Orchard, Massachusetts. Two

salts were used, with the working temperature range for the lower temperature salt (product name: Uni-Hard IR) being between 600°C and 920°C and that (product name: Sta-Hard 45) for the higher temperature experiments being between 850°C and 1150°C.

The temperature of the molten salt was varied between 600 and 950°C at an interval of 50°C. Five or six samples were suspended in the vertical furnace for preheat treatment, and then either dropped directly into the salt pot or, at times, caught and immediately placed into the salt bath. For samples that were caught and placed into the salt bath the transfer time was completed within 5 seconds. A schematic of the experimental set-up is shown in Fig. 23. Soak times in the salt bath ranged from 1 minute to 3 days. Samples removed from the salt bath were water quenched immediately. Long-time heat treatments to ensure equilibrium conditions at each soak temperature were performed using box furnaces. All soak temperatures were monitored by inserting a K-type thermocouple into both the salt pot and the box furnace. A complete listing of the heat treatment schedules is given in Table 5.

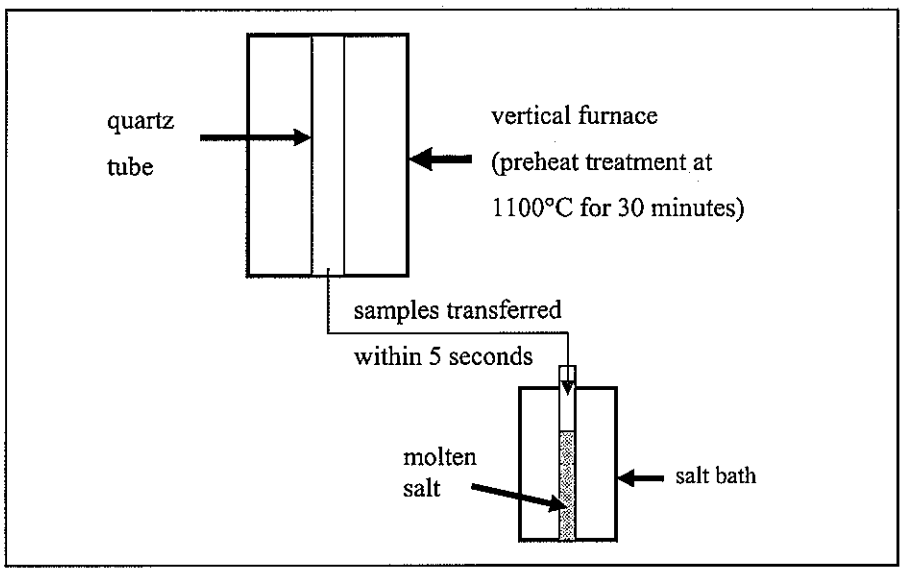

Fig. 23. Schematic experimental set up for isothermal heat treatments

Table 5. Heat treatment schedule for the different batches of alloys used in this study.

(a) CD3MN

Temp., °C	Time, minutes													
	1	10	30	60	120	300	480	720	1440	2880	4320	7200	18720	43200
700	■	■	■	■	■	■	▲	▲	▲	▲	●	▲	▲	▲
750	■	■	■	■	■	■	▲	▲	▲	▲	●	▲	▲	▲
800	■	■	■	■	■	■	▲	▲	▲	▲	●	▲	▲	▲
850	■	■	■	■	■	■	▲	▲	▲	▲	●	●	●	●
900	■	■	■	■	■	■	■	■	■	■	●	▲	▲	▲

●$4A_1$ ■$4A_2$ ▲$4A_3$

(b) CD3MWCuN

Temp., °C	Time, minutes							
	1	3	10	30	45	60	100	4320
700	●	●	●	●	■	■	●	●
750	●	●	●	●	■	■	●	●
800	●	●	●	●	■	■	●	●
850	●	●	●	●	■	■	●	●
900	●	●	●	●	■	■	●	●

●$6A_1$ ■$6A_2$

4.1.2. CCT Samples

For the continuous cooling study, encapsulated samples ($4A_2$ and $6A_1$ used) were heated to 1100°C at a rate of 20°C/*min* and then held for 30 minutes to homogenize the

starting microstructure. The samples were then cooled to room temperature at rates of 0.01, 0.1, 0.5, 1, 2, and 5°C/*min* using a programmable horizontal tube furnace. Such a furnace could not precisely control cooling rates faster than 5°C/*min* due to the absence of coolant. Thus, in order to achieve more rapid cooling profiles, a Bridgman furnace set-up was used. This type of set-up can decrease sample temperature by moving the position of the furnace relative to the sample such that the sample cooling rate is controlled by the furnace velocity. For this particular study, a furnace set at 1100°C was moved at fixed velocities of 0.1*mm/sec*, 0.15*mm/sec*, and 0.175*mm/sec,* which produced cooling rates between 10 and 40°C/min. Once the sample temperature was below 500°C it was water quenched to room temperature. Sample temperature was measured *in situ* using a type-K thermocouple inserted into the mid-point of the sample.

4.1.3. Thermo-Calc Study Samples

In order to assess the *Thermo-Calc* results obtained for the cast alloys CD3MN and CD3MWCuN, a series of alloys was designed with varying Cr, Ni and Mo contents, as shown in Table 6. Nine alloys were provided in the form of keel bars and then prepared in the same method as used for long time heat treatment in the TTT study described above. Each keel bar was poured at 1593°C (2900°F). Measured compositions of the steels are presented in Table 7. It is noted that each alloy was designed with the target compositions shown in Table 6, but Heat 6 could not be made due to difficulties during casting. The resulting alloy composition of Heat 6 is almost the same as Heat 5. The compositions of the other cast bars deviated little from what was targeted. Bars were solution heat treated at 1150°C for an hour followed by water quenching.

Small coupons about 4*mm* thick were sliced from sections of the bars. Each coupon was encapsulated in a quartz tube filled with Ar gas in order to reduce the extent of oxidation during long-time exposure at high temperature. A series of ten annealing temperatures was studied, from 825°C to 1050°C in intervals of 25°C. Samples were heat treated for 10 days to obtain maximum σ formation, then removed from the furnace and immediately quenched in water.

Table 6. Nominal (Target) compositions. (wt.%)

Alloys	Cr	Ni	Mo
CD3MN	22.5	5.5	3.25
Heat 1	20.0	4.0	3.75
Heat 2	25.0	4.0	3.75
Heat 3	20.0	7.0	2.75
Heat 4	20.0	7.0	3.75
Heat 5	25.0	4.0	2.75
Heat 6	25.0	7.0	2.75
Heat 7	20.0	4.0	2.75
Heat 8	25.0	7.0	3.75

Table 7. Measured compositions of the cast bars.

Alloys	Cr	Ni	Mo	C	Mn	Si	P	S	Cu	N
CD3MN	22.1	5.4	2.9	0.026	0.81	0.66	0.014	0.006	0.15	0.17
Heat 1	19.1	3.9	3.8	0.012	0.73	0.52	0.022	0.006	0.18	0.17
Heat 2	18.8	4.7	4.4	0.010	0.81	0.74	0.022	0.006	0.18	0.15
Heat 3	19.5	5.7	2.9	0.014	0.81	0.77	0.022	0.005	0.20	0.20
Heat 4	19.4	6.9	2.8	0.013	0.80	1.18	0.022	0.005	0.20	0.15
Heat 5	24.9	4.0	2.9	0.015	0.74	0.82	0.022	0.005	0.18	0.21
Heat 6	24.8	4.0	3.0	0.012	0.75	0.74	0.022	0.005	0.17	0.20
Heat 7	19.2	4.0	2.9	0.012	0.75	0.71	0.022	0.006	0.17	0.20
Heat 8*	25.0	6.9	3.9	0.014	0.72	0.64	0.022	0.006	0.14	0.18

* Composition of Heat 8 is close to ACI CD3MWCuN cast superduplex stainless steel

4.2. Sample Characterization

Heat treated samples were sectioned in the middle in order to examine their center, thereby avoiding any surface effects. Mounting was done using a LECO PR-25 hot mounting press with diallyl phthalate powder. The samples were polished using a Struer Prepmantic Polisher™ with 180-600 grit papers followed by a 1μm suspended diamond slurry solution. The samples were subjected to electrolytic etching with a sodium hydroxide solution (50g NaOH to 100mL H_2O) or potassium hydroxide solution (50g KOH to 100mL H_2O) at 6 volts for 10 seconds.[6] This electrolytic etching makes ferrite light blue in color

and the sigma phase a reddish brown. Carbides were identified by stain etching with Murakami's reagent (3g $K_3Fe(CN)_6$ + 10g KOH + 100mL H_2O), which causes them to turn black.[6]

An image analysis system, the MSQ image analysis system™ , was used to measure the amount of intermetallic (*i.e.,* assumed area fraction = volume fraction) in the optical cross-sectional images. The procedure used was to initially examine the entire surface of the sample to ensure that it appeared relatively homogeneous. Such a general examination was useful in determining the onset of precipitation since it was possible to observe very small amounts of precipitates, i.e., down to about 0.1 %. Once precipitation had proceeded to a measurable amount (about 0.5 %), ten areas were selected randomly at x200 magnification for image analysis. The area fraction was determined by the MSQ image analysis software using the following methodology. After an image was obtained a region of interest (and its associated color, contrast, and brightness levels) was specified simply by clicking the mouse on that region. The computer would then highlight all areas in the micrograph that exhibited the same color, contrast, and brightness as the point selected. If visually points were not included that the operator felt should be included, they could be added manually. Similarly, if regions were included that should not have been included they could be excluded by manually adjusting the contrast and brightness levels. It should be noted that the etch technique used tints the sigma and chi phases the same color. Therefore, the measured amount of intermetallic phase is more properly the amount of $\sigma+\chi$. The objective of selecting a region of interest is essentially to convert the multi-colored optical image to a binary image consisting of the selected color (in this case red) with everything else being considered "non-red." The computer then counted the number of "red" (denoting the $\sigma+\chi$)

versus "non-red" pixels and displayed the ratio of red to the entire number of pixels present in the image as the area percent, which is assumed equal to the volume percent. Such a method is essentially the same as outlined in ASTM standards E45, E562, and E1245, which are for manual point count analysis.

For phase identifications, Hitachi 3500N and JEOL 5910LV scanning electron microscopes (SEM) were used to take secondary electron images, back scattered electron images and electron dispersive spectroscopy (EDS). The acceleration voltages were set at 15kV or 20kV. An EDAX DX system with a sapphire detector attached on the Hitachi 3500N SEM was used to determine semi-quantitatively the phase compositions. The X-ray counts were kept at 2.8×10^3 counts per second and the live-time of acquisition was 100 seconds. A ZAF standardless quantification method was used for the quantification of the spectra. A more accurate determination of phase composition was carried out on polished bulk samples using an electron probe microanalyzer (EPMA) equipped with wavelength dispersive spectrometers (WDS).

Phase identification was also carried out using a Philips CM30 transmission electron microscopy (TEM) at 300 kV. For the phase identification, a CD3MN sample heat treated at 850°C for 30 days and a CD3MWCuN sample at 850°C for 3 days were analyzed, since these samples were expected to contain the greatest number of possible phases present. TEM foils were prepared using the jet polishing method. The solution used was 5% perchloric acid in 25% glycerol and 70% ethanol at a temperature of -20°C and a potential of 50 volts. An energy dispersive spectrometer (EDS) attached to the TEM was used for initial screening of the possible phases by semi-quantitative compositional analysis.

Each heat-treated sample was also Rockwell hardness tested using the B or C scale depending on the sample's hardness,[66] except for the Bridgman furnace samples which were too small for reliable Rockwell data. Those samples were tested using a diamond pyramid microhardness tester and converted to Rockwell.

CHAPTER 5: MICROSTRUCTURE CHARACTERIZATION

5.1. Introduction

Since DSS are highly alloyed steels, many secondary phases other than δ and γ may also form during either service or fabrication. As discussed in Chapter 2.3, typical secondary phases are secondary austenite (γ_2), carbides such as M_7C_3 and $M_{23}C_6$, and various types of intermetallic phases such as σ, χ, **R** and π. The most fundamental characterization to observe microstructure was carried out using optical microscopy together with tint-etching technique. Further phase characterization studies were undertaken using detailed scanning electron microscopy (SEM) and transmission electron microscopy (TEM) coupled with compositional analysis such as energy dispersive spectroscopy (EDS) and wavelength dispersive spectroscopy (WDS). Based upon various characterizing methods, the aim of this chapter is to clarify the phase identification of secondary phases formed in DSS alloys to produce accurate transformation curves.

5.2. Optical Microscopy

Metallographic examination of CD3MN samples showed that carbides can form at high temperatures and short soak times, while secondary austenite (γ_2) forms sympathetically at the primary austenite (γ_1)/ferrite boundaries. It was further shown that intermetallic phase forms at the γ_2/ferrite boundaries in the temperature range 700 - 900°C. Both γ_2 and the

intermetallic phase precipitates grew into the ferrite matrix. Typical micrographs and schematic illustration of intermetallic of CD3MN are shown in Fig. 24. Figure 25 shows the measured volume percent of intermetallic phase in CD3MN as a function of isothermal annealing time in the temperature range 700 - 900°C, with the corresponding data summarized in Table 8. It is seen in Fig. 25 that the extent of intermetallic phase formation as a function of time shows increasing volume percent after an incubation time, often called as sigmoidal, in accordance with the Avrami equation (Eq. 7).

Cross-sectional micrographs of the CD3MWCuN steel after different heat-treatment times are shown in Fig. 26. Intermetallic phase formation in CD3MWCuN initially occurred at ferrite/austenite grain boundaries and grew much more rapidly and extensively than in CD3MN, ultimately appearing eutectoid-like in structure at long aging time. According to color tint-etching, this morphology appears to be a consequence of the ferrite matrix decomposing to secondary austenite and intermetallic as illustrated schematically in Fig. 26. Figure 27 shows the amount of intermetallic formed as a function of isothermal hold time and temperature. As shown in Table 9 and Fig. 27, the equilibrium amount of intermetallic phase formed within only 3 days in comparison to 30 days for CD3MN.

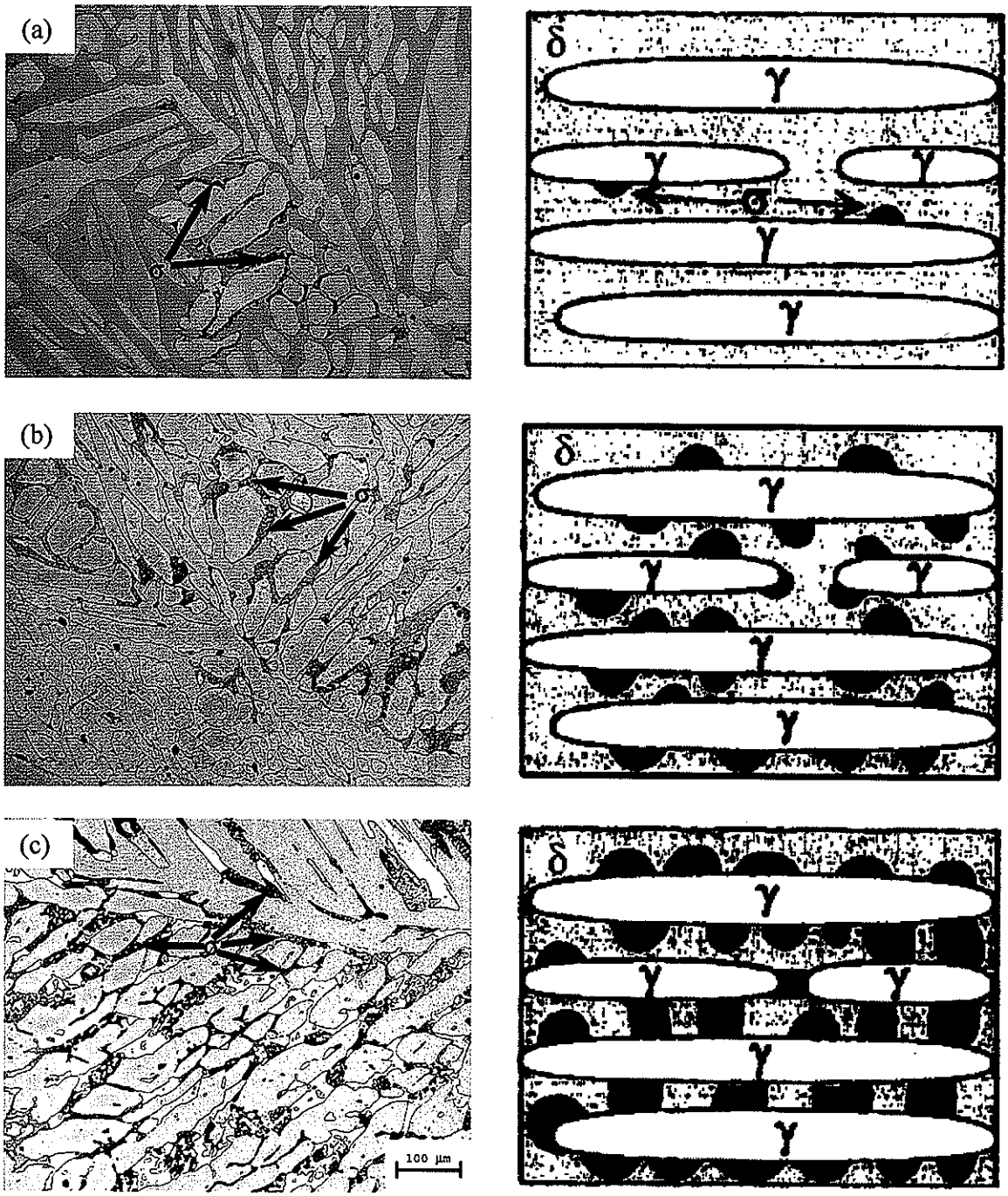

Fig. 24. Optical micrographs of the CD3MN with schematic illustration[51] of intermetallic precipitation mechanism after soaking for (a) 8, (b) 48 hours, and (c) 30 days at 900°C. N.B. the symbol σ may include a small amount of χ phase.

Table 8. Volume percent (or area %) intermetallic phase in CD3MN for soak time and temperature.

Time, min.	700°C	750°C	800°C	850°C	900°C
1	0 ± 0	0 ± 0	0 ± 0	0 ± 0	0 ± 0
10	0 ± 0	0 ± 0	0.07 ± 0.12	0 ± 0	0 ± 0
30	0 ± 0	0.02 ± 0.06	0.11 ± 0.13	0.26 ± 0.37	0.02 ± 0.05
60	0 ± 0	0.21 ± 0.44	0.71 ± 0.61	0.32 ± 0.19	0.01 ± 0.04
120	0 ± 0	0.30 ± 0.24	0.82 ± 0.50	0.50 ± 0.34	0.10 ± 0.09
300	0.03 ± 0.10	0.63 ± 0.49	1.08 ± 0.34	1.13 ± 0.44	0.13 ± 0.14
480	0.03 ± 0.03	0.77 ± 0.27	1.30 ± 0.19	2.07 ± 0.36	1.19 ± 0.97
720	0.04 ± 0.13	0.94 ± 0.51	1.73 ± 0.30	3.25 ± 1.24	0.87 ± 0.54
1440	0.14 ± 0.19	2.19 ± 0.30	2.79 ± 0.40	4.72 ± 1.98	1.57 ± 1.26
2880	0.25 ± 0.22	3.42 ± 1.16	8.54 ± 2.47	9.36 ± 2.46	4.28 ± 1.79
4320	1.43 ± 1.32	7.38 ± 0.83	10.09 ± 2.67	12.12 ± 3.63	7.13 ± 2.01
7200	2.24 ± 0.57	9.43 ± 2.35	12.58 ± 1.94	12.80 ± 1.61	11.42 ± 1.86
18720	6.13 ± 2.31	11.72 ± 2.54	11.37 ± 1.73	15.21 ± 2.92	13.33 ± 2.68
43200	6.64 ± 0.63	10.08 ± 0.88	11.75 ± 2.68	14.60 ± 2.77	14.39 ± 2.86

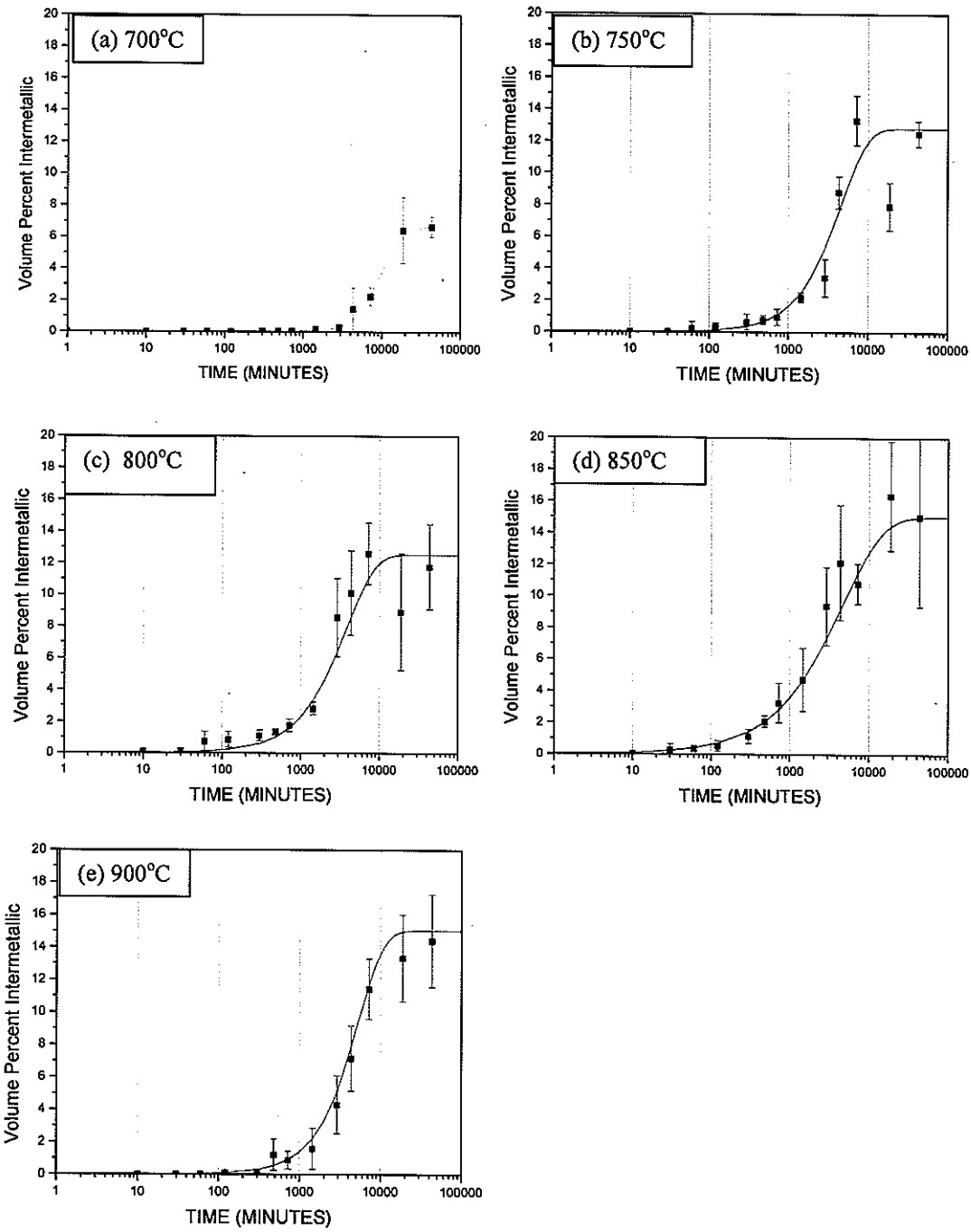

Fig. 25. The volume percent of intermetallic phase measured in CD3MN as a function of soak time at various temperatures.

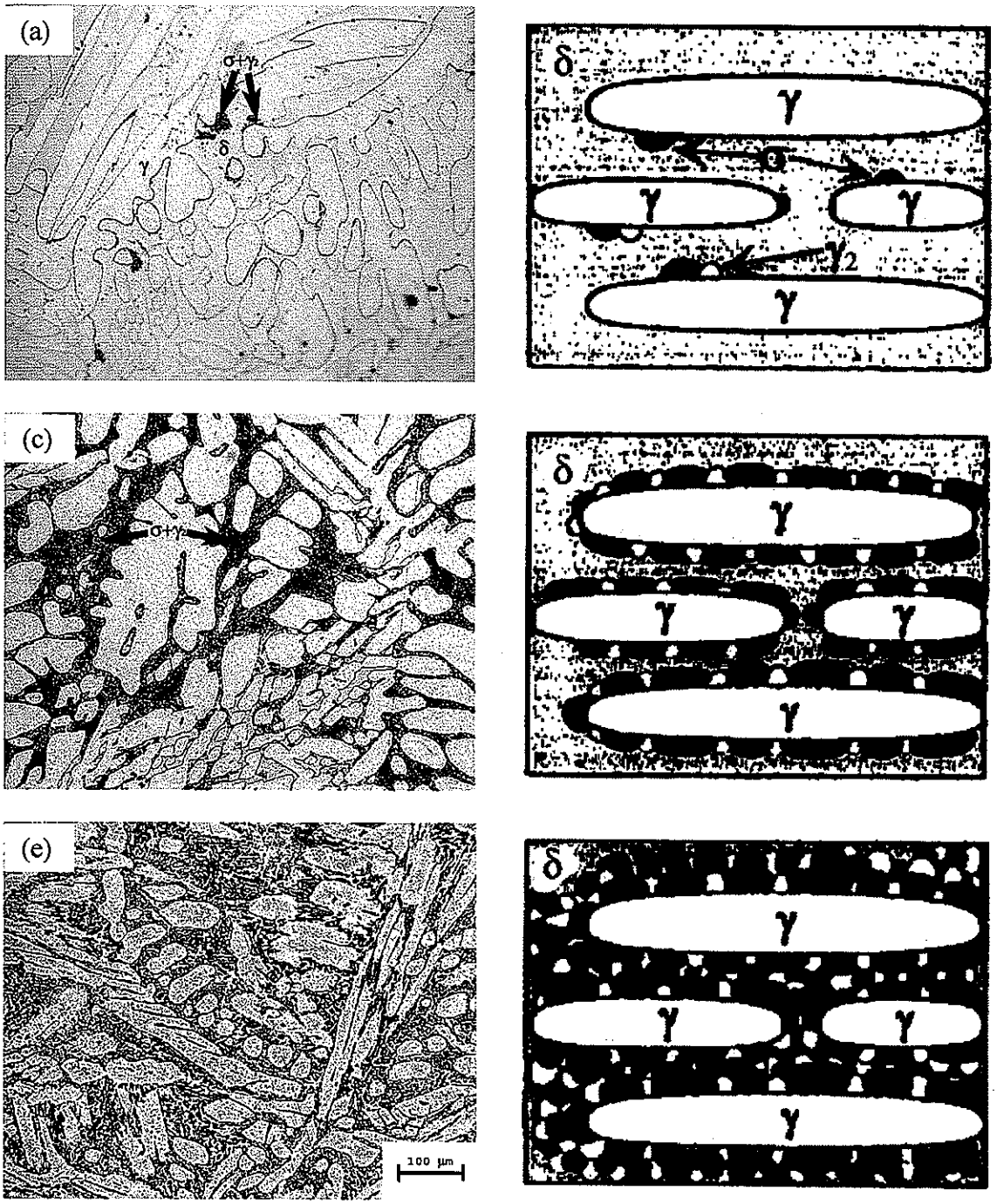

Fig. 26. Optical micrographs of CD3MWCuN with schematic illustration[51] of intermetallic precipitation mechanism after soaking for (a) 10, (b) 60, and (c) 4320 minutes at 900°C. N.B. the symbol σ may include a small amount of χ phase.

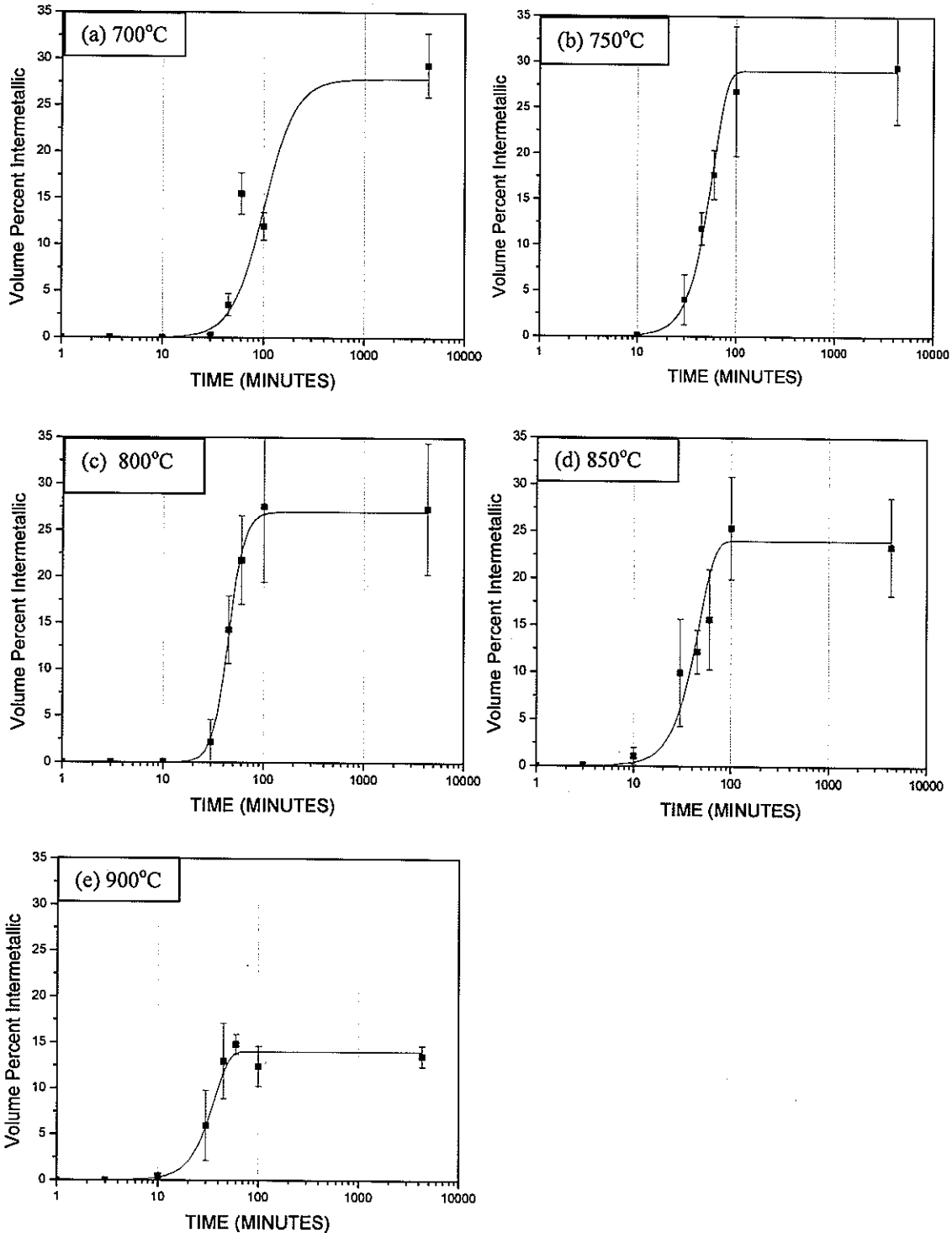

Fig. 27. The volume percent of intermetallic phase measured in CD3MWCuN as a function of soak time at various temperatures.

Table 9. Volume percent intermetallic phase in CD3MWCuN for soak time at various temperatures.

Time, min.	700°C	750°C	800°C	850°C	900°C
1	0	0	0	0	0
3	0	0	0	0.11 ± 0.11	0.02 ± 0.02
10	0	0.12 ± 0.19	0.09 ± 0.22	1.09 ± 0.89	0.49 ± 0.27
30	0.18 ± 0.39	4.01 ± 2.74	2.20 ± 2.38	9.95 ± 5.71	5.96 ± 3.19
45	3.53 ± 1.20	11.77 ± 1.80	14.27 ± 3.64	12.16 ± 2.33	11.34 ± 3.09
60	7.20 ± 1.60	17.67 ± 2.67	18.17 ± 3.99	15.61 ± 5.33	11.81 ± 0.93
100	13.99 ± 2.22	21.54 ± 2.84	23.42 ± 6.26	25.36 ± 5.47	12.41 ± 2.17
4320	20.35 ± 1.70	25.72 ± 3.25	28.48 ± 2.88	23.42 ± 5.21	13.53 ± 1.15

Intermetallic formation rate was much more rapid in CD3MWCuN than in CD3MN, with equilibrium amounts of intermetallic phase in the former also being much higher. This may be expected, since intermetallic phase formation is related to the concentration of Cr and Mo in the steel, both of which are present in greater amounts in CD3MWCuN. It has been reported that formation of an intermetallic phase such as sigma or chi can degrade the toughness and corrosion resistance of a duplex stainless steels when the amount present is greater than 5 vol.%.[27] Figures 28 and 29 show the time-temperature-precipitation (TTP) curves for 1, 5 and the final vol.% intermetallic in CD3MN and CD3MWCuN, respectively.

It is seen from these figures that the times to reach 5 vol.% intermetallic phase formation are almost two orders of magnitude longer for CD3MN than for CD3MWCuN. Specifically, 5 vol.% intermetallic phase forms in CD3MWCuN in as short as 20 minutes at about 850°C, while it takes a minimum of about 2000 minutes to form the same amount of intermetallic phase in CD3MN.[13, 25,26]

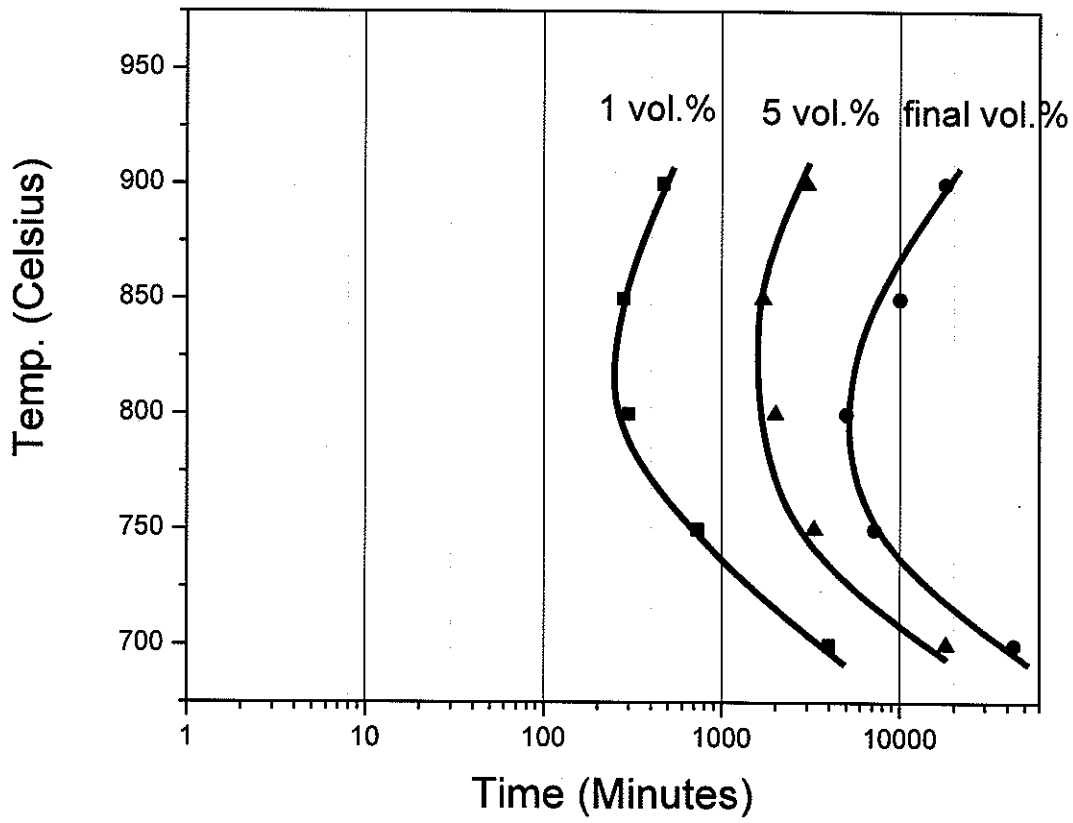

Fig. 28. Experimentally observed precipitation curves of CD3MN.

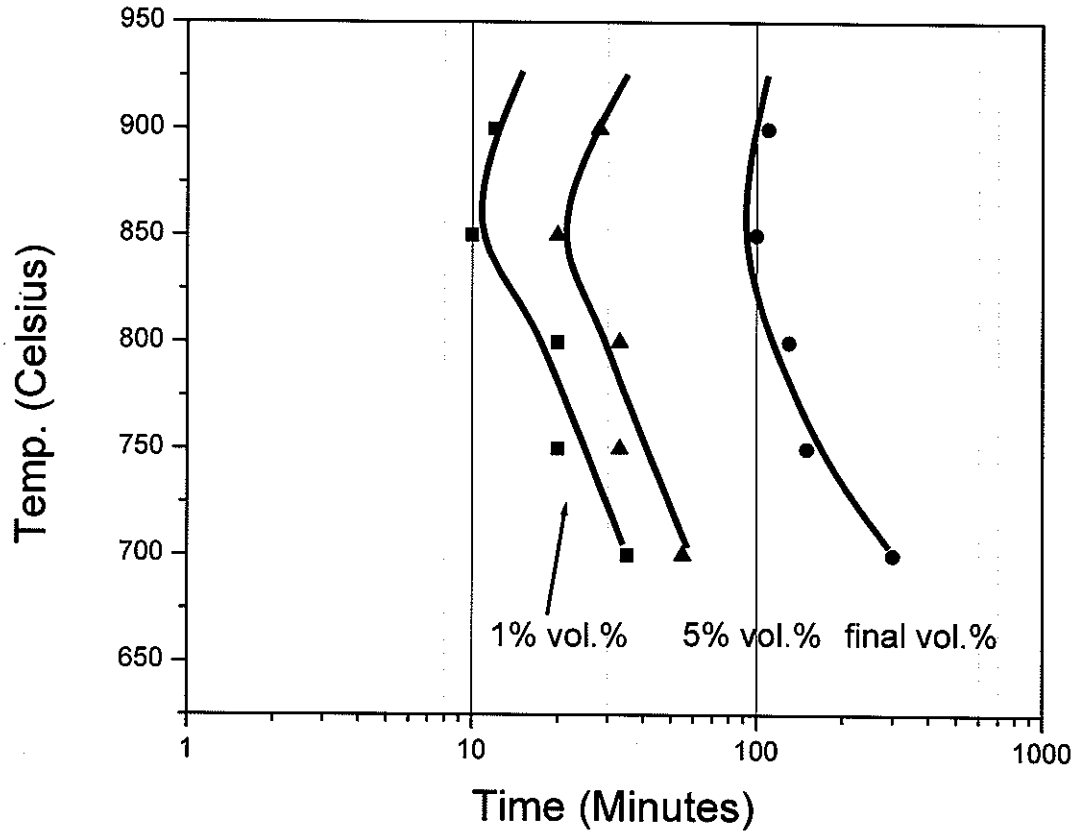

Fig. 29. Experimentally observed precipitation curves of CD3MWCuN.

5.3. SEM Analysis

The difficulty in differentiating between σ and χ in the optical images does not exist in BSE images. The contrast variations in BSE images due to atomic number differences in the phases, coupled with EDS measurements, allowed for accurate phase identification.

Specifically, while both σ and χ contain Fe, Cr, Mo and Ni as major elements, σ is a Cr-rich phase whilst the χ phase is Mo-rich. This causes the χ phase to appear brighter than σ in BSE images. Typical microstructures from CD3MN heat treated for 30 days at 850°C and CD3MWCuN heat treated for 3 days at the same temperature are shown in Fig. 30 (a) and (b), respectively. The matrix consists predominantly of γ and γ_2 (grey), with only small amounts of δ (dark grey) present in Fig. 30 (a). It is noted that δ was not present in a long-time heat treated CD3MWCuN (Fig. 30 (b)). The σ phase appears light grey and it is evident that σ grew at the expense of δ.

The small particles present at the γ_1 / γ_2 interface were assumed to be carbides due to their black appearance when using BSE imaging. Similarly, the white particles distributed through the grains were assumed to be a high Cr or Mo phase, possibly a nitride, due to their bright white appearance in BSE. Both types of particles were too small for accurate determination in the SEM using EDS. Subsequent TEM analysis (discussed in the following section) confirmed these phases to be $M_{23}C_6$ type carbide and Cr_2N, respectively. Fewer carbides and nitrides appear in the CD3MWCuN sample than in CD3MN.

Investigation of the chemical compositions of the major phases using WDS involved samples heat treated at short and long annealing times to effectively represent the start of precipitation and the establishment of equilibrium conditions. Concentrations of the major alloying elements such as Fe, Cr, Mo and Ni in δ, γ, σ and χ phases were seen to vary slightly with annealing time, as might be expected in a diffusional process. Typical results for short and long annealing times are summarized in Tables 10 and 11, respectively. It is noted that the composition of σ in CD3MN after 30 minutes annealing and χ in

CD3MWCuN after 10 minutes annealing could not be measured due to their small size. It is also noted that the amount of δ in CD3MWCuN after 3 days annealing was essentially zero. While the Cr content in δ and γ remains fairly steady in CD3MN, it must be remembered that δ phase is being consumed by the growth of σ and χ. As the high Mo and Cr intermetallics grow, depletion of these elements from γ results in a concomitant increase in Ni. Note that in the short-time annealed samples (i.e., 30 min. for CD3MN and 10 min. for CD3MWCuN) the amount of intermetallic phase present was so low it was difficult to discern in the SEM, even using BSE imaging, whether it was χ or σ simply on the basis of contrast. This is because with only a single phase present the contrast can be made to appear white or light grey in shade simply by varying the SEM contrast and brightness controls.

An isothermal section of Fe-Cr-Mo phase equilibrium diagram[60] shows the σ phase is stable over a wide range of composition variation, particularly with respect to Cr and Mo variation, and is very close to the χ phase field. Thus, in some cases the intermetallic phases observed may be either σ or χ. However, χ is especially rich in Mo when compared to σ, about 16-17 wt.% versus 5-6 wt% while σ is slightly enriched in Cr compared to χ. Therefore, the initial intermetallic phases that contained relatively high Mo (between 13-17 wt.%) are inferred to be χ, while those phase high in Cr (between 28-30 wt.%) are considered to be σ. Also, the composition of the intermetallic phase measured after 30 minutes in CD3MN is more closely aligned with that of χ, and it is therefore believed that this phase forms initially. Just the opposite is true for CD3MWCuN, where σ appears to form initially based on composition.

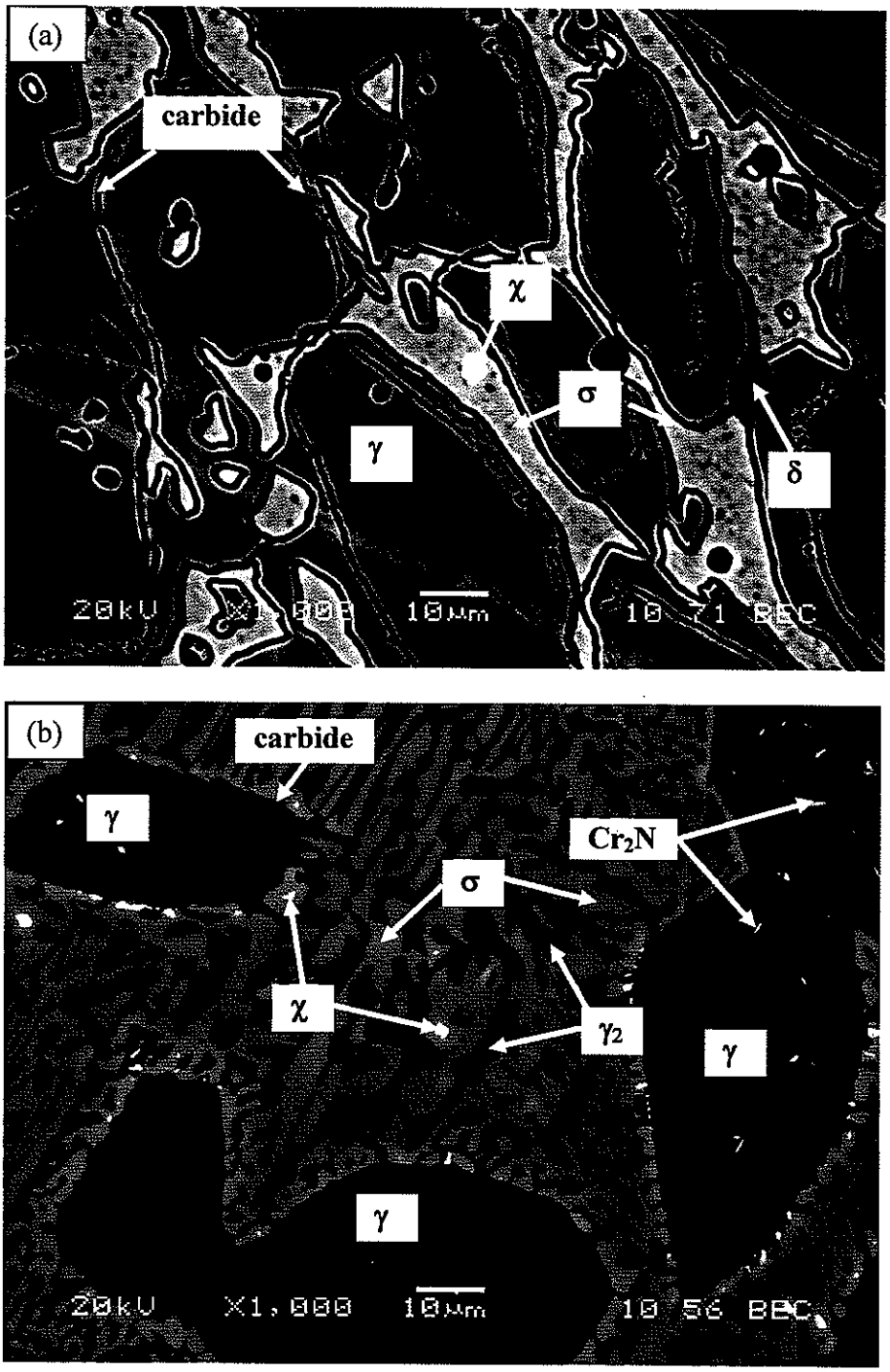

Fig. 30. Back scattered electron (BSE) image of (a) CD3MN annealed for 30 days and (b) CD3MWCuN annealed for 3 days. Chi phase brighter than sigma in BSE image.

Table 10. Composition (in wt.%) of CD3MN phases by WDS

(a) CD3MN sample annealed 30 minutes at 850°C.

phases	Fe	Cr	Ni	Mo	Si	Mn	W	Cu
δ	64.58 ±0.74	24.16 ±0.33	4.08 ±0.30	3.46 ±0.078	0.66 ±0.019	0.65 ±0.041	0.058 ±0.053	0.17 ±0.024
γ	66.09 ±0.70	21.11 ±0.21	6.51 ±0.090	2.18 ±0.033	0.57 ±0.027	0.74 ±0.036	0.031 ±0.035	0.22 ±0.028
σ	No data obtained							
χ	53.65 ±0.34	25.62 ±0.26	3.00 ±0.098	14.35 ±0.12	1.04 ±0.014	0.70 ±0.030	0.25 ±0.004	0.045 ±0.020

(b) CD3MN sample annealed 30 days at 850°C.

phases	Fe	Cr	Ni	Mo	Si	Mn	W	Cu
δ	67.93 ±2.88	24.12 ±1.63	2.23 ±0.27	2.36 ±1.37	0.68 ±0.10	0.39 ±0.045	0.027 ±0.025	0.093 ±0.032
γ	67.12 ±1.30	20.44 ±1.00	6.63 ±0.17	1.63 ±0.33	0.55 ±0.035	0.56 ±0.030	0.022 ±0.024	0.21 ±0.038
σ	56.85 ±0.79	31.78 ±0.48	2.01 ±0.14	5.64 ±0.27	0.95 ±0.023	0.45 ±0.035	0.064 ±0.037	0.042 ±0.031
χ	52.04 ±0.37	25.78 ±0.36	2.05 ±0.083	16.70 ±0.68	1.22 ±0.042	0.44 ±0.032	0.355 ±0.058	0.041 ±0.037

Table 11. Composition (in wt.%) of CD3MWCuN phases by WDS

(a) CD3MWCuN sample annealed 10 minutes at 850°C.

phases	Fe	Cr	Ni	Mo	Si	Mn	W	Cu
δ	58.52 ±1.36	26.62 ±0.60	5.66 ±0.26	4.18 ±0.43	0.85 ±0.032	0.60 ±0.033	0.70 ±0.087	0.56 ±0.065
γ	61.14 ±0.34	23.40 ±0.22	8.57 ±0.096	2.65 ±0.033	0.74 ±0.020	0.70 ±0.013	0.48 ±0.036	0.74 ±0.033
σ	55.92 ±1.45	28.36 ±1.29	5.06 ±0.42	5.49 ±0.99	0.94 ±0.053	0.64 ±0.039	0.91 ±0.15	0.40 ±0.10
χ	No data obtained							

(b) CD3MWCuN sample annealed 3 days at 850°C.

phases	Fe	Cr	Ni	Mo	Si	Mn	W	Cu
δ	Not present							
γ	61.43 ±1.00	22.65 ±0.60	8.48 ±0.55	2.31 ±0.16	0.69 ±0.043	0.68 ±0.048	0.39 ±0.036	0.88 ±0.051
σ	54.36 ±1.90	31.27 ±1.23	3.73 ±0.46	6.60 ±1.41	1.09 ±0.040	0.59 ±0.071	1.18 ±0.36	0.24 ±0.072
χ	50.85 ±0.39	26.66 ±0.46	2.78 ±0.023	15.10 ±0.83	1.17 ±0.013	0.57 ±0.001	2.69 ±0.19	0.15 ±0.018

The volume percentages of σ and χ were determined by analysis of BSE images similar to that of Fig. 30, and the results are shown in Figs. 31 and 32 for CD3MN and CD3MWCuN alloys, respectively. While it appears that χ may form initially in CD3MN, the amount remains extremely low when compared to σ. After 30 days annealing the amount of χ in CD3MN was a maximum at about 2 vol% at 800°C and about 1 vol% at 850°C. At 900°C, the amount of χ was essentially zero. This makes it difficult to determine with any certainty that equilibrium was reached. For CD3MWCuN, in which it appeared that σ forms first, the amount of χ was also small, even less than seen for CD3MN. The maximum amount was about 1.5 vol% at 800°C. At 900°C and 750°C, χ was not found after 3 days heat treatment. The kinetic curves for σ formation are approximately sigmoidal in shape, more nearly matching the results of previous optical studies.

The precipitation curves representing 1 vol.% of σ and χ in CD3MN and CD3MWCuN are plotted in Figs. 33 and 34, respectively. The 1 vol% intermetallic phase precipitation curve (σ+χ) previously determined from optical studies is included for comparison. The noses of the σ and χ curves match the previously reported curve fairly well; although, the 1 vol.% σ curve is displaced to shorter times while χ is displaced to longer times for CD3MN. The maximum formation temperature of χ for the times studied is located at approximately 900°C; although, the amount seen at this temperature never reached the 1 vol% level. For CD3MWCuN, the noses for the σ and χ phases were located at longer times than for the optically determined σ+χ curve. The nose for the χ phase appeared at a lower temperature than that for the σ phase. The temperature range for χ phase formation is between 750 and 900°C.

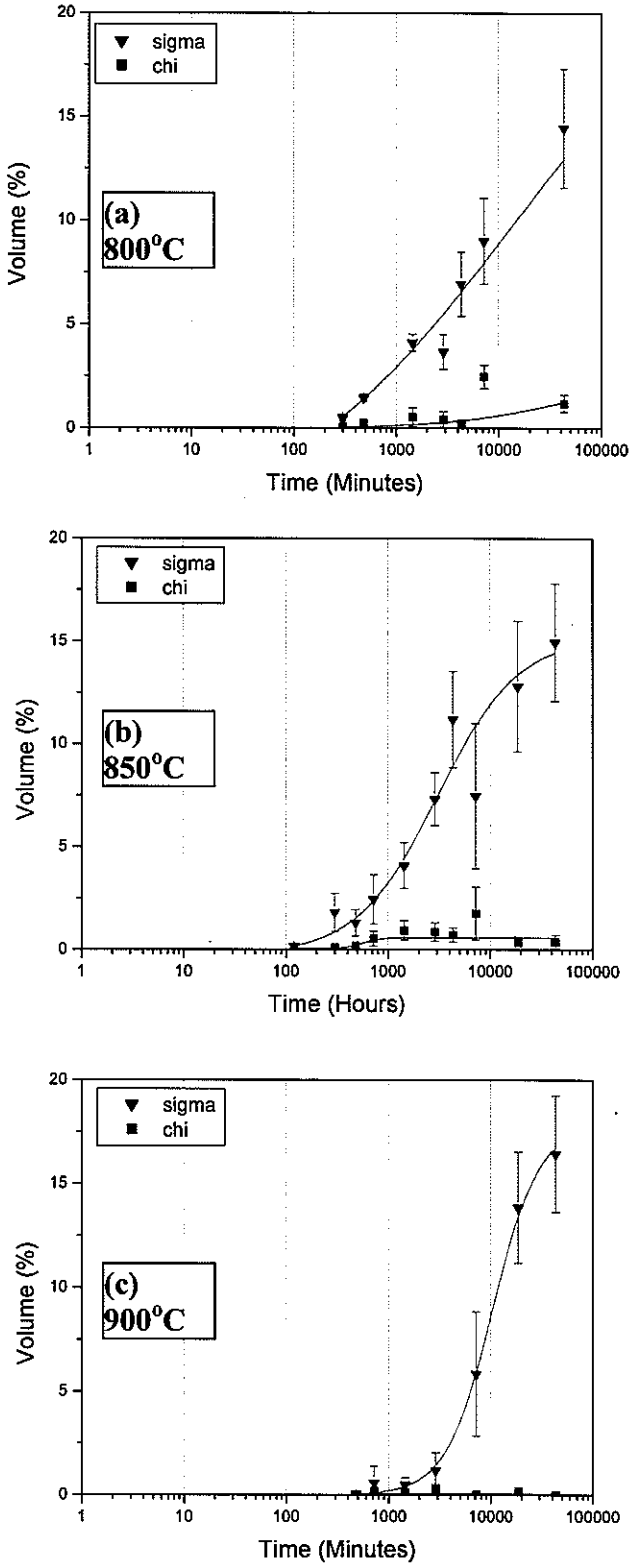

Fig. 31. Volume percent of σ and χ at (a) 800°C, (b) 850°C, and (c) 900°C.

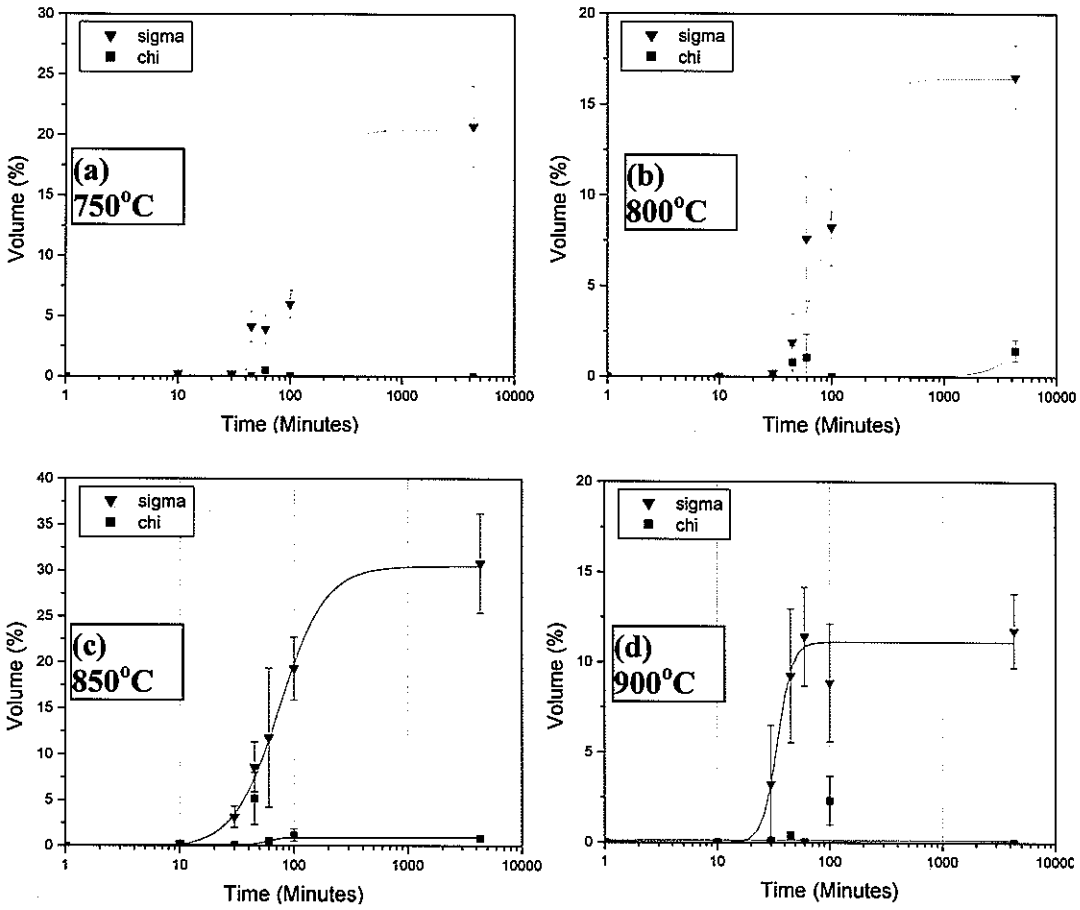

Fig. 32. Volume percent of σ and χ at (a) 750°C, (b) 800°C, (c) 850°C, and (d) 900°C in CD3MWCuN.

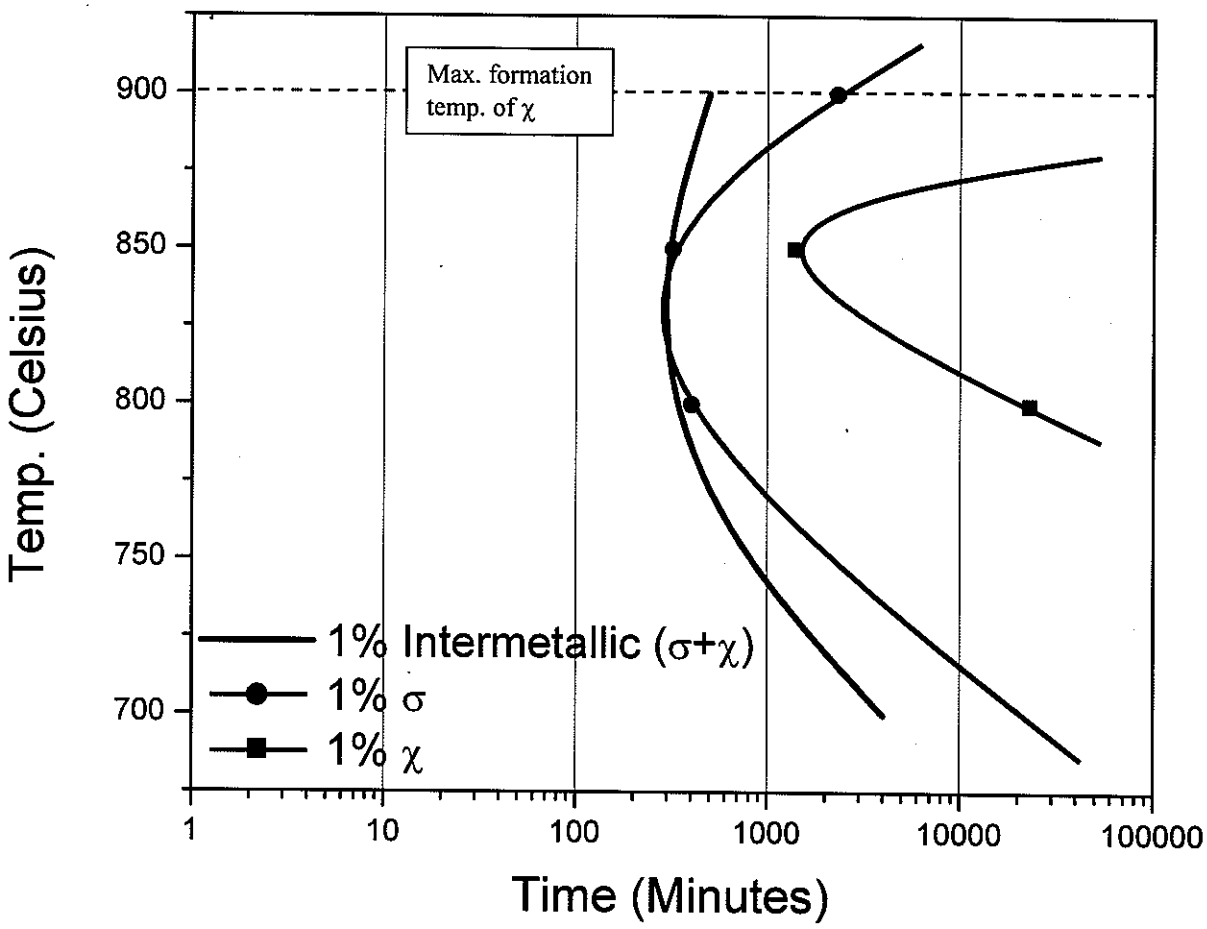

Fig. 33. Initial (1 vol.%) precipitation curves of σ and χ phases superimposed intermetallic (σ+χ) curve determined by optical microscopy study (Fig. 28).

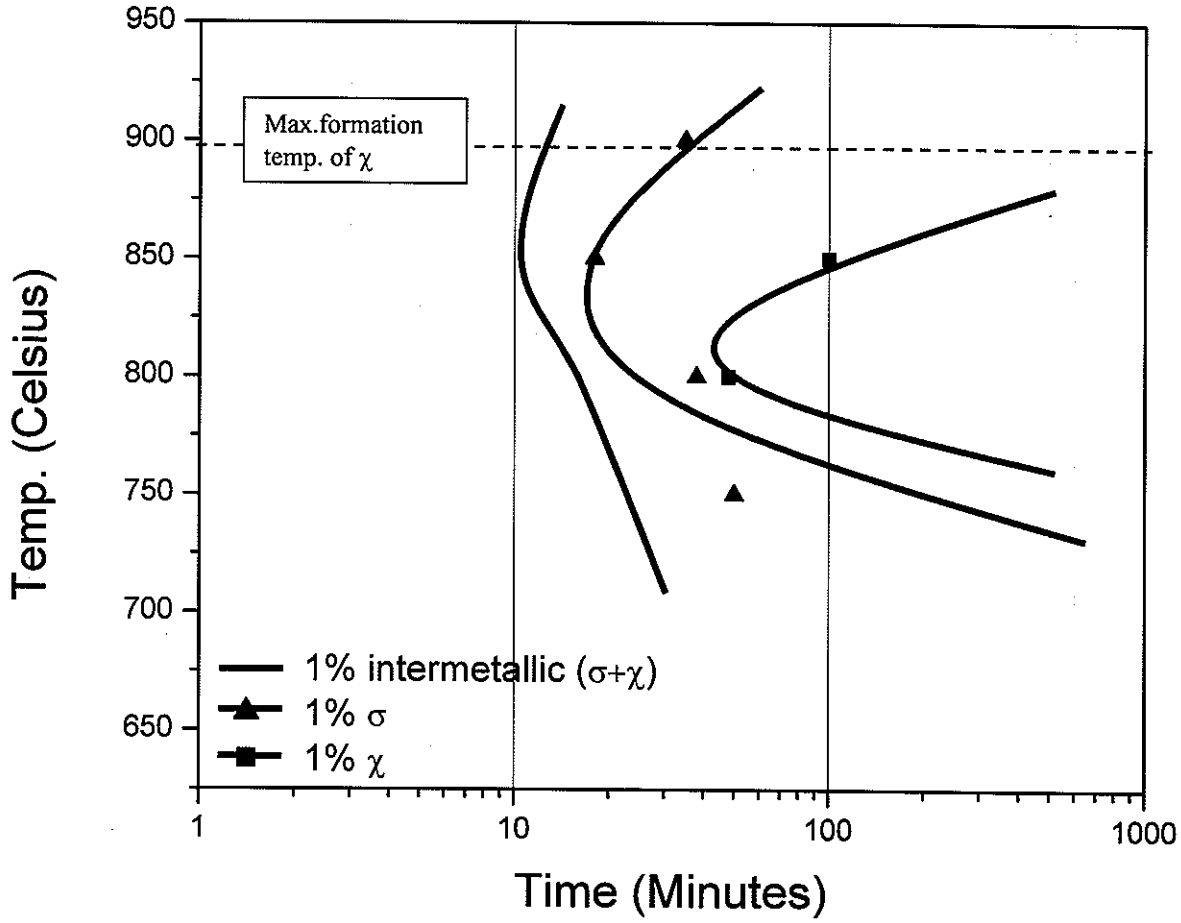

Fig. 34. Initial (1 vol.%) precipitation curves of σ and χ phases for CD3MN superimposed on the TTT intermetallic (σ+χ) curve determined by optical microscopy study (Fig. 29).

The composition studies summarized in Tables 10 and 11 indicate that χ is most likely the first intermetallic phase to form in CD3MN. SEM examination (e.g. Fig. 30) showed the χ phase to be associated with σ in previously δ-ferrite regions, in many cases appearing inside the σ. Such an assemblage would result if χ formed initially, followed closely by nucleation and rapid growth of σ phase at the χ / δ interface. The extremely slow growth of χ as opposed to σ causes the 1 vol.% precipitation line to be displaced significantly to the right in comparison to that for σ phase, even though initial nucleation may occur in the reverse order. In the case of CD3MWCuN the composition of the initial precipitates is closer to that of σ than χ; however, observation of Fig. 30 again shows a small number of χ precipitates appearing inside larger σ regions. It thus appears that the nucleation of σ and χ occurs essentially at the same time.

The major elements for stabilizing the σ and χ types of intermetallic phase are Cr and Mo. As shown in Tables 10 and 11, σ contains about 32 wt.% Cr but only 4-6 wt% Mo, while χ contains about 16 wt.% Mo. Such a high Mo content is difficult to achieve from the relatively small overall amount of about 3 wt.% Mo present in the alloy. Therefore, while χ may precipitate faster than σ, only limited amounts can be observed, unlike the relatively high volume percentage of σ. Since the Cr content in the alloy is high (about 22-25 wt.%), large amounts of σ can formed.

The discrepancy between the position of the intermetallic start curve determined using optical microscopy and the results obtained using SEM are undoubtedly related to the techniques used and the number of samples examined. SEM allowed higher magnifications to be employed so small precipitates that may have been hard to distinguish using tint-

etching and an optical microscope were easily revealed in the SEM, and this may account for the displacement of the initial precipitation curve to the shorter times when analyzing by SEM. In a similar manner, regions thought to be σ using optical means could be revealed as pits or inclusions using the higher resolution SEM. These possible variations, coupled with the minor variations that must be expected when examining different samples and areas, can easily account for the discrepancies.

The extremely low amounts of χ observed make it difficult to reliably plot initial and final curves for this phase. The 1 vol. % curve was plotted in Figs. 33 and 34 to show the existence of such a phase. Temperature range for precipitation was found to be between 750°C and 900°C, which is narrower than what was found for the σ phase. The location of the nose was found to be similar to that seen for the same amount of σ phase, only slightly lower and delayed in time.

5.4. TEM Analysis

Identification of the precipitate phases in the cast alloys was initially determined using EDS to locate potential regions in the sample for detailed electron diffraction analysis. Once a region was identified a combination of selected area diffraction (SAD) and convergent beam electron diffraction (CBED) was used, with the results being compared to the crystallographic information listed in Table 12.[27] In terms of microstructural evolution, the DSS alloys contain approximately a 50:50 ratio of ferrite and austenite at the beginning of isothermal transformation. As heat treatment time increases at a fixed temperature,

secondary phases such as γ_2, σ and χ start to form at δ/γ interphase boundaries between δ and γ. At long times the δ ferrite is totally consumed by the formation of intermetallic compounds.

The most commonly observed precipitate phase in both CD3MN and CD3MWCuN was σ. An example of a σ precipitate in the CD3MN steel is shown in Fig. 35, which also includes a selected area diffraction (SAD) pattern from the [100] zone axis. The χ phase (Fig. 36) was also observed but to a much lesser extent. Both χ and σ phases appeared large and relatively equi-axed, as might be expected if they were growing at the expense of an equi-axed δ ferrite grain. Regions of χ were found adjacent to σ grains in 3-day annealed CD3MWCuN alloy (Fig. 37(a)), and diffraction analysis indicated an orientation relationship between the two phases. Figure 37 (b) shows a SAD pattern from overlapped σ and χ phases, the zone axis of [001] for both phases. Since the planar spacing of the χ phase (cubic with a=8.92 Å) is nearly double that of the c-axis planar spacing of the σ phase (tetragonal with a=8.79 Å, c=4.54 Å), the diffraction patterns on the [001] zone axis appear overlapping. The deduced orientation relationship at the interface in this instance is $(001)_\sigma//(001)_\chi$ although other possible orientation relationships have been reported.[59]

A number of small roughly circular precipitates were also found in both alloys. Cr-rich particles identified as an $M_{23}C_6$-type carbide (Fig. 38) were present throughout the CD3MN sample. These precipitates were usually observed at γ grain boundaries. Also identified were Cr_2N precipitates, Fig. 39. These precipitates usually occurred in small clusters or groups of several precipitates, often somewhat aligned. The appearance of both carbides and nitrides matched well with the phases seen using the SEM (see Fig. 30) and

were more difficult to find in the CD3MWCuN TEM samples, also in agreement with SEM observations. Other types of secondary phases listed in Table 12 such as M_7C_3, R, and π phases were not observed in the current investigation in either CD3MN or CD3MWCuN. Table 13 compares the lattice parameters calculated from diffraction patterns obtained in this study to those obtained from the references. The contents of the major elements, as determined semi-quantitatively using EDS in the TEM, are also listed in this table.

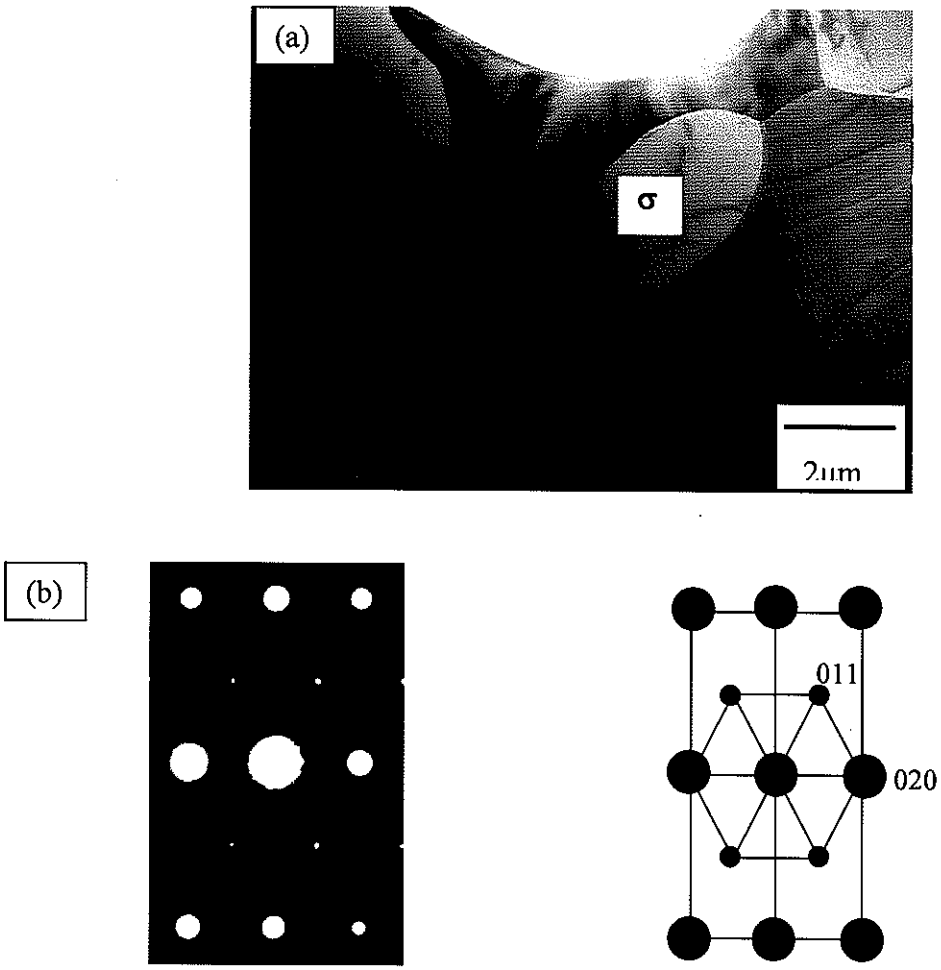

Fig. 35. (a) bright field image of σ phase in a 30 days heat treated CD3MN DSS, (b) SAD pattern from σ phase with [100] zone axis.

Table 12. General information on common secondary phases in duplex stainless steels.[27]

Phases	Lattice Type (Sturucture Type)	Space Group (Pearson Symbol)	Lattice Parameter (Å)	Temp. Ranges (°C)	Properties
δ	BCC (W)	Im3m (cI2)	a=2.86-2.88	all temp.	high corrosion resistance
γ/γ_2	FCC (Cu)	Fm3m (cF4)	a=3.58-3.62	700-900(γ_2)	high mechanical properties, γ_2 may have eutectoid morphology.
σ	Tetragonal (CrFe)	$P4_2/mnm$ (tP30)	a=8.79, c=4.54	600-1000	detrimental for mechanical, corrosion
χ	Cubic (Mn)	I43m (cI58)	a=8.92	700-900	similar to sigma, but higher Mo content (≈20%)
R	Rhombohedral (Mo)	R3 (hR53)	a=10.90, c=19.34	550-800	Mo rich(≈40% at the maximum) phase, detrimental
π	Cubic (Mn)	$P4_132$ (cP20)	a=6.47	600	detreimental to toughness and pitting corrosion resistance
Cr_2N	Hexagonal (Fe_2N)	P31m (hP9)	a=4.80, c=4.47	700-900	detrimental to corrosion resistance
$M_{23}C_6$	Cubic (C_6Cr_{23})	Fm3m (cF116)	a=10.56-10.65	<950	less important than other phases due to low carbon content in DSS or super DSS
M_7C_3	Orthorhombic (C_3Cr_7)	Pnma (oP20)	a=4.52, b=6.99, c=12.11	950-1050	

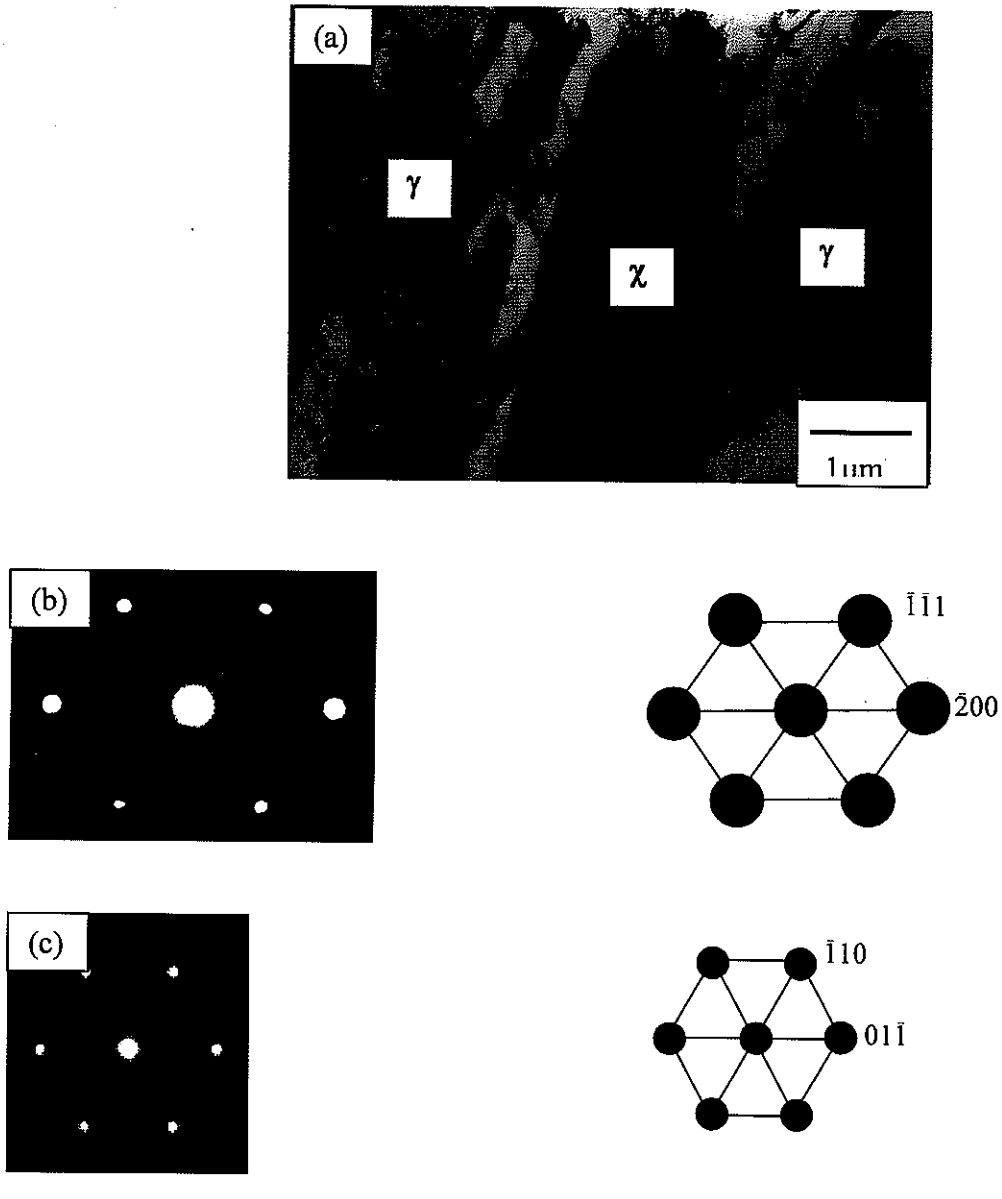

Fig. 36. (a) bright field image of γ and χ phases in a 30 days heat treated CD3MN DSS, (b) SAD pattern from γ phase with [011] zone axis, (c) SAD pattern from χ phase with [111] zone axis.

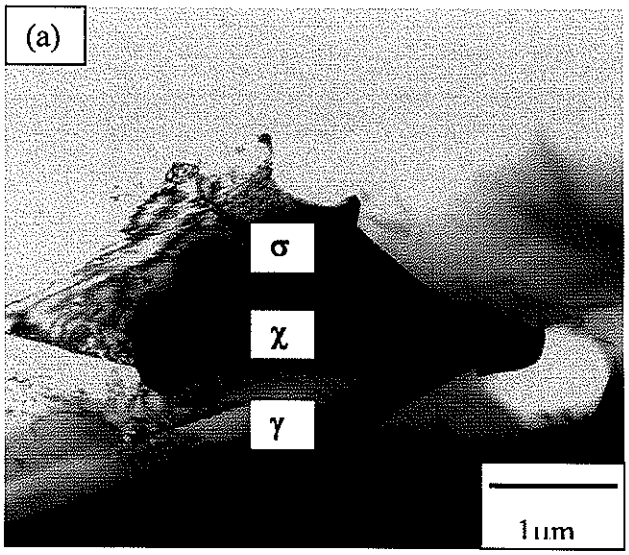

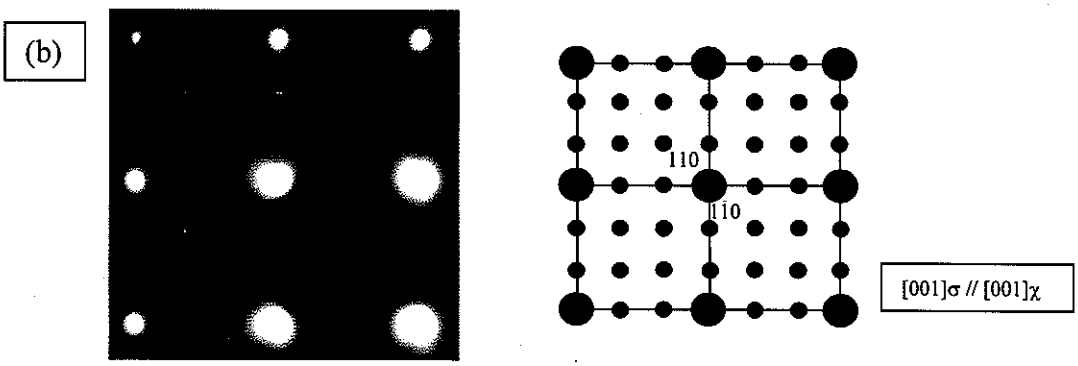

Fig. 37. (a) bright field image of σ phase including χ phase in a 3 days heat treated CD3MWCuN DSS, (b) SAD pattern from overlapped σ phase and χ phase with [001] zone axis.

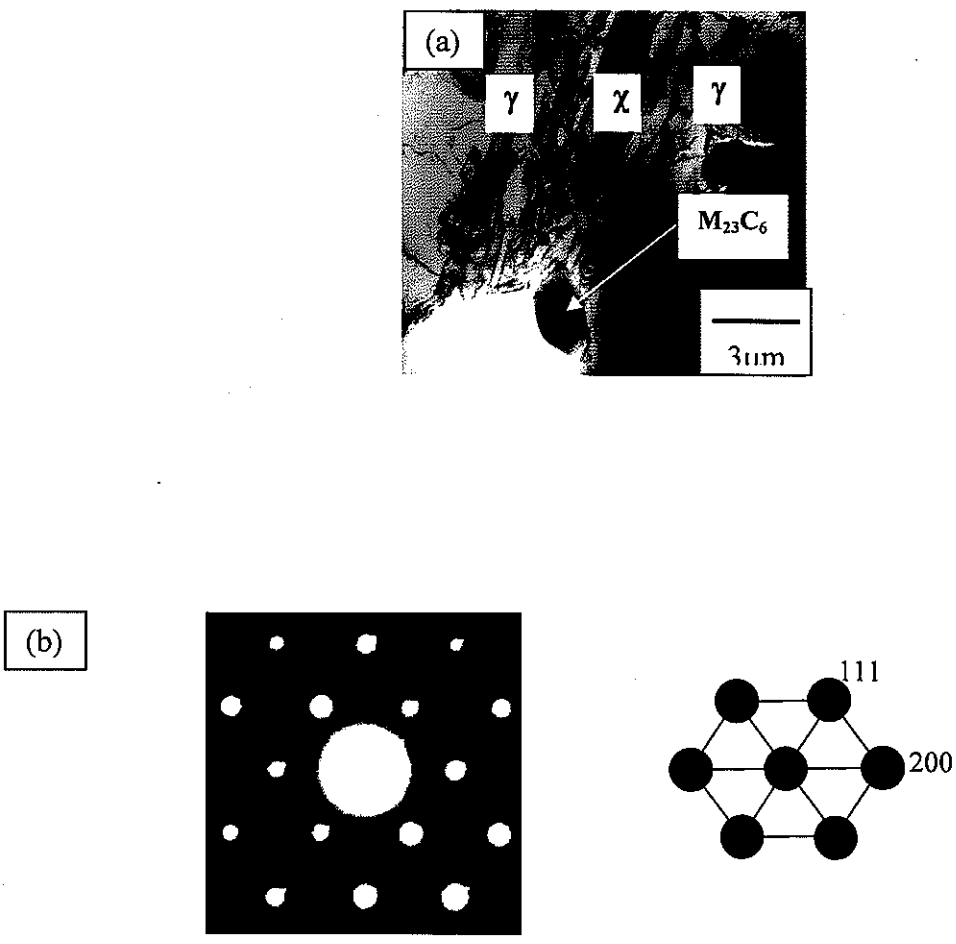

Fig. 38. (a) bright field image of $M_{23}C_6$ phase in a 30 days heat treated CD3MN DSS, (b) SAD pattern from $M_{23}C_6$ phase with $[0\bar{1}1]$ zone axis.

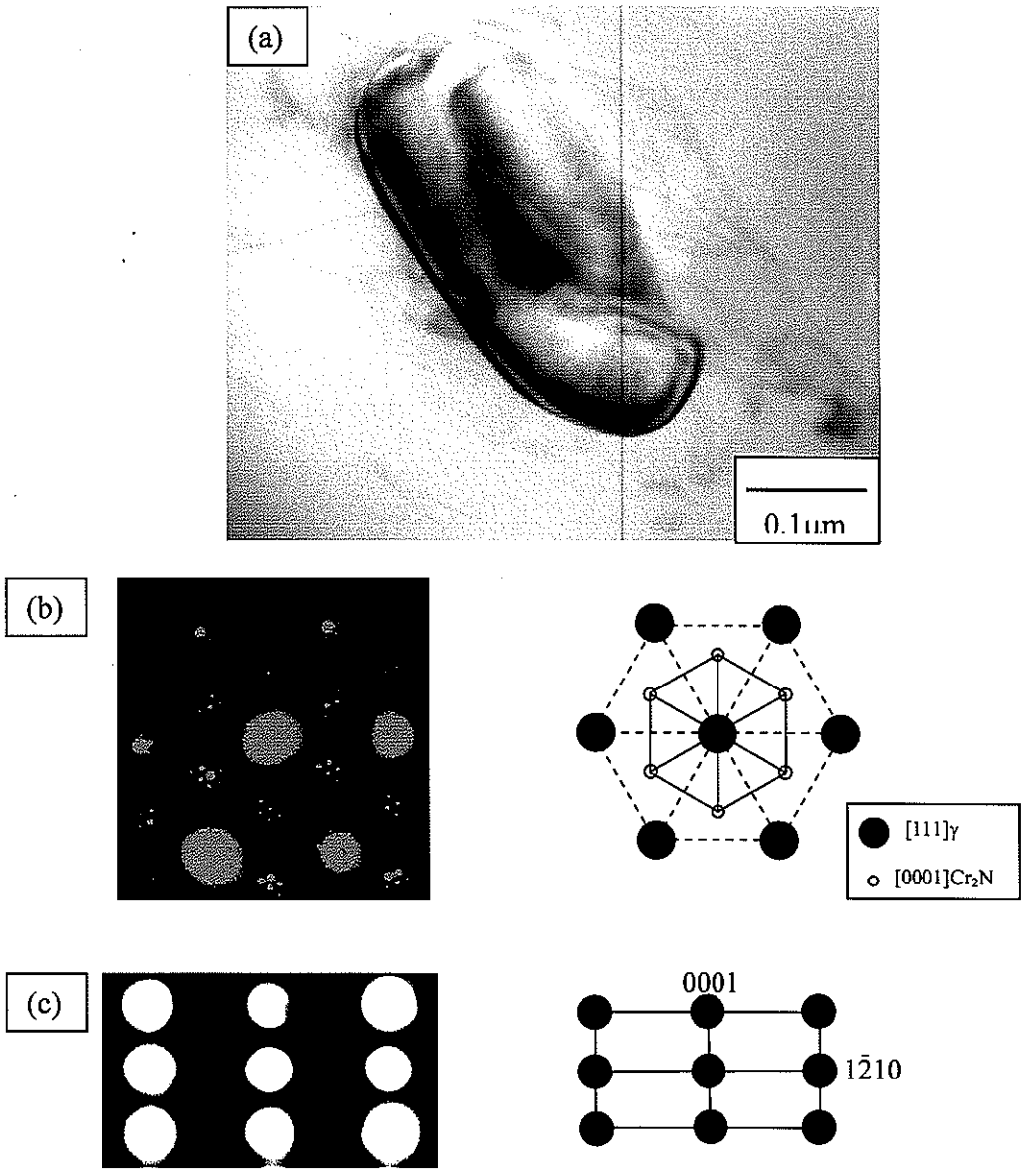

Fig. 39. (a) bright field image of Cr_2N phase in a 30 days heat treated CD3MN DSS, (b) SAD pattern from Cr_2N phase with [0001] zone axis with schematic SAD patterns overlapping [111] zone axis of γ and [0001] zone axis of Cr_2N, and (c) convergent beam diffraction patterns taken at [10$\bar{1}$0] zone axis of Cr_2N.

Table 13. Calculated lattice parameters of phases identified.

Phases	Reference Lattice Parameter, Å	Experimental Lattice Parameter, Å	Composition measured by EDS (in wt.%)
γ/γ_2	a=3.58-3.62	a≈ 3.61	70Fe-21Cr-6.0Ni-1.5Mo
σ	a=8.79, c=4.54	a≈8.83 , c≈4.55	56Fe-35Cr-4.5Ni-2.8Mo
χ	a=8.92	a≈8.89	51Fe-24Cr-2.1Ni-21Mo
Cr_2N	a=4.80, c=4.47	a≈4.70, c≈4.47	8.6Fe-88Cr-2.8Mo (N omitted)
$M_{23}C_6$	a=10.56-10.65	a≈10.67	21Fe-61Cr-1.2Ni-11Mo-5.0C

The phases identification from TEM analysis agree with what has been previously reported in DSS.[27] Although the M_7C_3, R and π phases were not seen, this is not to say they were not present. However, it can be said that the amounts of these phases were sufficiently low to escape attention in this study. This would indicate that they play little or no role in determining the mechanical and corrosion properties of these alloys and did not affect the kinetics of microstructural evolution.

5.5. Conclusions

Microstructure characterization was carried out using SEM and TEM equipped with EDS and WDS. Phases identified include γ, δ, σ, χ, $Cr_{23}C_6$ and Cr_2N. Detrimental

secondary phases such as σ and χ phases formed by migration of alloying elements especially Cr and Mo. At equilibrium, i.e., after a long term annealing, σ phase is the predominant intermetallic, with minor amounts of χ. According to WDS analysis, σ is rich in Cr, approximately 31 wt.%, while χ is rich in Mo, approximately 16 wt.%. Both phases seem to be forming at approximately the same time.

Resulting initial precipitate curves of σ and χ showed slight variations between the results from SEM and one which employed optical microscopy. The maximum χ phase formation temperature is lower than σ phase.

CHAPTER 6: JOHNSON-MEHL-AVRAMI (JMA) ANALYSIS FOR ISOTHERMAL TRANSFORMATION

6.1. Introduction

Theoretical analysis of intermetallic phase formation in both alloys was carried out employing the Johnson-Mehl-Avrami (JMA) equation. For this analysis the results from optical microscopy were used rather than from SEM examination for the following reasons. First, the amount of data available from optical samples was much greater than from SEM samples, which should provide for more accurate results. Second, although both σ and χ phases exist, SEM shows that the amount of χ is small when compared to the amount of σ observed, with the former never reaching more than approximately 1 vol.%. And finally, both phases act to embrittle the steel so from a practical standpoint the rate of total amount of intermetallic formation is more important than the respective rates for the individual phases. Therefore, σ and χ phases were considered collectively, *i.e.*, optical microscopy, for the JMA analysis.

6.2. CD3MN Alloy

Table 14 lists the equilibrium volume percentages and the calculated n and k values, obtained by using Equations 8 and 9 (Chapter 2), for the various soak temperatures. In order to use those equations the precipitation curves shown in Fig. 25 were fit with sigmoidal

shaped curves. Two points were then selected from the sigmoidal fit and the two unknown variables, n and k, were determined using Eqs. 8 and 9 on the basis of having two equations and two unknowns. To check the reliability of the values obtained, k and n were systematically varied and the Avrami equation used to re-plot a sigmoidal curve. This curve was then compared to the experimental data to see if it remained within the error bars associated with each measurement of the volume percent intermetallic. An example of this is shown in Fig. 40, which shows the 700°C data for CD3MN. In this example, the n value could only be varied in the range 2.55-2.62 for the 700°C curve and have the calculated sigmoidal curve from the Avrami equation remain within all experimental error bars. In a similar way, average k values could be varied from $2.3\text{x}10^{-11}$ to $5.3\text{x}10^{-11}$ min^{-n} and still remain within the experimental error ranges noted for the 700°C curve. This shows that the Avrami equation is very sensitive to changes in n value, suggesting that the average n values reported in Table 14 obtained at various heat treatment temperatures are reliable to approximately ± 0.05. Similarly, for k the expected error is between $\pm 10^{-11}$ and 10^{-5}.

The corresponding Avrami curves are shown in Fig. 41. The times separating the limits in a given Avrami curve, *i.e.*, $f \approx 0$ and $f \approx 1$ represent the start and finish times for the transformation. For the curves shown in Fig. 41, intermetallic formation was fastest at 850°C and slowest at 700°C. The calculated n values in Table 14 range from 1.4 to 2.6, indicating that the intermetallic formation is diffusion controlled, with the intermetallic phase precipitates forming at a small nucleation rate and growing from small dimensions.[14]

The Avrami equations that were determined were further used to establish TTT curves for 1%, 50% and 99% intermetallic phase transformation. The results are shown in Fig. 42. Conventionally, the initial curve is representative of 1% transformation and the final

curve is regarded as 99% completed. The nose of the initial curve is located in the temperature range 800°C and 850°C at a time of about 70 minutes.

6.3. CD3MWCuN Alloy

The same methodology was used for solving exponents in the Avrami equation for CD3MWCuN alloy. The results are listed in Table 15, and the corresponding Avrami curves are shown in Fig. 43. Calculated *n* values range from 2.7 to 3, indicating diffusion-controlled intermetallic phase formation, as found for CD3MN; however, the *n* values for CD3MWCuN further suggest that intermetallic phase formation takes place with precipitates forming at constant and/or increasing nucleation rates and growing from small dimensions.[14]

Figure 44 shows a TTT diagram for CD3MWCuN that was constructed using the Avrami equations determined in this study. As done for CD3MN, TTT curves for 1% (initial), 50% and 99% (final) intermetallic phase transformation are plotted. The nose of the initial curve is located between around 850°C and 900°C in as short as 5 minutes.

Table 14. Avrami analysis results for the CD3MN alloy.

Temp., °C	V_e, %	k, $min.^{-1}$	n
700	~6.7	$(3.0 \pm 1.3) \times 10^{-11}$	2.6 ± 0.05
750	~10.0	$(3.5 \pm 0.7) \times 10^{-6}$	1.5 ± 0.05
800	~11.5	$(6.3 \pm 1.0) \times 10^{-6}$	1.5 ± 0.05
850	~14.0	$(2.0 \pm 1.3) \times 10^{-5}$	1.4 ± 0.05
900	~15.0	$(7.8 \pm 0.9) \times 10^{-6}$	1.4 ± 0.05

Table 15. Avrami analysis results for the CD3MWCuN alloy.

Temp., °C	V_e, %	k, $min.^{-1}$	n
700	~20	$(1.6 \pm 0.8) \times 10^{-6}$	3 ± 0.05
750	~24.5	$(1.8 \pm 0.8) \times 10^{-5}$	2.7 ± 0.05
800	~27	$(2.2 \pm 0.5) \times 10^{-5}$	2.7 ± 0.05
850	~28	$(3.0 \pm 0.7) \times 10^{-5}$	2.7 ± 0.05
900	~13	$(4.8 \pm 0.5) \times 10^{-5}$	2.7 ± 0.05

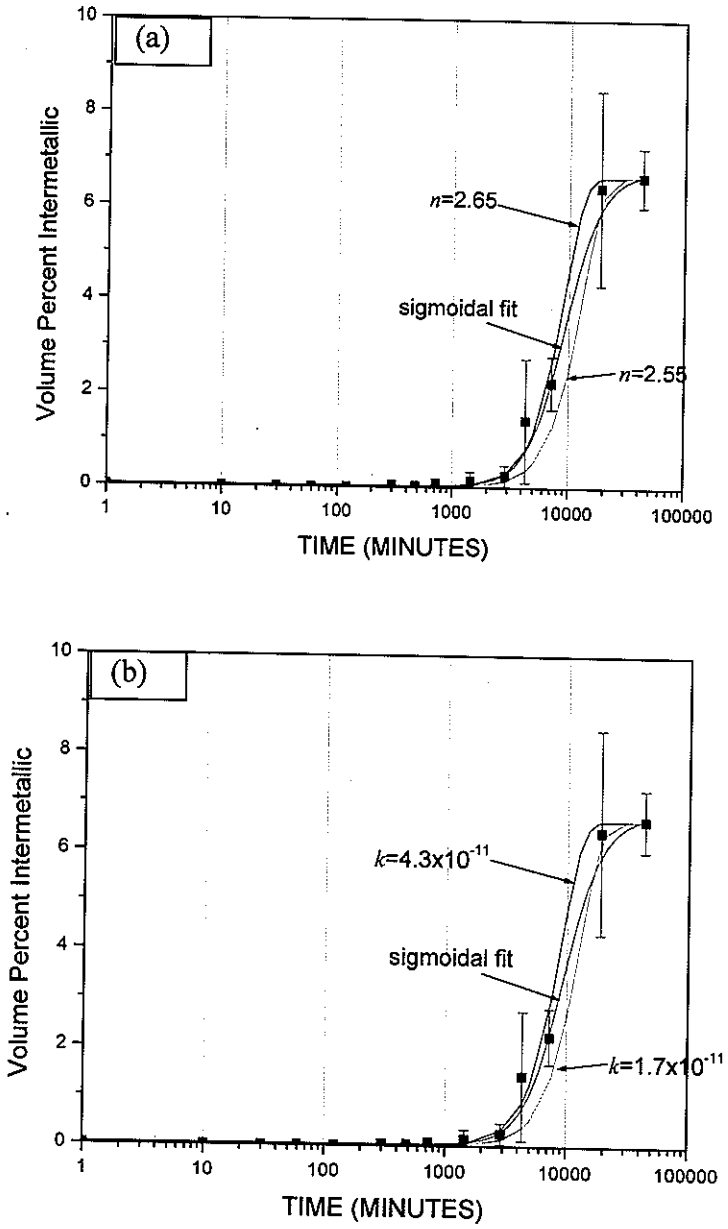

Fig. 40. Avrami plots for CD3MN at 700°C varied (a) n from 2.55 to 2.62 and (b) k from $2.3\text{x}10^{-11}$ to $5.3\text{x}10^{-11}$ min^{-n}.

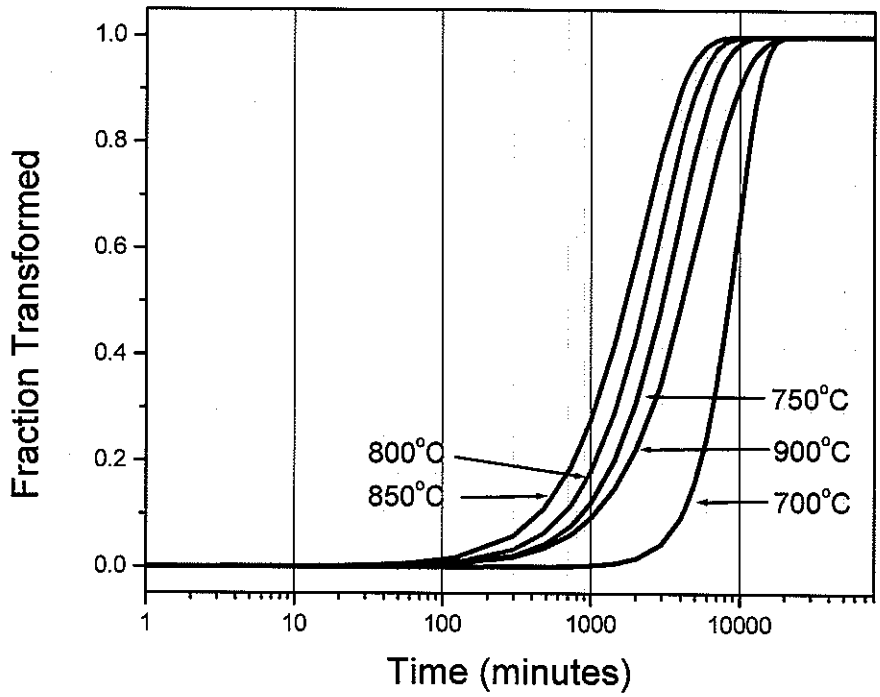

Fig. 41. Avrami curves determined for CD3MN.

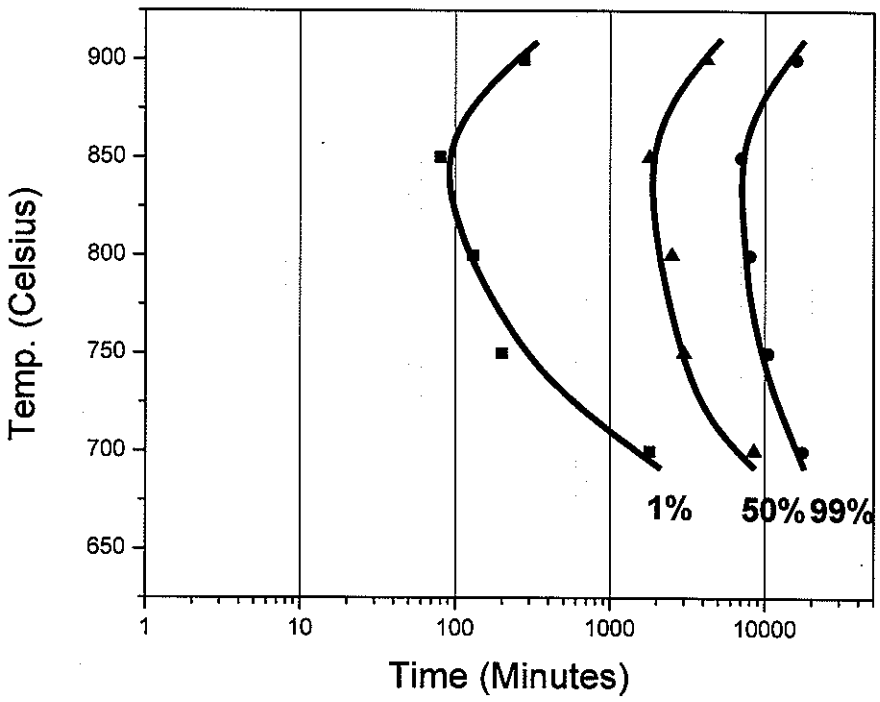

Fig. 42. Calculated TTT diagram of CD3MN.

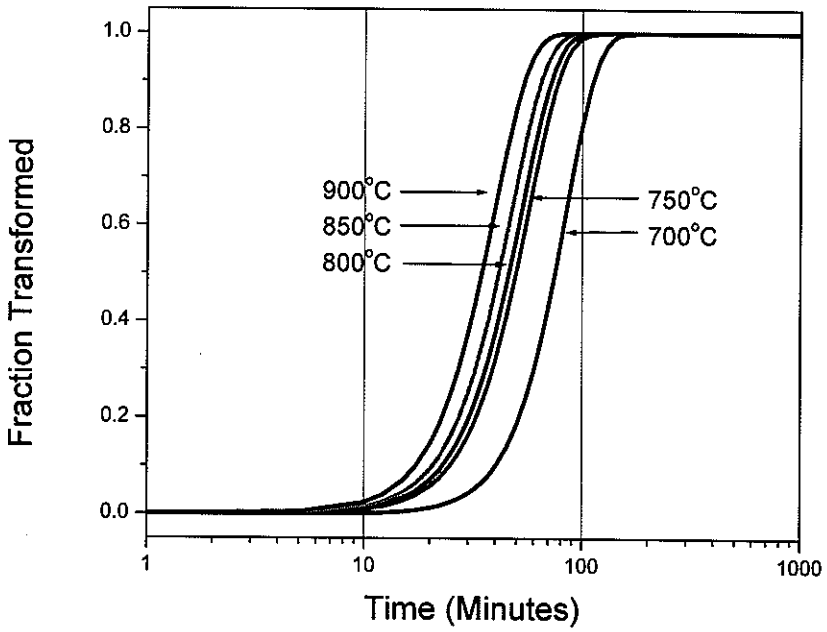

Fig. 43. Avrami curves determined for CD3MWCuN.

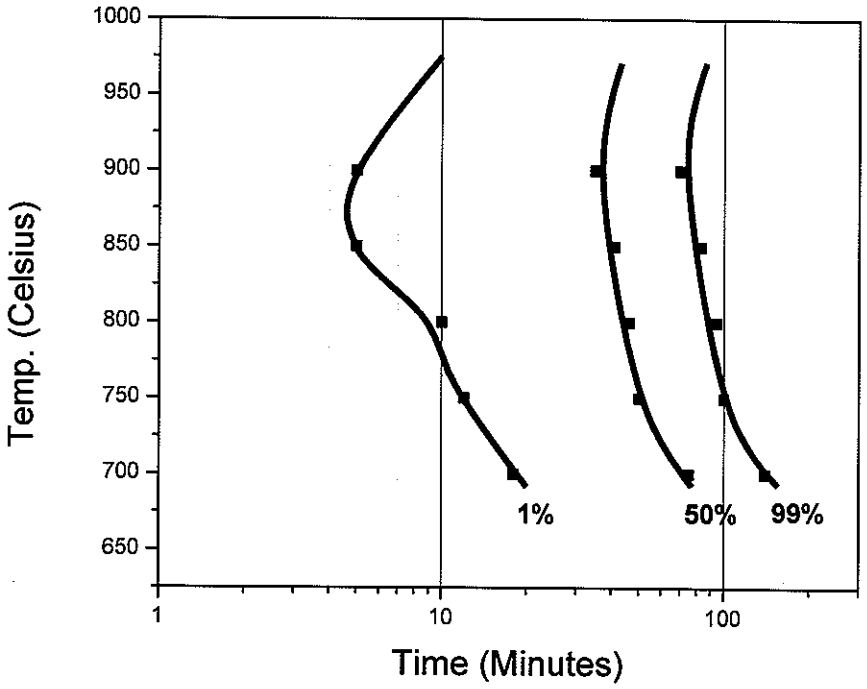

Fig. 44. Calculated TTT diagram of CD3MWCuN.

6.4. Discussion

The TTT curves established in this study show that intermetallic formation is much more rapid in CD3MWCuN than in CD3MN, with equilibrium amounts of intermetallic phase in the former also being much higher. This may be expected, since intermetallic phase formation is related to the concentration of Cr and Mo in the steel, both of which are present in greater amounts in CD3MWCuN. Therefore, higher concentrations of those elements would be expected to increase the driving force for intermetallic phase nucleation. This indeed is reflected in the calculated *n* values from the Avrami analysis for both CD3MN and CD3MWCuN, which imply different phase transformation behaviors, particularly nucleation rates.

The microstructures that developed in the two alloys upon formation of the intermetallic phase differed substantially from one another, being discrete precipitates in CD3MN and large regions of a eutectoid-like structure consisting of intermetallic and secondary austenite in CD3MWCuN. Associated with this morphology difference was the fact that the intermetallic formed at different rates and by different mechanisms in the two alloys, as indicated by the different exponent *n* values in the Avrami equation. The high *n* value (≈2.7-3) for CD3MWCuN indicates increasing nucleation and rapid growth. This would be consistent with a rapid structure formation as one expects to see in the closely-spaced $\sigma+\gamma_2$ assemblage that developed in this alloy. Similarly, the lower *n* value for CD3MN (≈1.4-2.6) is consistent with precipitation and slow growth, as would be expected for the relatively isolated intermetallic precipitates in this alloy.

The JMA analysis results relating the rate of intermetallic formation to resulting growth morphology can be confirmed by characterization discussed in Chapter 4. In CD3MN alloys, it was noted that intermetallic phase nucleated preferentially at the ferrite and austenite grain boundaries and grew into the adjacent ferrite grains, as shown in Fig. 24 (a) and (b). It is also seen from Fig. 24 (a) through (e) that the size of intermetallic phase increased with increasing soak time as did the number density, although to a lesser extent. The final size of intermetallic phase shown in Fig. 24 (e) or (f) appeared obviously coarser with irregular shape than that of the early stage of heat treatment. In CD3MWCuN alloys, as mentioned, intermetallic phase started to nucleate at the ferrite/austenite interfaces, as shown in Fig. 26 (a), but a $\sigma+\gamma_2$ dual-phase morphology (e.g., Fig. 35) was observed with increasing in soak time (Fig. 26 (b) - (e)). These observations agree with more detailed studies involving wrought alloy compositions, for which growth morphology and diffusion mechanisms were considered.[35,50,51]

TTT diagrams of several wrought DSS alloys have been published[1,28,35] and can be compared to the diagrams determined from this study. The alloy UR45N (alternatively designated by SAF 2205) has a chemical composition similar to CD3MN, while Zeron 100 is somewhat comparable to CD3MWCuN. A comparison of the TTT diagrams (Fig. 45) for the wrought versus the cast alloys shows that intermetallic phase formation starts at similar temperatures but at slightly delayed times in the cast alloys. As shown in Fig. 45 (a), for example, UR45N has the nose in the intermetallic phase curve at around 25 minutes and 850°C compared to 60 minutes and 850°C for CD3MN. Similarly, Zeron 100, shown in Fig. 45 (b), has the nose in the intermetallic curve at about 2.7 minutes and 850°C compared to about 4.5 minutes and 850°C for CD3MWCuN. These comparisons indicate that differences

in microstructure between cast and wrought alloys may play a role in affecting the kinetics of intermetallic phase formation. In terms of differences in microstructures, defects, for example dislocations and/or grain boundaries, formed in wrought alloys during fabrication may effectively promote σ and/or χ phases formation.

6.5. Conclusions

Kinetics of intermetallic phases (σ+χ) in two types of cast duplex stainless steels, CD3MN and CD3MWCuN, were studied employing the JMA equation. The kinetics and extent of intermetallic formation were much greater in CD3MWCuN. For both steels the intermetallic formation takes place in the approximate temperature range 700 - 1000°C, with the kinetics of sigma formation being fastest at about 850°C.

Comparison of TTT diagrams of cast DSS to wrought counterpart DSS indicates that the intermetallic phase transformation is slower in the cast alloys than in counterpart wrought alloys. This is believed to be due primarily to the difference in nominal compositions and microstructures between wrought and cast alloys.

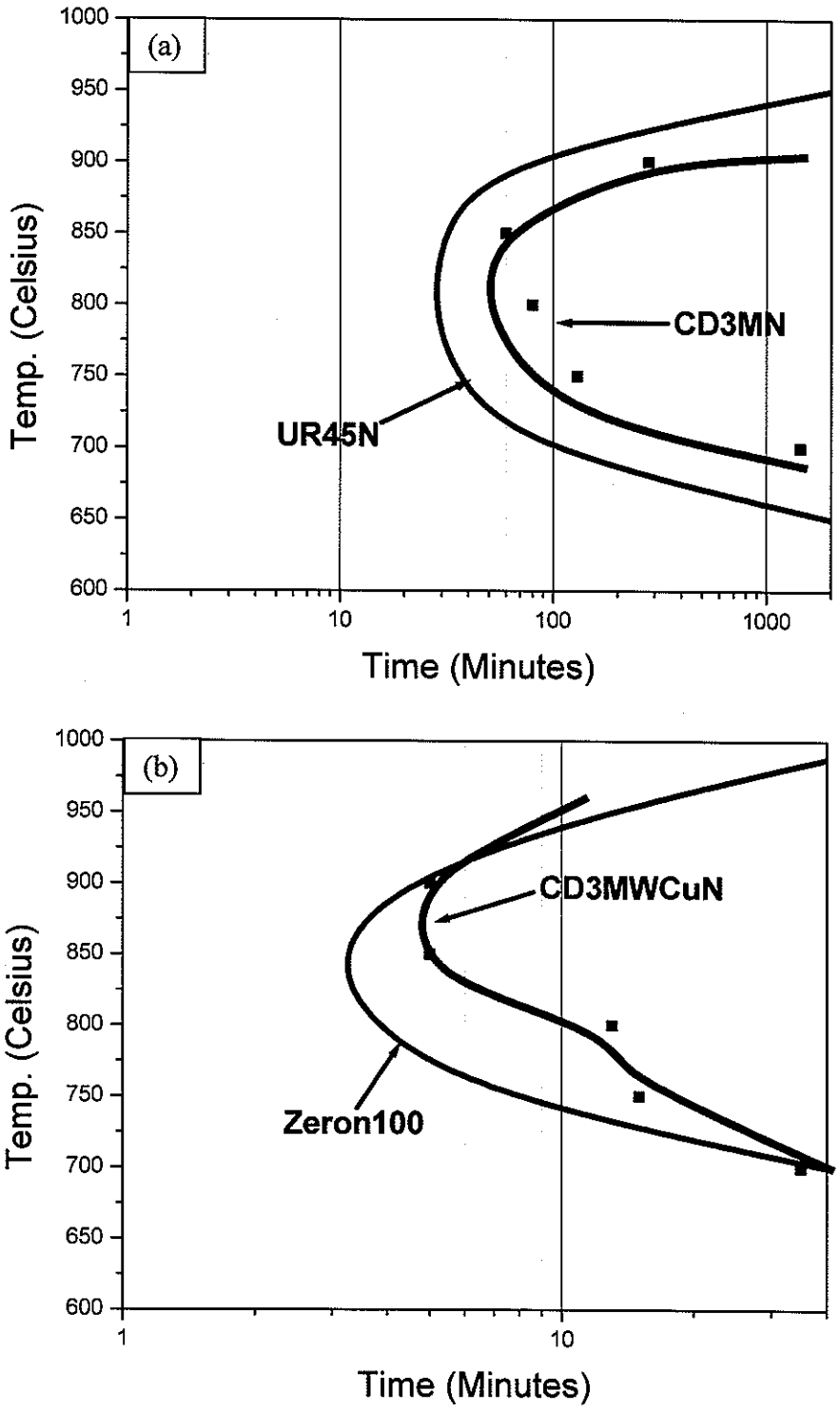

Fig. 45. Comparison to the TTT diagrams for (a) UR45N[3,5] and (b) Zeron 100[12] (wrought counterpart alloys for CD3MN and CD3MWCuN, respectively).

CHAPTER 7: CCT DIAGRAM DETERMINATION

7.1. Modified JMA Analysis for CCT Prediction

In order to investigate transformation kinetics during continuous cooling, it is mathematically convenient to assume that cooling paths can be constructed by summing a series of isothermal hold times. Specifically, the amount transformed for the entire non-isothermal reaction is assumed to adhere to the additivity rule, and this can be generally expressed as follows[11,65]:

$$\int_0^{t'} \frac{dt}{\tau} = \int_0^{T'} \frac{dT}{\tau\left(\frac{dT}{dt}\right)} = \int_0^{f'} \frac{df}{\tau\left(\frac{df}{dt}\right)} \qquad \text{Eq. 15}$$

where t' is the time (t) to reach a certain fraction transformed (f') during continuous cooling, and τ denotes the time taken for achieving the same fraction (f') when the transformation is isothermal at some effective temperature. A sufficient condition for the additivity of reactions is that the nucleation rate is proportional to the growth rate, a so called isokinetic condition. Such a condition is rarely satisfied in practice. Rather, it is found for many reactions that nucleation rate saturates at the early stage of transformation, which is often referred to as site-saturation. When this situation exists, the additivity rule may be invoked by setting Eq. 15 equal to unity.[13]

Based on the assumption of the additivity rule under the site-saturation condition, Wilson *et al.*[20] and Campbell *et al.*[67-71] modified the JMA equation for continuous cooling situations. Briefly, a cooling curve is assumed to be a series of step-wise paths as shown in Fig. 46. According to Eq. 15 with site-saturation, the total fraction transformed after such a

step-wise path is added to be unity. As illustrated in Fig. 46, at each cool-down temperature, the sample is held from τ_i for a fixed period Δt so long as the cooling rate is constant. In Eq. 15, τ can be considered as a transformation starting time after some cooling step i, at which the volume of precipitate formed is V_{i-1}. Transformation at T_i is completed in time $\tau_i+\Delta t$, and then moved to the next cooling step T_{i+1}. An expression for τ_i can be found from the JMA equation, *i.e.*,

$$\frac{V_{i-1}}{V_{ei}} = 1 - \exp(-k_i \tau_i^{n_i}) \qquad \text{Eq. 16}$$

giving

$$\tau_i = \left(\frac{\ln(1 - V_{i-1}/V_{ei})}{-k_i} \right)^{1/n_i} \qquad \text{Eq. 17}$$

Here, n_i and k_i are the parameters from the JMA equation at a particular temperature T_i, V_{ei} is the equilibrium volume of transformed phase at T_i, and V_{i-1} is the total volume transformed up to the time τ_i. By invoking the JMA equation it is tacitly assumed that during the holding period Δt, transformation follows typical isothermal transformation kinetics behavior. Therefore, transformation at T_i from τ_i for a period Δt contributes the total fraction transformed at the particular step. The modified JMA equation for continuous cooling transformation is thus given as shown in Eq. 12. At the temperature T_i, f_i or V_i can be calculated and plotted on a cooling curve. A CCT diagram can thus be predicted.

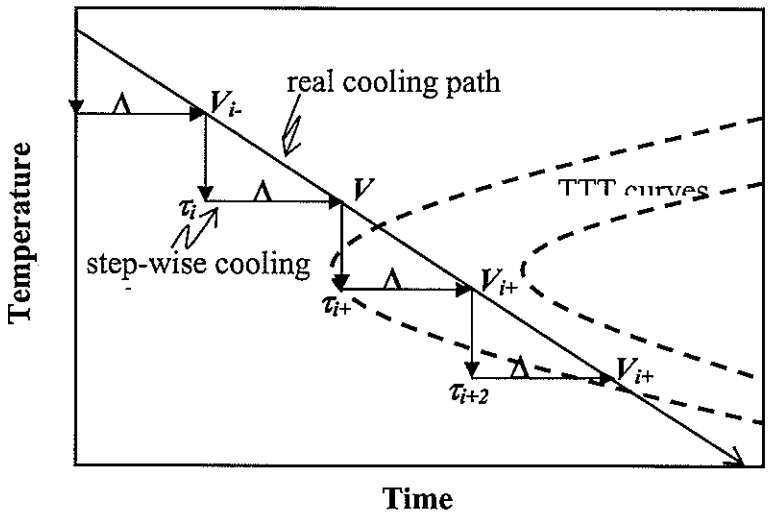

Fig. 46. Schematic description of a real cooling curve and a superimposed step-wise curve presented with TTT curves.

Parameters such as V_i, n_i and k_i at various temperatures for intermetallic phases were taken from the TTT study in Chapter 4. The intermetallic phase consists mainly of σ plus a small amount of χ. Tables 9 and 11 present the JMA parameters determined for the intermetallic phases in CD3MN and CD3MWCuN, respectively. Each temperature step is taken to be 50°C in a regular step-wise cooling path, as shown in Fig. 46. Thus, Δt in Eq. 12 was simply obtained by dividing the temperature step, *i.e.*, 50°C, by the cooling rate. Finally, a CCT diagram can be constructed by plotting volume V_i over a step-wise time duration, $t_{step} = (1100 - T_i)/cooling\ rate$, versus temperature.

The calculated initial (1 volume percent) and final (maximum volume percent) CCT curves for intermetallic phase formation in CD3MN and CD3MWCuN alloys are shown in Fig. 47 (a) and (b), respectively. It is recalled that intermetallic phase in this context

connotes σ+χ. The reliability of the predicted CCT diagrams will be confirmed by comparing with experimental results.

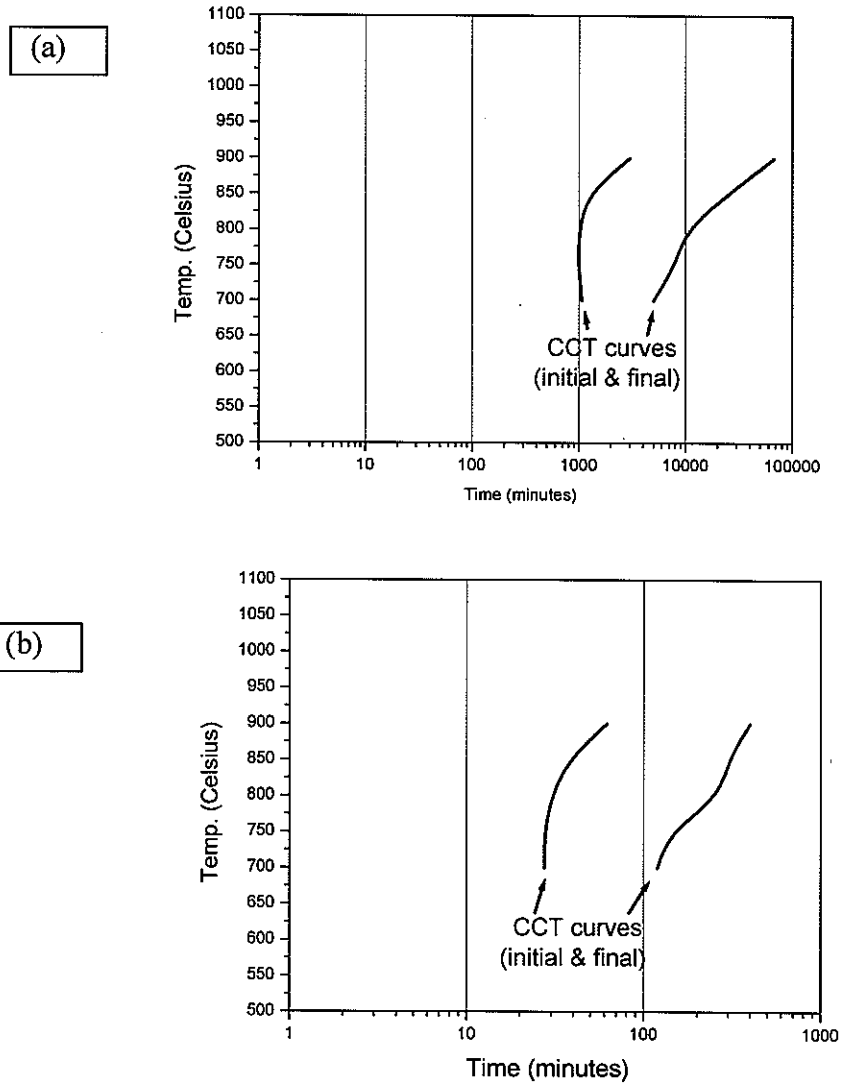

Fig. 47. Predicted initial (1 vol.%) and final CCT curves for the intermetallic phases in (a) CD3MN and (b) CD3MWCuN, respectively.

7.2. Microstructures of CD3MN and CD3MWCuN After Cooling

Optical micrographs of CD3MN after cooling at different rates from 1100°C to room temperature are shown in Fig. 48. As indicated, the microstructures were found to consist of ferrite, austenite and intermetallic and carbide precipitates. The phase identification of each phase was based on tint-etched color and EDS analyses. The electrolyte etching technique used colors the delta-ferrite orange to a light blue and the sigma and chi phases gold-brown, but it does not color the austenite. Accordingly, the globular shaped phase in the micrograph in Fig. 48 is inferred to be austenite within a δ–ferrite matrix. As shown in Fig. 48 (c), intermetallic precipitates (σ+small χ) in CD3MN form primarily at the δ/γ interphase boundaries during the initial stages of transformation. These precipitates grow by consuming the δ matrix, in agreement with previous studies.[1,36,56] The resulting amount and size of intermetallic precipitates increased substantially at slower cooling rates. The area (or volume) percents of intermetallic precipitate in CD3MN were measured and the results are summarized in Fig. 49. A measurable amount of phase (0.54%) was observed in the sample cooled at 0.5°C/*min*, but not at the relatively fast cooling rates of 2 and 5°C/*min*.

Microstructures of CD3MWCuN are shown in Fig. 50. Dual phase assemblages of $(\sigma + \chi) + \gamma_2$ were observed in the δ matrix. Such morphology is also seen optically in the TTT study samples and has been seen in previous studies on the wrought counterpart alloy, Zeron 100.[35] Fine intermetallic precipitates start to form at δ/γ interphase boundaries. This initial precipitation develops into a rapidly growing dual-phase morphology of intermetallic (predominantly σ) with γ_2 in the ferrite matrix. Such a formation behavior is associated with

much faster phase formation kinetics, as seen for the TTT samples. For instance, intermetallic phase formation was observed even at the relatively fast cooling rate, 5°C/*min*, at which approximately 3.61% was formed. A similar amount of intermetallic phase (about 10%) was observed at slow cooling rates of 0.1°C/min to 1°C/min. The area (or volume) percent of intermetallic phase was found to be higher for these given cooling rates than was seen in CD3MN. Intermetallic phase percents in CD3MWCuN alloy after continuous cooling are shown in Fig. 51.

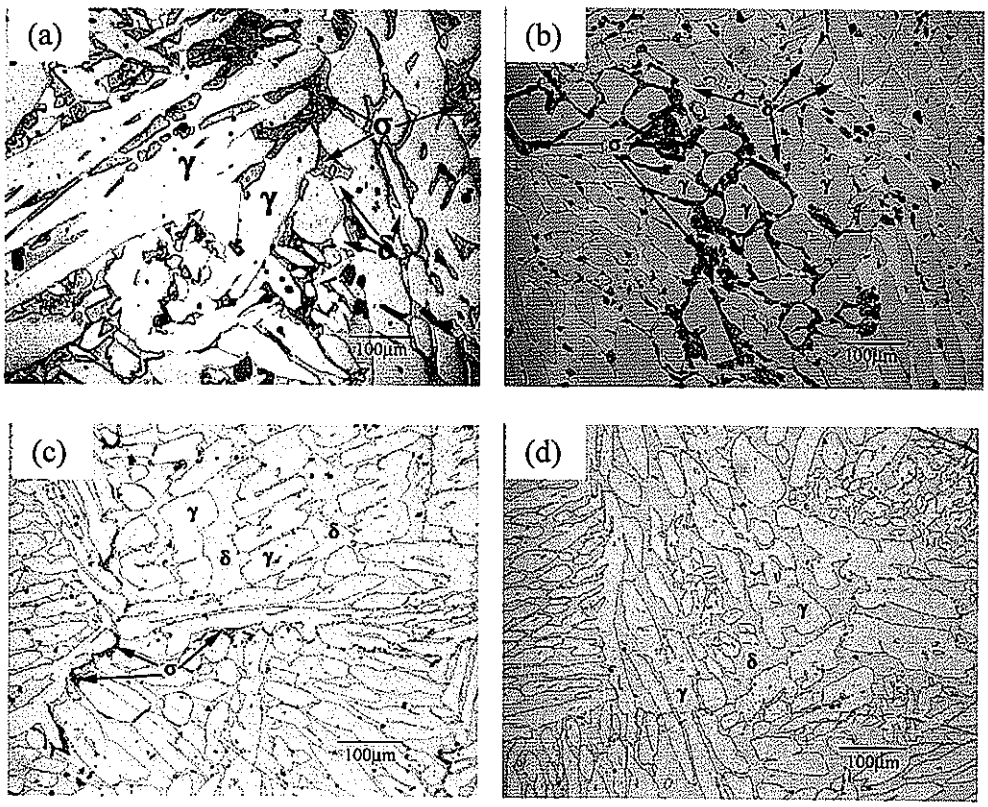

Fig. 48. Optical micrographs of CD3MN after continuous cooled at the rates of (a) 0.01, (b) 0.1, (c) 0.5, and (d) 1 °C/*min*.

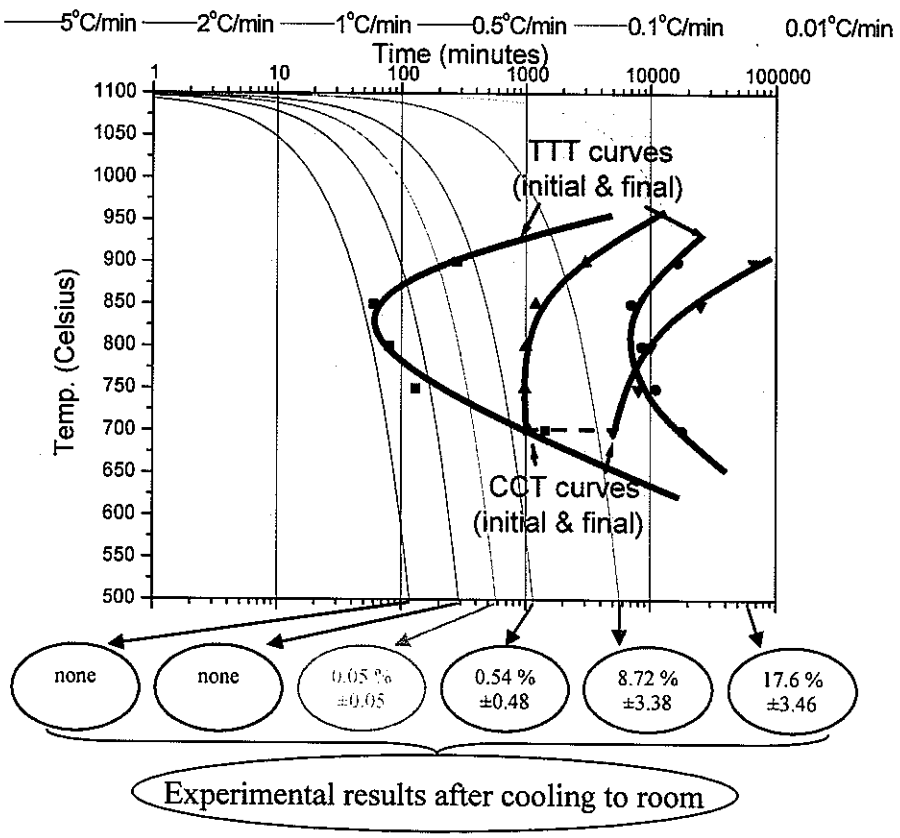

Fig. 49. Calculated CCT curves of CD3MN showing initial and final intermetallic phase precipitation superimposed on the corresponding TTT curves. Experimental results for cooling from 1100°C to room temperature are indicated in circles. Cooling rates are 5, 2, 1, 0.5, 0.1, and 0.01°C/*min*, shown respectively from left to right in the diagram.

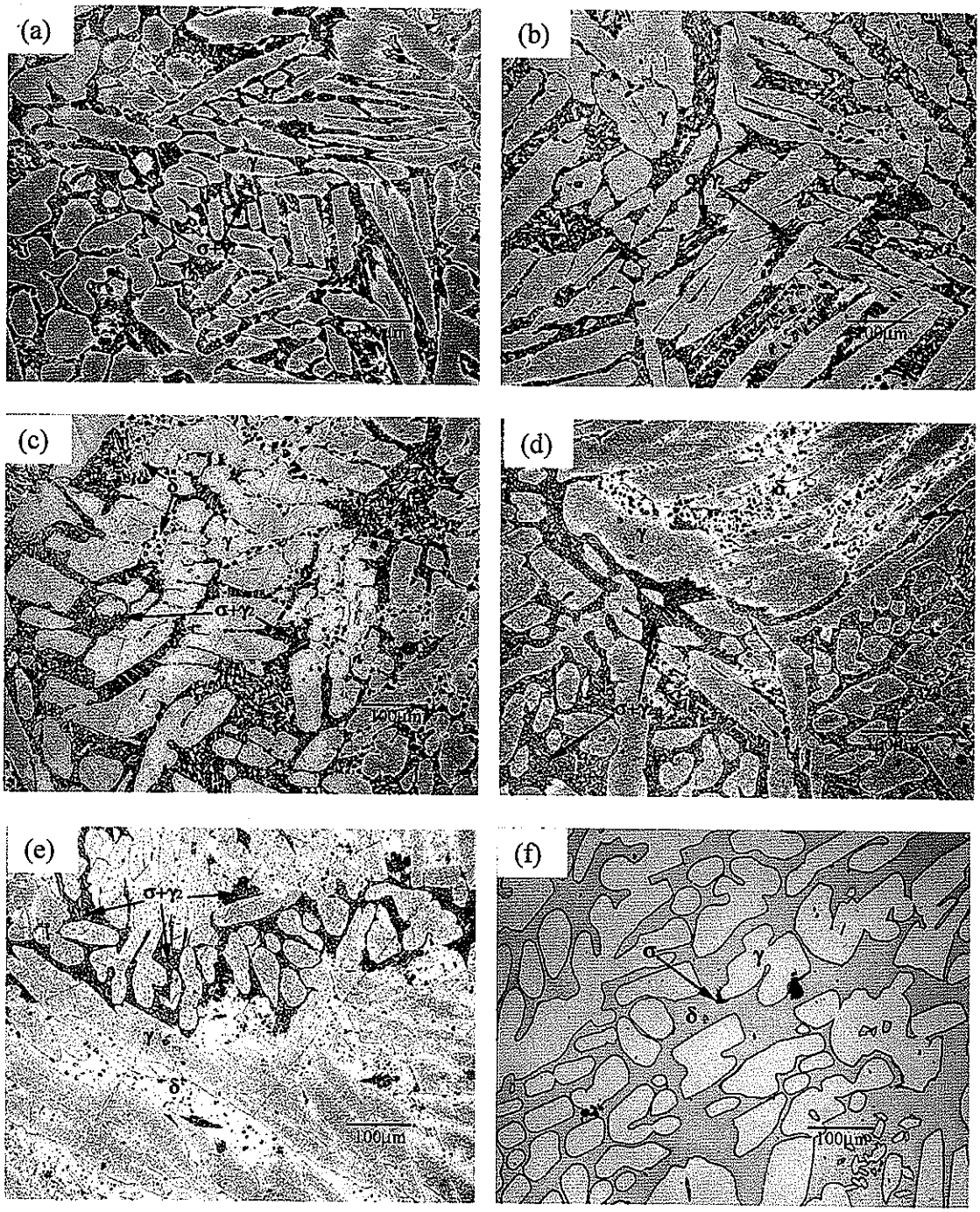

Fig. 50. Optical micrographs of CD3MWCuN after continuous cooled at the rates of (a) 0.1, (b) 0.5, (c) 1, (d) 2, (e) 5 °C/*min* and rapidly cooled using the Bridgman furnace with a velocity of 0.100 *mm*/sec.

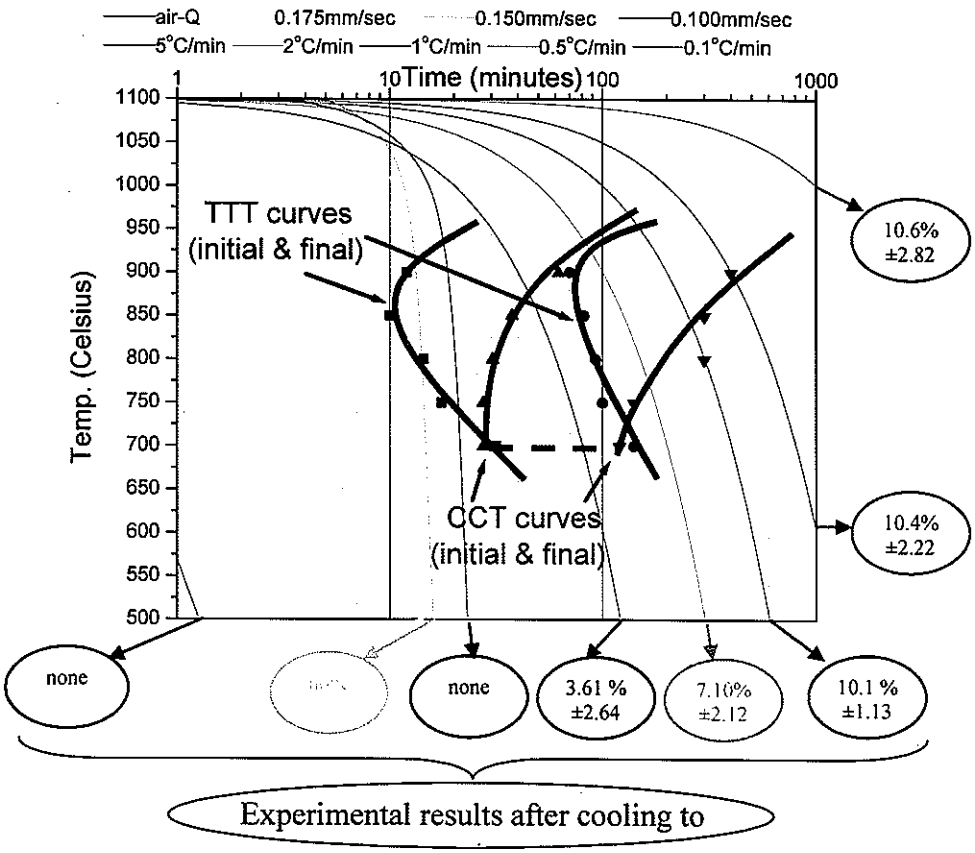

Fig. 51. Calculated CCT curves of CD3MWCuN showing initial and final intermetallic phase precipitation superimposed on the corresponding TTT curves. Experimental results for cooling from 1100°C to room temperature are indicated in circles. Cooling curves are air quenching, 0.175, 0.150, 0.100 *mm/sec* using the Bridgman furnace, and 5, 2, 1, 0.5, 0.1 °C/*min* using a tube furnace are shown respectively from left to right in the diagram.

7.3. Hardness Testing

The results of the Rockwell hardness tests conducted on the continuous cooled CD3MN and CD3MWCuN alloys are shown in Figs. 52 and 53, respectively. Since the amount of intermetallic phase formation was found to be smaller in CD3MN than CD3MWCuN during isothermal transformation discussed previous section, the hardness was anticipated to be lower in the former. Hence, the Rockwell B scale was used for CD3MN and the C scale for CD3MWCuN. The hardness of CD3MN shows a plateau at approximately 94 on the Rockwell B scale when cooled at the faster rates of 0.5 to 5°C/min. However, the hardness increased slightly at slower cooling rates such as 0.1 and 0.01°C/min, reaching approximately 99 Rockwell B. CD3MWCuN, on the other hand, showed increasing hardness from the fastest cooling rate, 5°C/min to the slowest 0.1°C/min. Hardness ranges for this alloy were obtained between 22 and 30 Rockwell C .

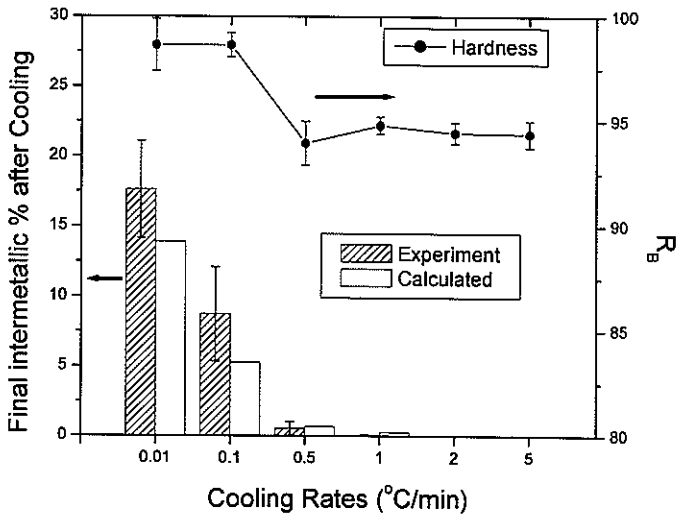

Fig. 52. Final intermetallic phase percent after cooling at various rates and corresponding Rockwell B scale hardness measured for CD3MN.

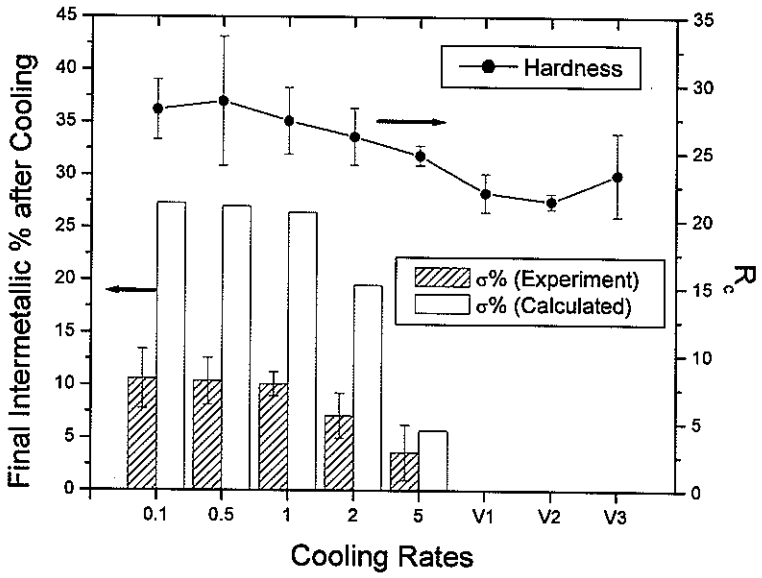

Fig. 53. Final intermetallic phase percent after cooling at various rates and corresponding Rockwell C scale hardness measured for CD3MWCuN.

7.4. Discussion

The calculated initial (1 vol.%) and final (maximum vol.%) CCT curves and previously determined TTT curves of CD3MN and CD3MWCuN are compared in Figs. 49 and 51, respectively. The nose of the initial CCT curve for CD3MN is located between 750°C and 800°C at approximately 1000 minutes. This location is delayed in time by roughly an order of magnitude and decreased by about 100°C from the initial TTT curve. Similarly, the nose of the initial CCT curve for CD3MWCuN is shifted to lower temperatures and a longer time, calculated to be between 700°C and 750°C in about 28 minutes. This

shifting of the extent of transformation to lower temperatures and longer times is a common observation.[12] This is because unlike an isothermal transformation, during continuous cooling the driving force for the start of transformation increases in a continual and sometimes gradual manner. Thus, while the driving force for nucleation continually increases as a result of cooling, the overall force remains small near the TTT curve; therefore, the nose of the CCT curve is usually shifted to lower temperature and longer times.

The experimentally measured volume percentages of intermetallic phase at each cooling rate are in reasonable agreement with the calculated CCT diagrams. The experimental results are indicated in circles in Figs. 49 and 51. As seen in the JMA analysis, the phase transformation kinetics in CD3MN are very sluggish, and no intermetallic phase was observed at the relatively fast cooling rates of 2 and 5°C/*min*. The first observed intermetallic phase was measured to be 0.54% at 0.5°C/min, slightly left of the nose of the initial calculated CCT curve, which corresponds to 1% precipitate.

Reasonable agreement is also seen for the CD3MWCuN alloy in which intermetallic formation is much more rapid, due to higher Cr and Mo concentrations and different transformation mechanisms (dual-phase morphology). The nose of the curve is predicted to lay somewhere between 5°C/*min*, the fastest velocity obtained with the conventional tube furnace, and 0.100*mm/sec*, the slowest velocity studied with the Bridgman furnace. (N.B. Cooling profiles from a Bridgman furnace are not constant due to an increasing thermal gradient as the relative distance to sample increases. Temperature profiles for the three velocities shown in Fig. 51 are plots of the thermocouple data obtained during cooling, the average rate over 20 minutes for 0.100*mm/sec* being approximately 30°C/min.) Concerning the location of the initial CCT curve, a constant rate of between 15 and 20°C/min. is

estimated as being required to intersect the nose of the curve. As shown in Fig. 51, the calculated initial curve is located within the region defined by the 5°C/*min* and 0.100*mm/sec* curves.

Figures 52 and 53 compare experimental and calculated final amount of intermetallic phase after cooling in CD3MN and CD3MWCuN, respectively. Calculation for the kinetically slower transforming CD3MN system (Fig. 52) predicts a maximum final volume percentage of 13.9%. Approximately 17.5% was observed experimentally, which is within experimental error and is nearly what was seen in earlier TTT studies in Chapter 4. Such error may be caused by other factors affecting precipitation, such as the amount of grain and interphase boundaries available as nucleation sites.[69] Since the intermetallic phases nucleated along the interphase boundaries between δ and γ, the interphase boundary area could also affect transformation kinetics during cooling. However, the δ/γ interphase boundary area was similar for the two alloys studied (cf. Figs. 48 and 50) suggesting that other factors, such as minor element contents in the alloys, plays a role in affecting the transformation kinetics.

The kinetically faster transforming CD3MWCuN system (Fig. 53) shows poor agreement between calculated and experimentally determined values. It is interesting that all of the slower cooling rates were predicted to have reached an equilibrium value (Fig. 51) of approximately 10% intermetallic, however, this value is much less than the calculated maximum equilibrium value of 27% and less than the final value seen for the more sluggish CD3MN. This is presumably due to an overriding influence of kinetic factors and dual-phase morphology of $(\sigma + \chi)+\gamma_2$. Another reason can be found from the manner by which the intermetallic transforms. Unlike CD3MN alloys, fine intermetallic precipitates continually

nucleate in the ferrite matrix. Therefore, nucleation plays a role in the formation of intermetallic phase throughout the entire transformation period. This does not obey the assumption of site-saturation for the additivity rule.

The measured hardness of the two alloys as a function of cooling rate is also shown in Figs. 52 and 53. In general, hardness appears to follow the amount of intermetallic phase and significantly increases once the amount of intermetallic phase reaches around 5%, as reported in other studies.[1,29]. Such results are reasonable since σ and χ are hard and can be expected to embrittle the alloy.

Intermetallic precipitation behavior during continuous cooling has been studied in SAF 2205 DSS, the wrought counterpart alloy of CD3MN. Chen *et al.*[24] reported that initial phase formation (1 volume percent σ-phase) was observed at a cooling rate of 0.25°C/*sec* (equivalent to 15°C/*min*) in the wrought DSS. This indicates a much faster rate of intermetallic phase formation than is observed in the cast material of this study, where initial intermetallic formation is only seen at cooling rates slightly less than 0.5°C/*min*. The comparison between CCT diagrams for CD3MWCuN and its wrought counterpart alloy, Zeron 100, could not be made since a CCT diagram of the wrought counterpart alloy has not been published. However, the results for CD3MN support the earlier TTT study in which it was found that transformation kinetics are more sluggish in cast alloys than in wrought counterpart alloys.

7.5. Conclusions

CCT diagrams of cast duplex stainless steels CD3MN and CD3MWCuN have been determined mathematically and experimentally. Samples were solution heat treated at 1100°C for 30 minutes and cooled to room temperature at various rates. Area (or volume) percent of intermetallic phase through optical microscopy was measured for each sample by image analysis system. And the experimental data were compared to calculated CCT diagrams. Observations in CD3MN agree reasonably with the theoretical calculations, but showed poor agreement in CD3MWCuN. The rapid transformation rate and dual phase morphology of intermetallic phase in CD3MWCuN indicates kinetic factors dominate in this system, causing deviation from the model.

Results from hardness test for both alloys were found to be correlated to the amount of intermetallic phase. If intermetallic phase reaches 5 vol. %, hardness was shown to increases substantially.

Kinetics of intermetallic phase formation in cast DSS during continuous cooling was found to be slower than the wrought counterpart alloy as previously reported on the isothermal transformation kinetics of both alloys. This is speculated that the difference in composition and microstructure plays a role in intermetallic phase precipitates.

CHAPTER 8. *THERMO-CALC* STUDY/DESIGNED EXPERIMENTS

The equilibrium fraction of intermetallic phase formation can be empirically obtained from the Avrami equation for the alloys examined. As an alternative, a thermodynamic software package such as *Thermo-Calc* may be used to overcome the practical limitations of experimentally determining the equilibrium fraction of phases in a specified alloy composition. Databases used by *Thermo-Calc* have been produced by various thermodynamic research groups and institutes.[38,73] Importantly, the equilibrium calculations are sensitive to the database used. Among the databases, the most recent iron and steel database TCFE 3[73] (Thermo-Calc steels/alloys database version 3.0 released in 2002) produced by Thermo-Calc Software AB, Stockholm, Sweden was used for this research.

Based on TEM/SEM characterization, seven possible phases, δ, γ, σ, χ, Cr_2N, $M_{23}C_6$, liquid, were considered for the phase equilibria calculations. Figure 54 shows the predicted equilibrium mole fraction of phases versus temperature in the CD3MN and CD3MWCuN alloys of nominal composition predicted. The amount of σ phase formed is at least a factor of two greater than the amount of χ in terms of mole fraction. It was possible to calculate the equilibrium volume percent of σ using *Thermo-Calc*; however, the same could not be done for χ because the molar volume of this phase is not present in the database used.[52] Therefore, the volume of χ at 800°C was estimated using the *Thermo-Calc* results for total molar volume, and calculating the molar volume of χ phase using the crystal structure data in Table 12. The results, presented in Table 16, show the volume fraction of σ is always significantly greater than that of χ, as suggested in Fig. 54. Note also that the calculated

values shown in Table 16 are significantly higher than the 1-2 vol% maximum seen experimentally (see, for example, Fig. 30).

(a)

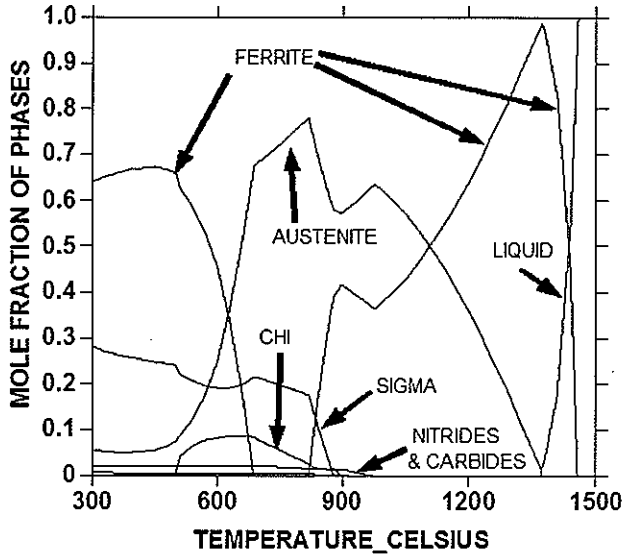

(b)

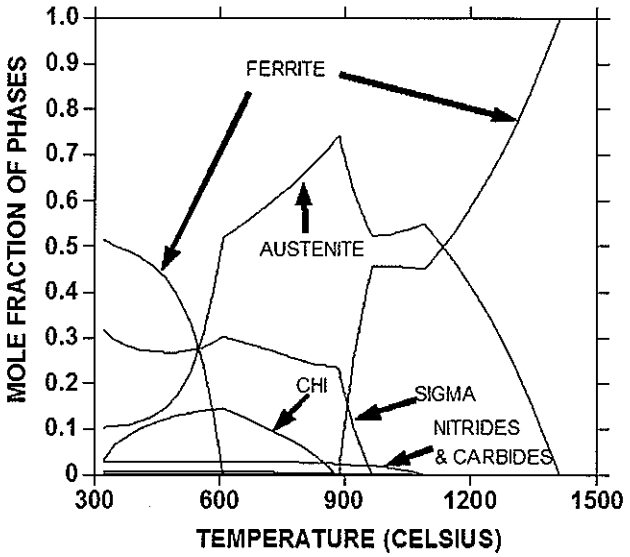

Fig. 54. *Thermo-Calc* calculation plotted for (a) $4A_1$ (CD3MN) and (b) $6A_1$ (CD3MWCuN) compositions in Table 4 in mole fraction of phases vs. temperature.

Table 16. Summary of experimental and calculated intermetallic phase volume percents at 800°C using $4A_1$ and $6A_1$ compositions of CD3MN and CD3MWCuN, respectively. Maximum intermetallic phase formation temperature is also shown.

	CD3MN		CD3MWCuN	
	Max. temp., °C	vol.% at 800°C	Max. temp.,°C	vol.% at 800°C
OM Results				
σ including χ	~950	11.75 ± 2.68	~1050	28.48 ± 2.88
SEM Results				
σ phase	~950	14.45 ± 2.87	~1050	16.54 ± 1.75
χ phase	~900	1.19 ± 0.40	~900	1.46 ± 0.59
Predicted by *Thermo-Calc*				
σ phase	~880	~9.80	~970	~18.0
χ phase	~900	N/A	~890	N/A
Calculated from Table I using $V_m^{\chi} = 7.37 \times 10^{-6}$ m^3/mole				
- χ phase	N/A	6.18	N/A	9.00

It is also seen from Fig. 54 that the maximum temperature for the formation of σ is predicted to be about 880°C and 970°C for CD3MN and CD3MWCuN, respectively. Experimentally the maximum temperatures for σ formation were found to be slightly above 900°C for CD3MN (Fig. 43) and around 1000°C for CD3MWCuN (Fig. 44). This

discrepancy is not attributed to the formation of χ phase (rather than σ) because Fig. 54 shows that χ phase is predicted to form at lower temperature than σ phase.

The driving force for the formation of σ and χ phases can be computed as a function of temperature and this is shown in Fig. 55. Assuming the composition for CD3MN and a pre-heat treatment at 1100°C followed by quenching to lower temperatures between 700°C and 900°C, the driving forces for nucleation of σ and χ are essentially the same. This suggests that local composition fluctuations could easily affect which phase actually forms initially in any given location.

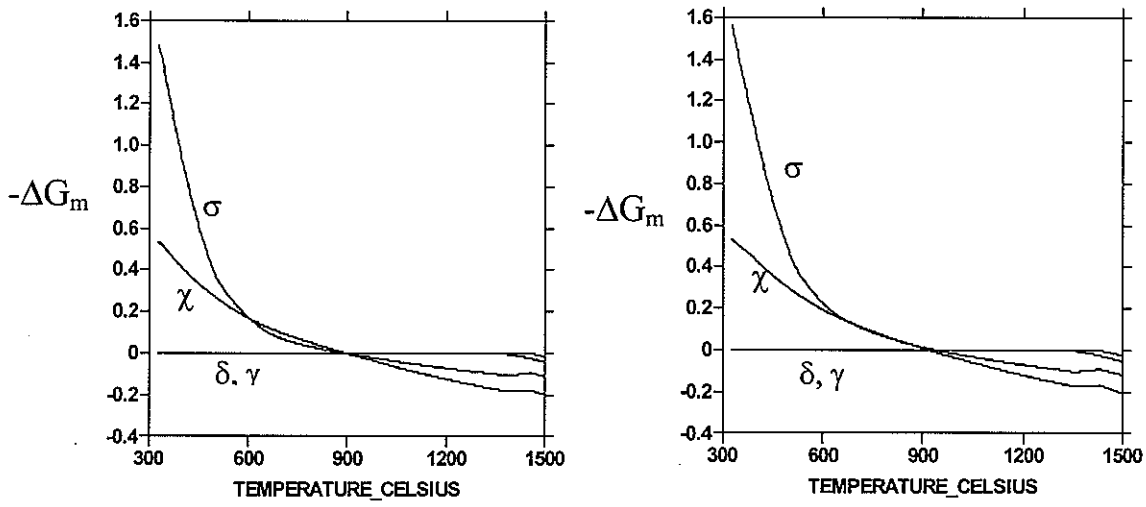

Fig. 55. Driving force of δ, γ, σ and χ phases after pre-heat treatment at 1100°C in (a) CD3MN and (b) CD3MWCuN.

In order to examine the sensitivity of alloying additions on σ and χ formation a designed experiment was undertaken in which the amounts of Cr, Ni, and Mo were systematically varied to produce a three-factor full-factorial design based upon the composition of CD3MN. Target compositions are shown in Table 6 while Table 7 gives the actual measured compositions. Etched optical micrographs of each heat are shown in Fig. 56. All alloys possess the typical DSS microstructure consisting of globular primary austenite in a ferrite matrix; however, the amount and size are different depending upon Cr, Ni and Mo contents.

Figure 57 shows the *Thermo-Calc* predicted mole fraction of phases versus temperature plots for σ and χ using the measured compositions in Table 7. Comparing Heat #7 and #5 it is seen that Cr addition is expected to push σ formation to much higher temperatures (<700 to 875°C) and to greatly increase the equilibrium amount (7.5 mole % to 30 mole %); while for χ the formation temperature decreases and equilibrium amount slightly decreases (>900 to ≈825°C, near 10 mole % to ≈ 6 mole%). Raising Ni content (comparing heat #3 to #4) also pushes σ content and formation temperature up slightly while slightly lowering χ temperature and amounts. Increasing Mo (Heat #7 vs #1) slightly increases χ formation temperature and greatly increases equilibrium amount (< 10 mole % to >15 mole %), while depressing σ formation temperature and amount. Thus, *Thermo-Calc* predicts that high Mo favors χ formation while high Cr (and Ni to a mush lesser extent) favors σ.

The experimental results obtained by direct observation of the alloys having varying major alloying elements are shown in Table 17, which records the observed maximum

temperature for intermetallic phase formation as well as the predicted results from *Thermo-Calc*. Phase identification of the σ and χ phases in Table 17 was carried out using a combination of SEM imaging and EDS analysis. This was done as follows. When both phases were present, backscattered electron (BSE) images could be used to differentiate between the phases as shown in Fig. 58. Both *Thermo-Calc* predictions and TEM examination of CD3MN and CD3MWCuN show σ to be the major phase with χ being the minor phase. Therefore, the χ phase is identified as the brighter phase and σ is the somewhat darker phase in Fig. 58. EDS data collected on intermetallic phases with different contrast confirmed that the brighter appearance of χ is due to it having a higher Mo and lower Cr content as compared to the somewhat darker σ. This agrees with the trends predicted in Fig. 57 where higher Mo favors χ formation while higher Cr favors σ. From this basis, phase identification was carried out at the earliest stages of precipitation, where only one phase may have been present, by comparing the measured composition of the precipitate to the average predicted compositions of σ and χ. The actual compositions measured are shown in Table 18. Generally, if the phase was seen to be Cr-rich (≈30 wt.%) and Mo-poor (≈ 10 wt.% or less), it was considered to be σ. Similarly, if the precipitate was Mo-rich (≈14wt.%) and Cr-poor (<25%) it is believed to be χ.

Comparing the experimental results to the *Thermo-Calc* results summarized in Table 17 reveal both good and poor matches between predicted and observed maximum formation temperature of intermetallic phases. For example, Heats #1, #2 and #7 closely matched with experiments. The two major discrepancies in the remaining heats are that the formation temperatures are always predicted to be lower than what is actually observed, sometimes by

as much as 75 degrees, and the predicted initial phase to form is incorrect. For example, *Thermo-Calc* often predicts χ to be more stable at high temperature, while σ was observed experimentally (e.g. Heats 2, 3, 4, and 7).

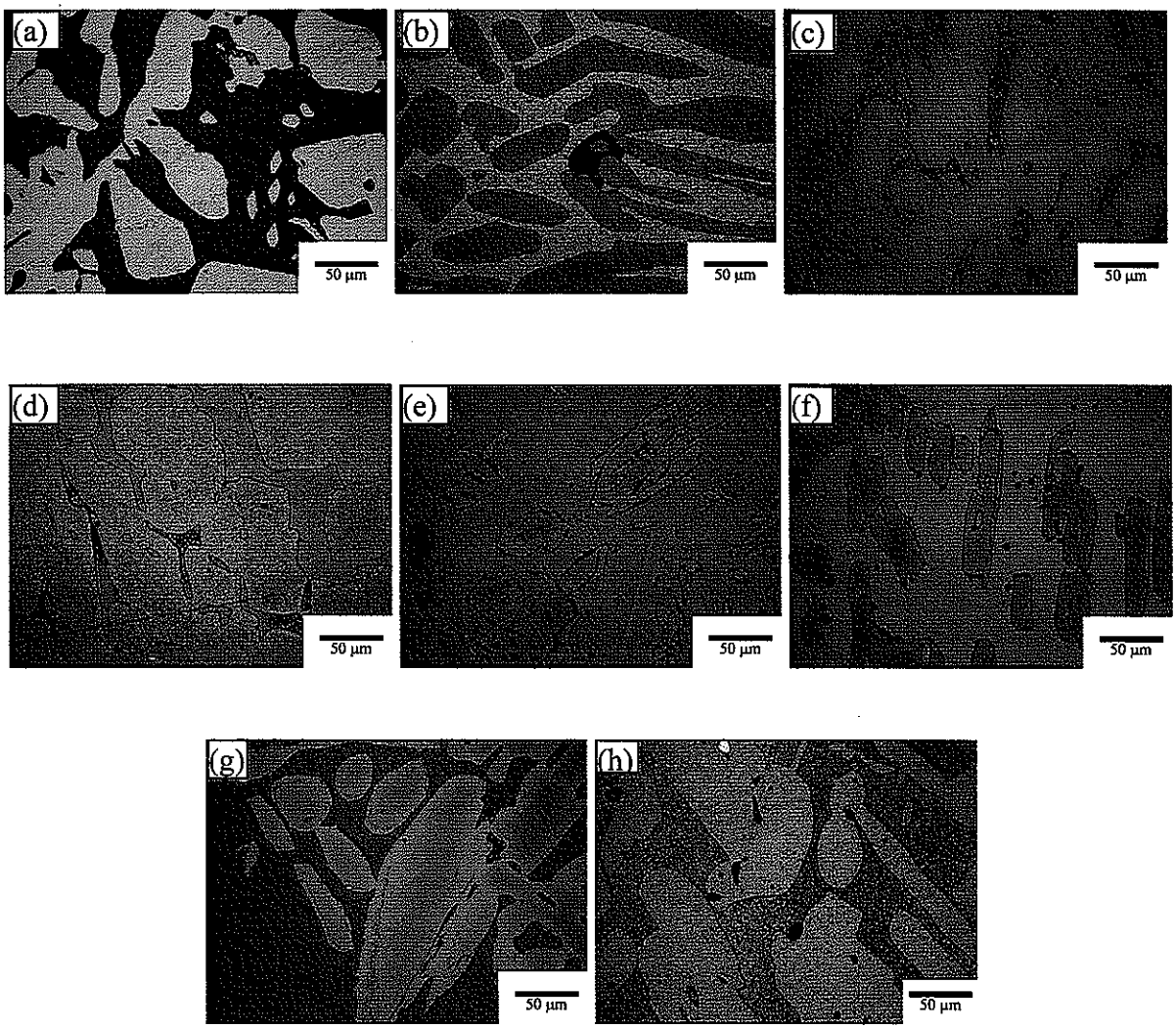

Fig. 56. Micrographs of heat treated alloys: (a) Heat 1 at 925°C, (b) Heat 2 at 975°C, (c) Heat 3 at 975°C, (d) Heat 4 at 975°C, (e) Heat 5 at 950°C, (f) Heat 6 at 950°C, (g) Heat 7 at 900°C and (h) Heat 8 at 1025°C.

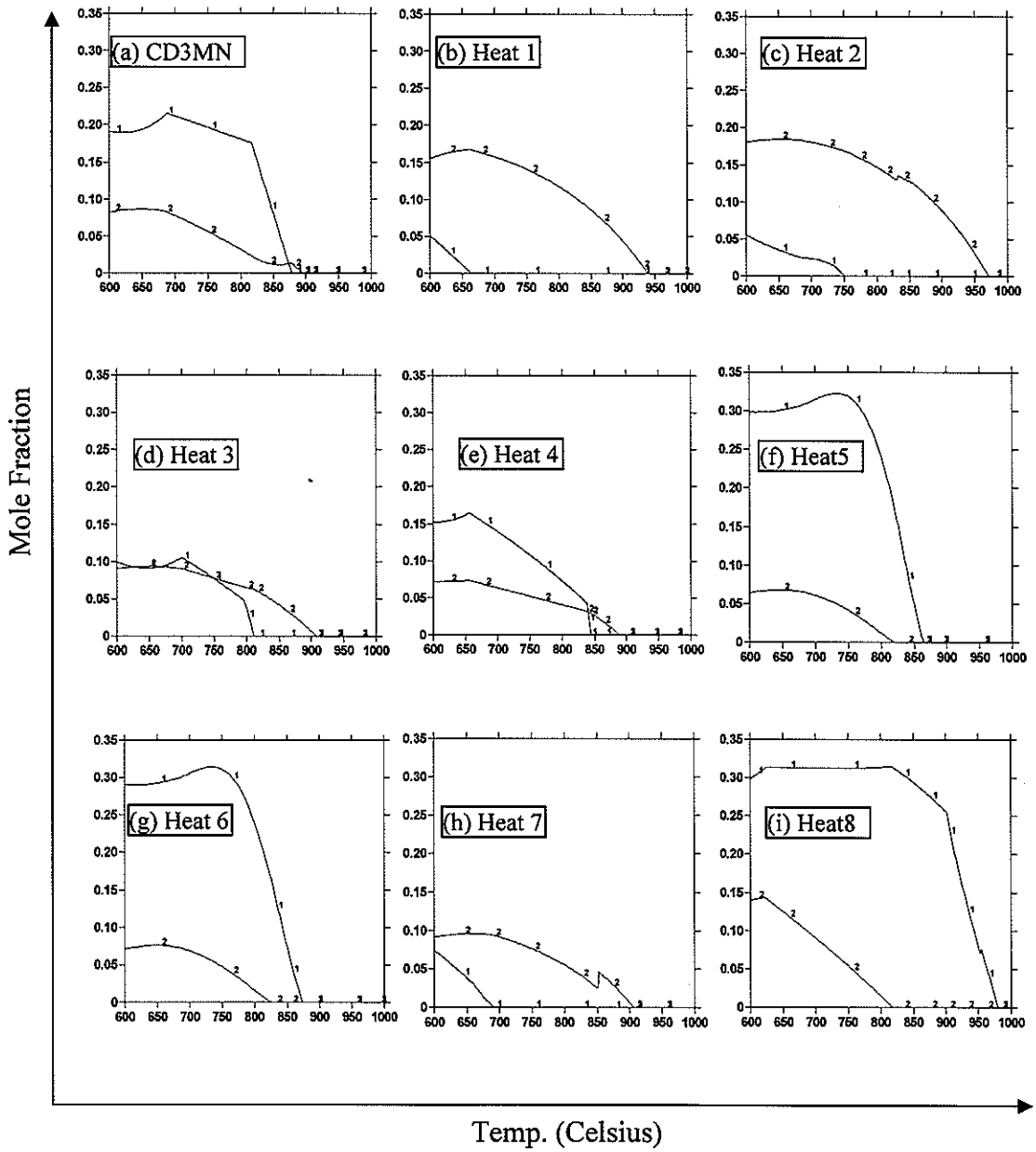

Fig. 57. *Thermo-Calc* results for various cast steels plotted mole fraction of phases vs. temperature where curve 1 is σ and curve 2 is χ.

Table 17. Identified intermetallic phase at maximum formation temperature with *Thermo-Calc* prediction.

	Major Contents (wt.%)			Max. Temp.(°C) and Corresponding Phase			
Alloys	Cr	Ni	Mo	*Thermo-Calc*		Experiments	
CD3MN	22.1	5.4	2.9	895	χ	950	σ
Heat 1	19.1	3.9	3.8	940	χ	925	χ
Heat 2	18.8	4.7	4.4	970	χ	975	σ + χ
Heat 3	19.5	5.7	2.9	907	χ	975	σ
Heat 4	19.4	6.9	2.8	888	χ	975	σ
Heat 5	24.9	4	2.9	865	σ	950	σ
Heat 6	24.8	4	3	874	σ	950	σ
Heat 7	19.2	4	2.9	905	χ	900	σ + χ
Heat 8*	25	6.9	3.9	980	σ	1025	σ

* Composition of Heat 8 is within the nominal limit of CD3MWCuN alloy.

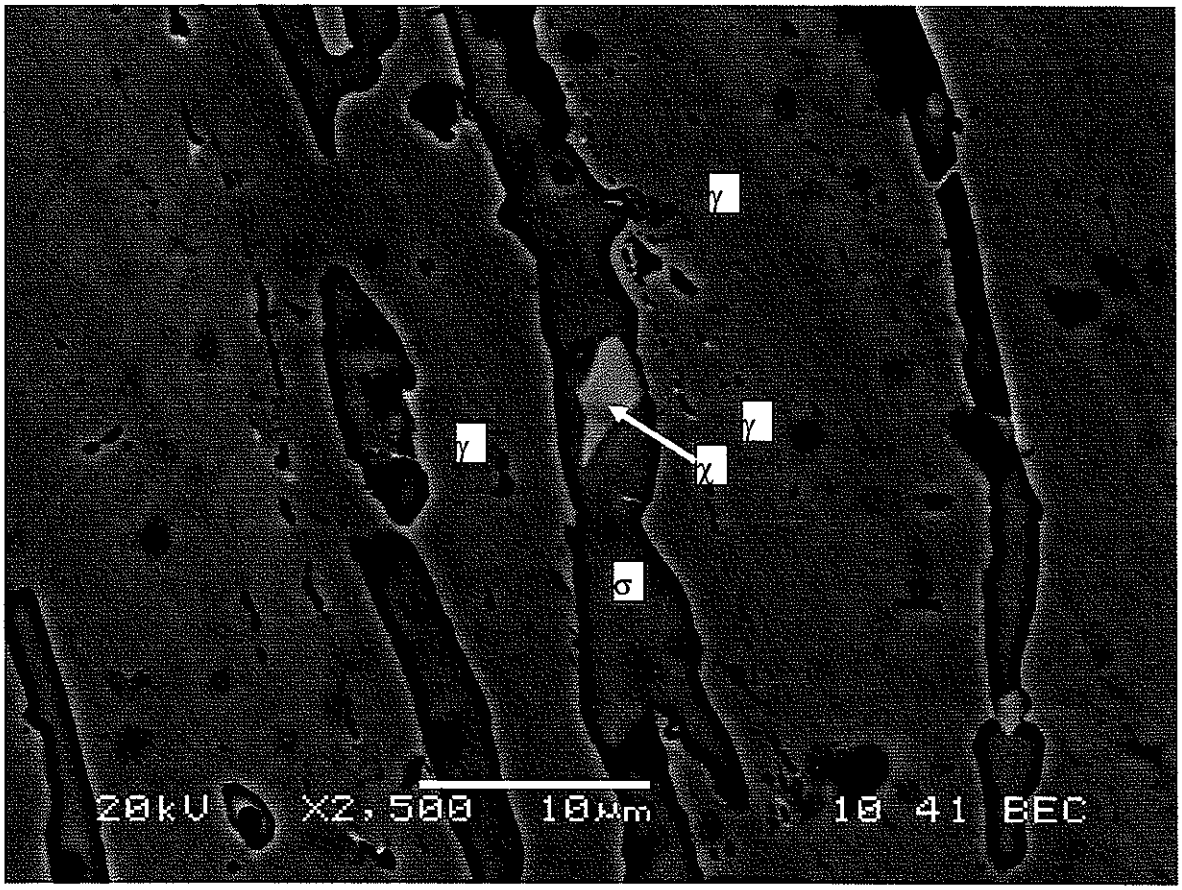

Fig. 58. SEM backscattered electron micrograph of Heat 4 annealed at 825°C. Contrast difference can be seen between σ and χ. EDS scanning assured the brighter phase as χ enveloped by σ.

Table 18. EDS results (in wt.%) from intermetallic phases at its maximum formation temperature.

Alloys	Phase at $T_{max.}$	Fe	Cr	Mo	Ni	Mn	Si
CD3MN	Sigma	57.62 ±0.13	30.19 ±0.10	7.84 ±0.11	2.87 ±0.07	0.50 ±0.06	0.94 ±0.03
HEAT 1	Chi	57.98 ±0.15	21.98 ±0.09	16.26 ±0.14	2.01 ±0.07	0.74 ±0.06	0.81 ±0.03
HEAT 2	Sigma +Chi	56.89 ±0.15	25.43 ±0.10	12.73 ±0.13	3.00 ±0.08	0.86 ±0.07	0.99 ±0.04
HEAT 3	Sigma	56.78 ±0.14	28.26 ±0.10	9.08 ±0.12	3.62 ±0.08	0.81 ±0.07	1.32 ±0.04
HEAT 4	Sigma	62.59 ±0.18	34.34 ±0.13	6.91 ±0.15	3.84±0.10	1.02±0.08	1.29 ±0.05
HEAT 5	Sigma	57.81 ±0.13	30.64 ±0.10	6.62 ±0.11	2.90 ±0.07	0.88 ±0.07	1.15 ±0.03
HEAT 6	Heat 6 is the same alloy as Heat 5.						
HEAT 7	Sigma +Chi	61.45 ±0.13	25.78 ±0.09	8.22 ±0.11	2.70 ±0.07	0.86 ±0.06	0.99 ±0.03
HEAT 8	Sigma	52.40 ±0.18	29.19 ±0.12	10.22 ±0.13	4.24 ±0.08	0.63 ±0.07	0.89 ±0.04

To determine whether composition variations in the casting were responsible for the discrepancies, a composition profile of the cast alloys after solution heat treatment was obtained using wavelength dispersive spectrometry (WDS), and the results are shown in Fig. 59. The scan was positioned so as to traverse four δ/γ interphase boundaries. The profiles appear quite good, with only a slight scattering of Cr detected across the sample. A slight enrichment of Ni and depletion of Cr was detected within the γ near the δ/γ boundary. Since the intermetallic phases were always seen to nucleate and grow within the δ grains this slight variation is not expected to be significant. However, it may indicate that kinetics override thermodynamic considerations and produce local fluctuations in the cast alloys that may cause discrepancy between the equilibrium calculations using *Thermo-Calc* and the experimental results.

To study the affect kinetics may have on initial phase formation, the program DICTRA (Diffusion Controlled Transformations) was used to predict the diffusion profiles expected to exist around σ and χ precipitates in the absence of the other phase. As shown in Fig. 60 the profiles are almost identical, indicating both phases have similar formation kinetics. Thus, kinetics do not appear to be the controlling factor in determining which phase is observed initially. Given these results it was determined that the minor alloying elements present, namely Si, N, W, and Cu, which had been ignored in the designed experiment and in initial *Thermo-Calc* simulations likely play an important role in affecting the balance between σ and χ formation.

Figures 61 and 62 show *Thermo-Calc* results for an alloy based on the CD3MN composition and in which the major alloying elements Cr, Mo, and Ni have been varied $\pm 10\%$ relative to the nominal base composition. In general the predicted shifts in equilibrium

amounts and formation temperature agree with observations of the alloys of the designed experiments, i.e., Cr and to a lesser extent Ni favors σ formation while Mo favors χ. In both cases the maximum formation temperatures are consistently lower than what was observed experimentally. It should also be noted that while the relative amount of alloying variation is only ± 10%, the absolute differences in alloying amounts are quite substantial e.g. ± 2.2 wt% Cr, 0.5 wt% Ni and 0.3 wt% Mo, and these variations are much greater than are typically allowed for in specifications. When the minor alloying elements of Si and N are considered, the situation is much different when one considers the effect of the element within specified range. Examples of the effect produced on σ and χ formation are presented in Figs. 63 and 64, where N was varied from zero percent up to within the nominal limits of 0.10 to 0.30 wt.% and Si was varied up to a maximum of 1.00 wt.%. These plots show that increasing N decreases σ equilibrium amounts and slightly suppresses maximum formation temperature, while greatly increasing χ formation temperature. A similar effect is seen with increasing Si, with the σ amounts remain fairly constant and the maximum formation temperature dropping; however, χ formation temperature is greatly enhanced. In either case the predicted equilibrium phase shifts dramatically from σ to χ with slight additions of these minor elements, even within nominal limits. Thus, a CD3MN alloy could be well within specifications for composition and still produce different phase assemblages at high temperature depending upon the minor alloying element contents.

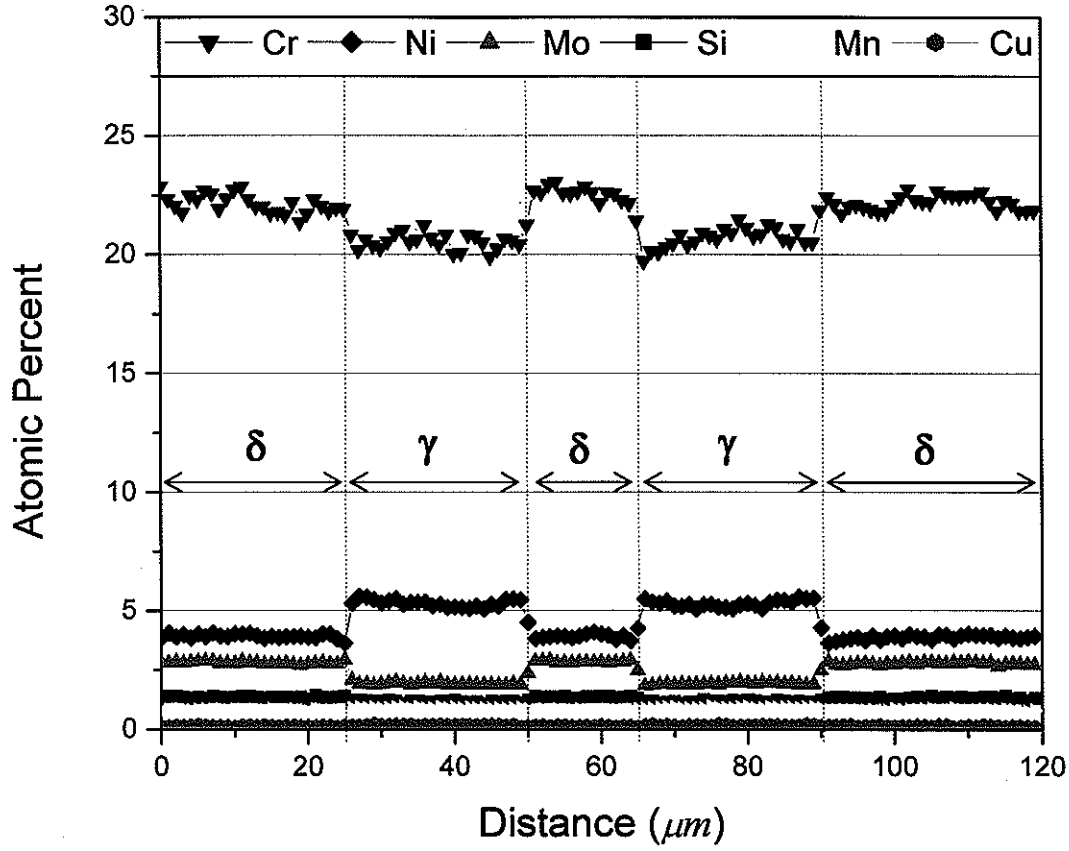

Fig. 59. WDS line scanning of Cr, Ni, Mo, Si, Mn and Cu for Heat 2 as solution heat treated condition.

(a)

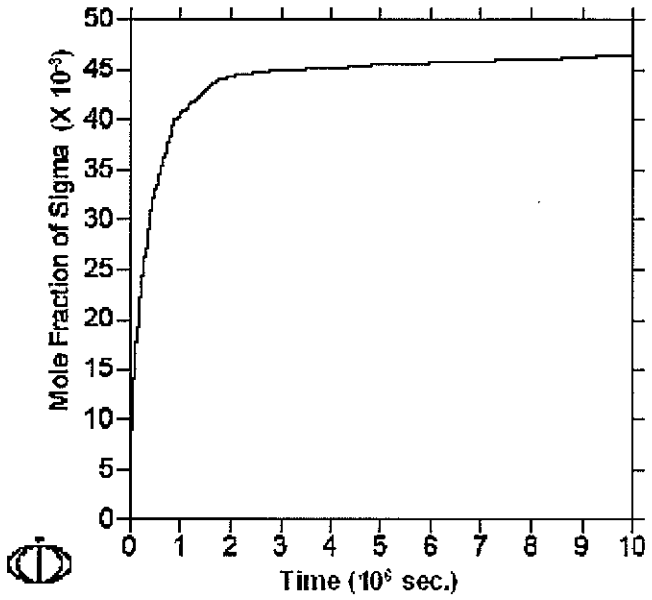

(b)

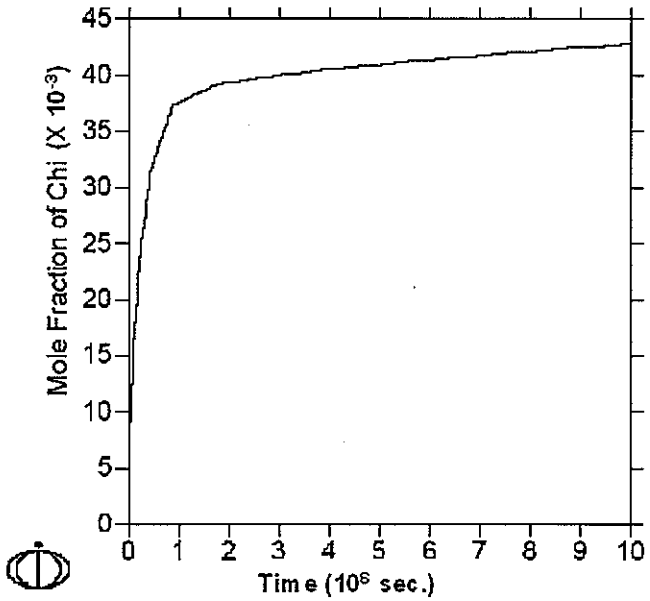

Fig. 60. DICTRA simulations of (a) σ and (b) χ growth rate. Time to achieve equilibrium amount (*i.e.*, maximum) is almost same for both phases.

(a)

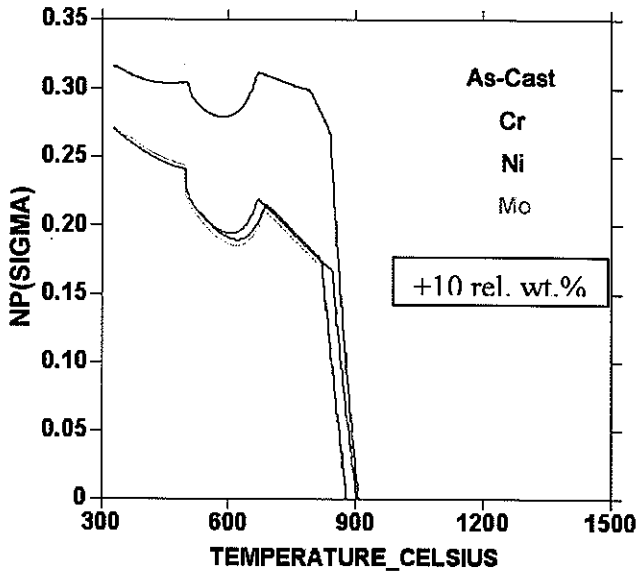

(b)

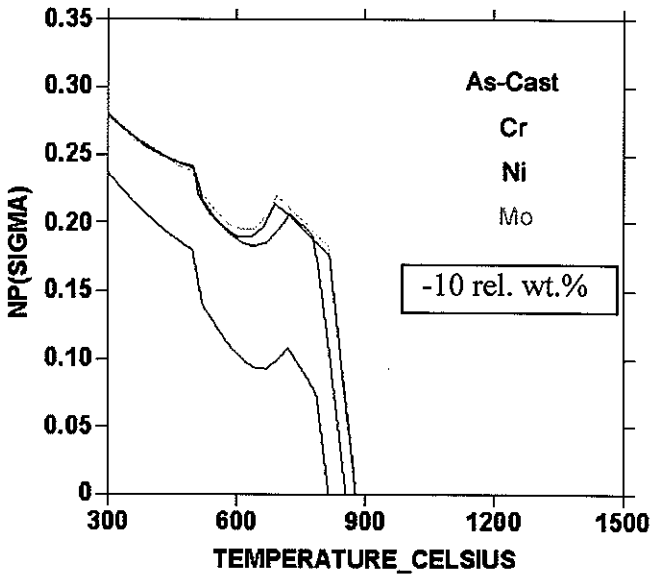

Fig. 61. Mole fraction (NP) of σ phase was plotted with temperature. (a) Each curve was calculated with about 10% relative higher amount of Cr, Ni and Mo and (b) with 10% relative lower amount of Cr, Ni and Mo from nominal composition of CD3MN.

(a)

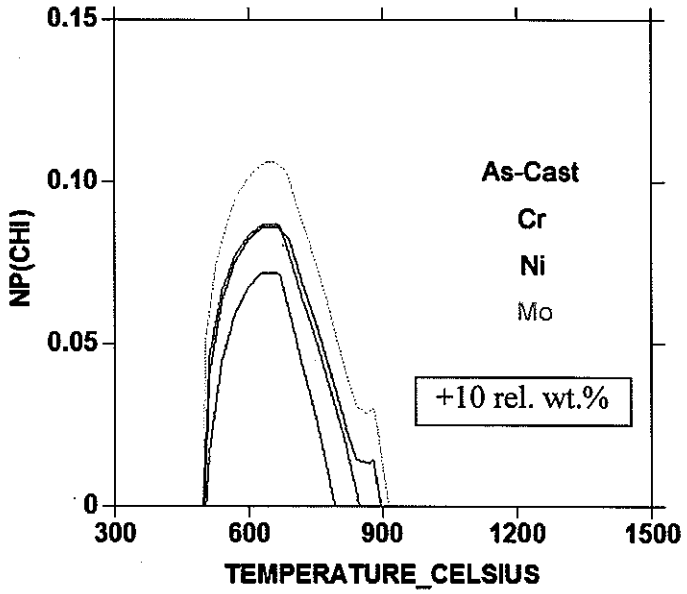

(b)

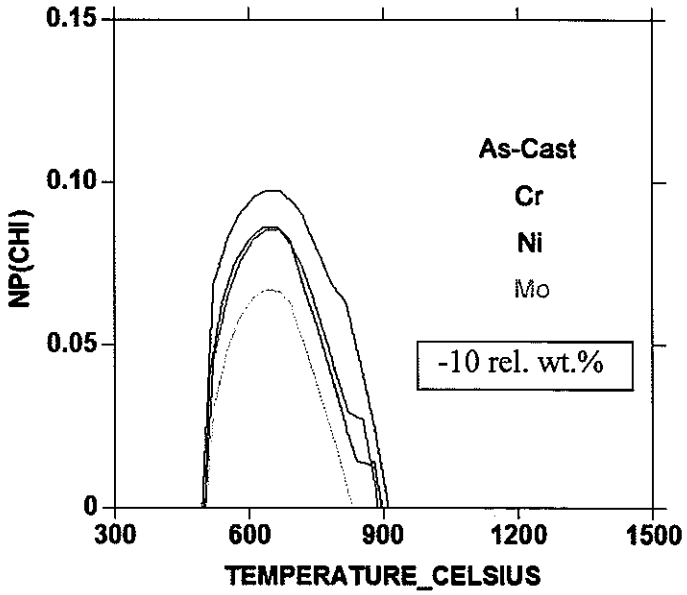

Fig. 62. Mole fraction (NP) of χ phase was plotted with temperature. (a) Each curve was calculated with about 10% relative higher amount of Cr, Ni and Mo and (b) with 10% relative lower amount of Cr, Ni and Mo from nominal composition of CD3MN.

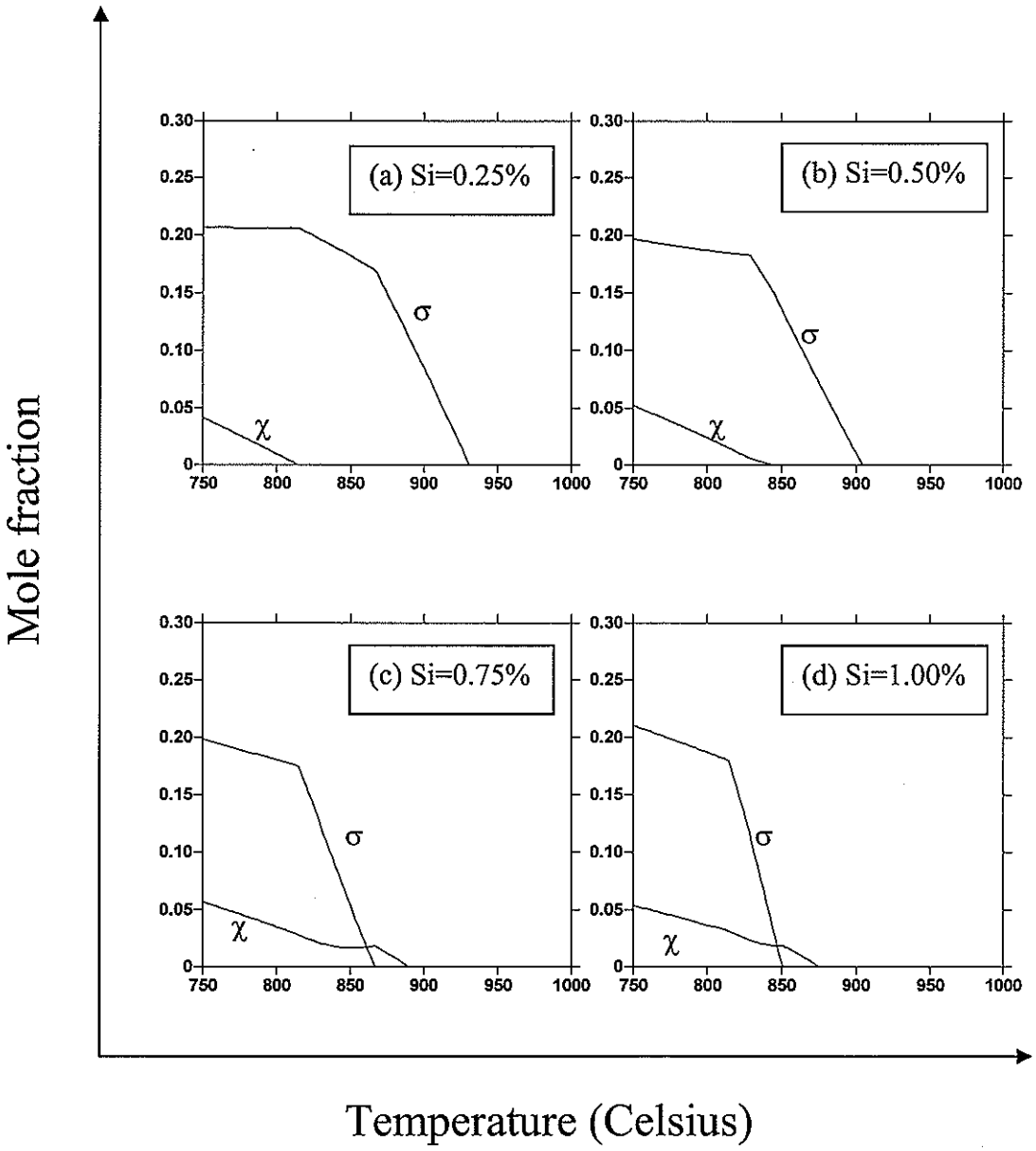

Fig. 63. Mole fraction of σ and χ when Si is added (a) 0.25 %, (b) 0.50 %, (c) 0.75 %, and (d) 1.00 % into CD3MN nominal composition.

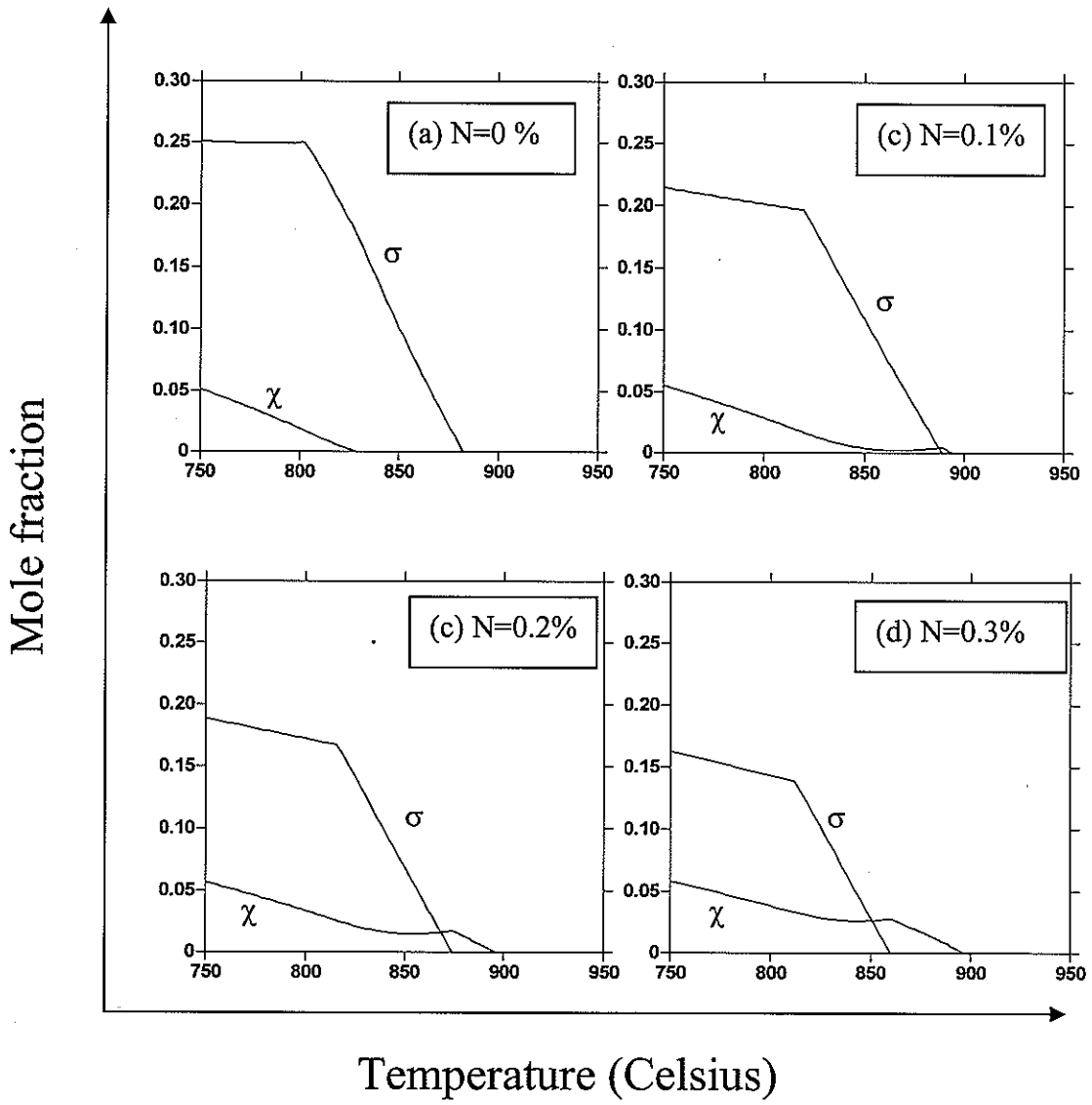

Fig. 64. Mole fraction of σ and χ when N is added (a) 0.25 %, (b) 0.50 %, (c) 0.75 %, and (d) 1.00 % into CD3MN nominal composition.

Given the apparent sensitivity of the alloys systems to minor additions it is interesting to review the compositions present in Heats #1-#8 and compare them again to the experimental observations. Examination of Table 7 shows that Si varies from a minimum of

0.52 in Heat #1 to a maximum of 1.18 in Heat #4, while N is more closely controlled, varying from a low of 0.15 (Heat #2) to a maximum of 0.21 (Heat #5). Heats #1 and #4 have similar N contents, being 0.17 and 0.15, respectively. It is seen in Table 17 that Heat #1 is predicted to have χ form initially, as was found experimentally. By contrast, Heat #4 is also predicted to have χ form initially (presumably due to the effect of high Si even though the Mo content is low) but σ was found experimentally. Both Heats #4 and #5 have similar Mo amounts, but Heat #4 is high in Si and low in Cr and N while Heat #5 is high in Cr and N and low in Si. Heat #4 is predicted to form χ initially, while Heat #5 is predicted to form σ. Given the relative balance of σ and χ stabilizers this prediction would seem to make sense. However, both heats possess σ as the initial phase. Thus, a complex balance exists between σ and χ stabilizers and the near identical thermodynamic and kinetic driving forces that exist for both phases result in experimental observations frequently varying from predictions.

It should be noted that Heat #4 has a higher Ni content, which is predicted to be a σ stabilizer even though Ni is not a major component of the σ or χ compositions, and this may be an additional factor explaining the reason that χ is often not observed to be the initial phase. It is interesting to note that in every heat with high Ni, σ is observed to be the first to form rather than χ. This may indicate that while Ni is not integral to the σ or χ structures it does change the γ / δ ratio and compositions, which may affect phase nucleation of σ or χ. The effect of Ni variation on the formation of the intermetallic phases was not fully understood.

Despite the discrepancies noted above, *Thermo-Calc* calculations can agree reasonably well with experimental results if certain limitations are understood. For example,

consider Fig. 65 which compares a *Thermo-Calc* calculation for the CD3MN alloy in the range 750°C to 950°C to a typical SEM picture taken at 850°C after extended (30 days) heat treatment. At first glance the ratio of predicted phases appears incorrect, with more δ being predicted than σ (≈ 23 mole% vs 8 mole%), which clearly disagrees with observations. However, it must be remembered that *Thermo-Calc* consistently underestimates the formation temperature of phases when compared to experimental observations. For the case of CD3MN, phase precipitation is observed to be approximately 50 degrees higher than predicted. If the curves of Figure 65 (b) were shifted to higher temperatures, to more accurately reflect observations, a much closer agreement would be obtained between experiment and prediction. For example, a 25 degree shift would mean that the predicted phase amounts at 850°C would lay approximately along line B (arrowed in Fig 65 (b)) rather than line A. At this point the observed phase percentages match quite well with predicted amounts. Also note that in Fig. 65 (a), numerous precipitates of χ are observed inside σ regions. Thus, while sigma may have formed first overall, in many specific nucleation locations χ forms initially followed by growth of σ, again in agreement with predictions.

In order to shift curves to higher temperature, it is necessary to modify interaction parameters in the database (TCFE3) used. At present, the *Thermo-Calc* databases have not been fully evaluated for σ and χ phases in the high alloyed steel systems such as DSS, and any modifications and/or assessments may be needed.

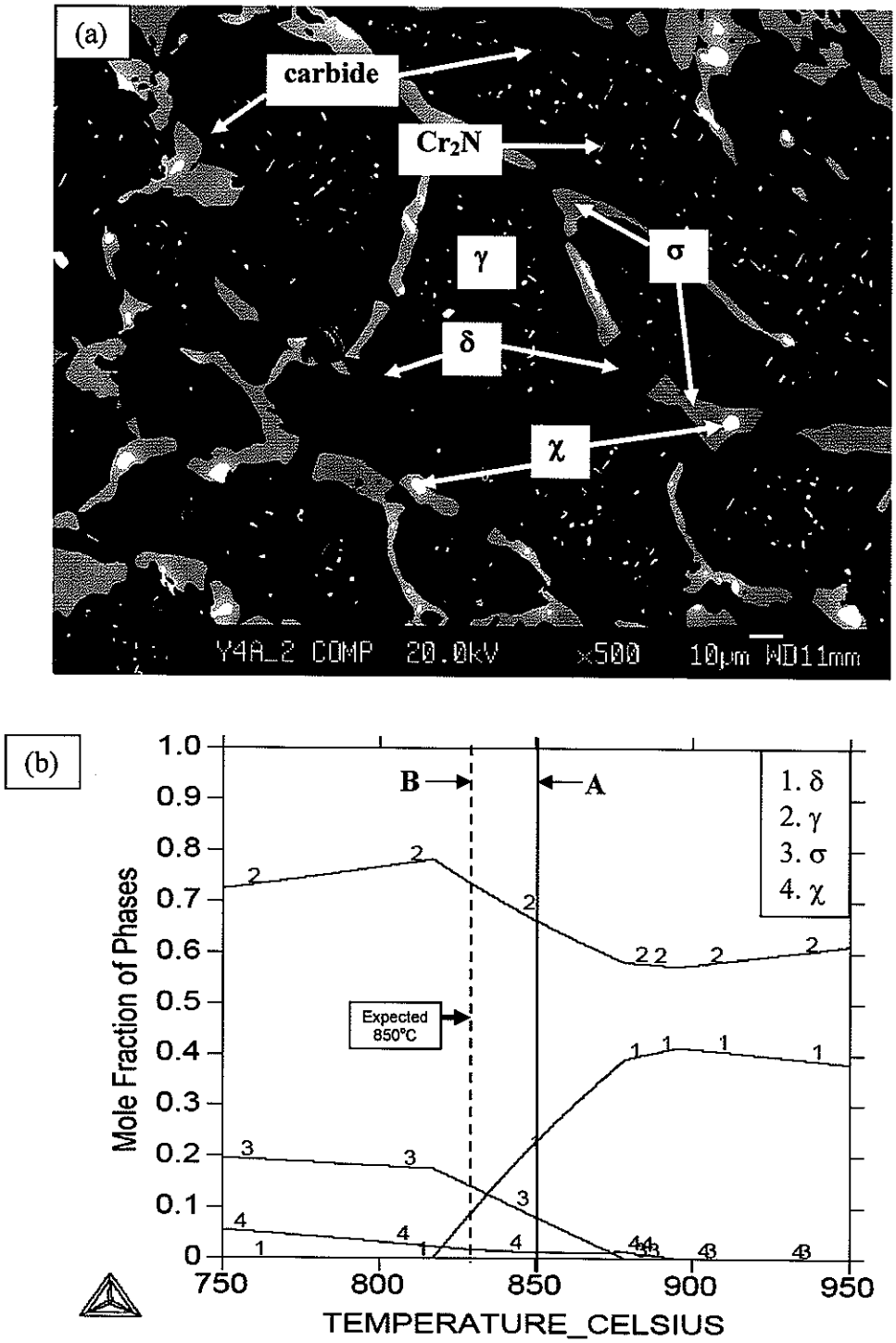

Fig. 65. (a) SEM/BSE micrograph of CD3MN taken at 850°C after 30-day heat treatment, (b) corresponding *Thermo-Calc* calculation.

CHAPTER 9. GENERAL CONCLUSIONS

The findings from this study alloy the following conclusions to be made.

1. TTT curves developed for CD3MN and CD3MWCuN show that the kinetics and extent of intermetallic formation were much greater in CD3MWCuN than in CD3MN. For both steels intermetallic formation takes place in the approximate temperature range 700 - 1000°C, with the kinetics being fastest at about 850°C. In CD3MN, intermetallic formation reaches the 5 vol% level, where mechanical properties start to be affected, after about 1500 minutes while in CD3MWCuN this occurs in only about 20 minutes.

2. The secondary phases σ and χ formed owing primarily to the migration of Cr and Mo in the steel. At equilibrium, i.e., after a long term annealing, σ phase is the predominant intermetallic, with minor amounts of χ. Sigma is rich in Cr, approximately 31 wt.%, while χ phase is rich in Mo, approximately 16 wt.%. Both phases seem to form at approximately the same time.

3. Phase identification of various types of secondary phases was carried out using transmission electron microscopy (TEM). The phases identified include γ, δ, σ, χ, $Cr_{23}C_6$ and Cr_2N.

4. Comparison of TTT diagrams of cast DSS to wrought counterpart DSS indicates that the intermetallic phase transformation is slower in the cast alloys than in counterpart wrought

alloys. This is believed to be due primarily to the difference in nominal compositions and microstructures between wrought and cast alloys.

5. CCT diagrams of cast duplex stainless steels CD3MN and CD3MWCuN have been determined mathematically and compared to experimental results. Observations in CD3MN and CD3MWCuN show good agreement with theoretical calculations as regards curve position. The rapid transformation rate and dual phase morphology of intermetallic phase formation in CD3MWCuN indicates kinetic factors dominate in this system, causing deviation from predicted equilibrium amounts.

6. Results from hardness tests for both alloys were found to correlate with the amount of intermetallic phase. If intermetallic phase reaches 5 vol. %, hardness was shown to increases substantially, as had been previously reported.

7. Kinetics of intermetallic phase formation in the two cast DSS studied during continuous cooling were found to be slower than their wrought counterpart alloys, similar to previously reported results concerning isothermal transformations. It is speculated that slight differences in composition and microstructure play a role in intermetallic phase precipitation.

8. Calculation of phase equilibria using *Thermo-Calc* and the TCFE3 database does not completely agree with experimental results. Observed formation temperatures are consistently higher than predicted and the predicted initial intermetallic to form (χ or σ) is not consistently observed.

9. Alloying variations may play a significant role in the formation of intermetallic phases. Cr and Ni promote σ, and Mo promotes χ. Minor alloying additions, especially Si and N may play a large role in determining the equilibrium phase at high temperature.

10. Further optimization of thermodynamic variables using such database is still required for cast DSS systems.

REFERENCES

1. J. Charles, "Proc. Conf. Duplex Stainless Steel '91", Beaune, France, Les editions de physique, Vol. 1, 1991, pp. 3-48.

2. W. F. Smith, "Structure and Properties of Engineering Alloys", New York, NY, McGraw-Hill, 1993, 2nd Ed.

3. T. B. Massalski (Ed.), "Binary Alloy Phase Diagram", Metals Park, OH, American Society for Metals, Vol. 1, 1986.

4. R. W. K. Honeycombe, "Steels: Microstructure and Properties", Metals Park, OH, American Society for Metals, 1981.

5. K.G. Budinski, "Engineering Materials: Properties and Selection", Englewood Cliffs, NJ, Prentice Hall, 1996, 3rd Ed.

6. J. R. Davis (Ed.), "ASM Specialty Handbook: Stainless Steels", Materials Park, OH, ASM International, 1994.

7. J. W. Pugh, J. O. Nisbet, Transactions of American Institute of Metallurgical and Petroleum Engineers, Vol. 188, 1950, pp. 268-276.

8. J. L. Walter, M. R. Jackson, C. T. Sims (Ed.), "Alloying", Metals Park, OH, American Society for Metals, 1988.

9. P. Shewmon, "Diffusion in Solids", Warrendale, PA, TMS, 1989, 2nd Ed.

10. C. R. Barrett, W. D. Nix, A. S. Tetelman, "The Principles of Engineering Materials", Englewood Cliffs, NJ, Prentice-Hall, 1973.

11. J. D. Verhoeven, "Fundamentals of Physical Metallurgy", New York, NY, John Wiley and Sons, 1975.

12. D. A. Porter, K. E. Eastering, "Phase Transformations in Metals and Alloys", London, UK, Chapman and Hall, 1992, 2nd Ed.

13. J. W. Cahn, Acta Metallurgica, Vol. 4, 1956, pp. 449-459.

14. J. W. Christian, "The Theory of Transformations in Metals and Alloys, Part 1: Equilibrium and General Kinetic Theory", New York, NY, Pergamon, 1975, 2nd Ed.

15. J. -C, Zhao, M. R. Notis, Materials Science and Engineering R, Vol. 15, 1995, pp. 135-208.

16. R. Ferragut, A. Somoza, I. Torriani, Materials Science and Engineering A, Vol. 334, 2002, pp. 1-5.

17. S. Beckman, B. A. Cook, M. Akinc, Materials Science and Engineering A, Vol. 299, 2001, pp. 94-104.

18. R. E. Reed-Hill, R. Abbaschian, "Physical Metallurgy Principles", Boston, MA, PWS Pub., 1994, 3rd Ed.

19. J. W. Cahn, Acta Metallurgica, Vol. 4, 1956, pp. 572-575.

20. A. Wilson, J. O. Nilsson, Scandinavian Journal of Metallurgy, Vol. 25, 1996, pp. 178-185.

21. J. -L. Lee, H. K. D. H. Bhadeshia, Materials Science and Engineering A, Vol. 171, 1993, pp. 223-230.

22. M. Venkatraman, O. N. Mohanty, R. N. Ghosh, Scandinavian Journal of Metallurgy, Vol. 30, 2001, pp. 8-13.

23. Z. Zhang, R. A. Farrar, "An Atlas of Continuous Cooling Transformation (CCT) Diagrams Applicable to Low Carbon Low Alloy Weld Metals", London, UK, Institute of Materials, 1995.

24. A. B. Cota, P. J. Modenesi, R. Barbosa, D. B. Santos, Scripta Materialia, Vol. 40, 1999, pp. 165-169.

25. A. Zarei Hanzaki, R. Pandi, P. D. Hodgson, S. Yue, Metallurgical Transactions A, Vol. 24, 1993, pp. 2657-2665.

26. D. Q. Bai, S. Yue, T. M. Maccagno, J. J. Jonas, Matallurgical and Materials Transactions A, Vol. 29, 1998, pp. 989-1001.

27. Malcolm Blair (Ed.), "Duplex Stainless Steels: A State-of-the-Art Literature Review", Crystal Lake, IL, Steel Founders' Society of America, 2001.

28. R. N. Gunn (Ed.), "Duplex Stainless Steels: Microstructure, Properties and Applications", Abington Publishing, 1997.

29. J. -O. Nillson, P. Kangas, T. Karlsson, Q. Wilson, Metallurgical and Materials Transactions A, Vol. 31, 2000, pp. 35-45.

30. E. M. Johnson, Master of Science Thesis in Iowa State University, Ames, IA, 2002.

31. Y. H. Lee, K. T. Kim, Y. D. Lee, K. Y. Kim, Materials Science and Technology, Vol. 14, 1998, pp. 757-764.

32. R. A. Lula (Ed.), "Proc. Conf. Duplex Stainless Steels '83", Metals Park, OH, American Society for Metals, Vol. 1, 1983, pp. 693-756.

33. H. D. Solomon, T. M. Devine in ASTM, STP 672, 1979, pp. 430-461.

34. B. Josefsson, J. O. Nilsson, A. Wilson, "Proc. Conf. Duplex Stainless Steel'91", Beaune, France, Les Editions de Physique, Vol. 1, 1991, pp. 67-78.

35. X. G. Wang, D. Dumortier, Y. Riquier, "Proc. Conf. Duplex Stainless Steel'91", Beaune, France, Les Editions de Physique, Vol. 1, 1991, pp. 127-134.

36. E. M. Johnson, Y. -J.Kim, L. S. Chumbley, B. Gleeson, Scripta Materialia, Vol. 50, 2004, pp. 1351-1354.

37. N. Saunders, A. P. Miodownik, "CALPHAD (Calculation of Phase Diagrams), A Comprehensive Guide" Pergamon Materials Series, Oxford, UK, Elsevier, Vol. 1, 1998.

38. J. -O. Andersson, T. Helander, L. Hoglund, P. Shi, B. Sundman, Calphad, Vol. 26, 2002, pp. 273-312.

39. K. M. Lee, H. S. Cho, D. C. Choi, Journal of Alloys and Compounds, Vol. 285, 1999, pp.156-161.

40. T. H. Chen, J. R. Yang, Materials Science and Engineering A, Vol. 311, 2002, pp. 28-41.

41. Y. S. Sato, H. Kokawa, Scripta Materialia, Vol. 40, 1999, pp. 659-663.

42. Y. Maehara, M. Koike, N. Fujino, T. Kunitake, Trans ISIJ, Vol. 23, 1983, pp. 240-246.

43. A. Gregori, J. -O. Nilsson, Metallurgical and Materials Transactions A, Vol. 33, 2002, pp. 1009-1018.

44. M. Ceylan, V. Kuzucu, M. Aksoy, I. Aksoy, M. Kaplan, M.M. Yildirim, Journal of Materials Processing Technology, Vol. 69, 1997, pp. 238-246.

45. V. Kuzucu, M. Ceylan, M. Aksoy, I. Aksoy, M. Kaplan, Journal of Materials Processing Technology, Vol. 69, 1997, pp. 247-256.

46. E. L. Brown, T. A. Whipple, G. Krauss, "Proc. Conf. Duplex Stainless Steel '91", Beaune, France, Les editions de physique, 1991, Vol. 1, pp. 665-691.

47. J. A. Jimenez, M. Carsi, O. Ruano, F. Penalba, Journal of Materials Science, Vol. 35, 2000, pp. 907-915.

48. J. Li, T. Wu, Y. Riquier, Materials Science and Engineering A, Vol. 174, 1994, pp. 149-156.

49. S. Bugat, J. Besson, A. F. Gourgues, F. N'Guyen, A. Pineau, Materials Science and ngineering A, Vol. 317, 2001, pp. 32-36.

50. T. H. Chen, K. L. Weng, J. R. Yang, Materials Science and Engineering A, Vol. 338, 2002, pp. 259-270.

51. T. Kuroda, K. Nakade, K. Ikeuchi, Welding in the World, Vol. 44, 2000, pp.17-22.

52. B. J. Lee: Pohang University of Science and Technology, Pohang, Korea, Private communication, 2004.

53. X. Li, A. P. Miodownik, N. Saunders, Materials Science and Technology, Vol. 18, 2002, pp. 861-868.

54. A. J. Ramirez, J. C. Lippold, S. D. Brandi, Metallurgical and Materials Transactions A, Vol. 34, 2003, pp. 1575-1597.

55. S. -B. Kim, K. -W. Paik, and Y. -G. Kim, Materials Science and Engineering A, Vol. 247, 1997, pp. 67-74.

56. Y. -J.Kim, L. S. Chumbley, B. Gleeson, Metallurgical and Materials Transactions A, in press, 2004.

57. Y. -J.Kim, L. S. Chumbley, B. Gleeson, Metallurgical and Materials Transactions A, submitted, 2004.

58. M. E. Wilms, V. J. Gadgil, J. M. Krougman and F. P. Ijsseling, Corrosion Science, Vol. 36, 1994, pp. 871-875.

59. A. Proult, A. Redjaimia, P. Donnadieu, Journal de Physique IV, Vol. 6, 1996, pp. C2-135-140.

60. J. -O. Andersson, N. Lange, Metallurgical and Materials Transactions A, Vol. 19, 1988, pp. 1385-1394.

61. M. Avrami, Journal of Chemical Physics, Vol. 7, 1939, pp. 1103-1112.

62. M. Avrami, Journal of Chemical Physics, Vol. 8, 1940, pp. 212-224.

63. M. Avrami, Journal of Chemical Physics, Vol. 9, 1941, pp. 177-184.

64. E. Scheil, Archiv für das Eisenhüttenwesen, Vol. 8, 1935, pp. 565-567.

65. J. S. Ye, H. B. Chang, T. Y. Hsu, Metallurgical and Materials Transactions A, Vol. 34, 2003, pp. 1259-1264.

66. G. E. Dieter, "Mechanical Metallurgy", London, UK, McGraw-Hill, 1988.

67. P. C. Campbell, E. B. Hawbolt, J. K. Brimacombe, Metallurgical Transactions A, Vol. 22, 1991, pp. 2769-2778.

68. P. C. Campbell, E. B. Hawbolt, J. K. Brimacombe, Metallurgical Transactions A, Vol. 22, 1991, pp. 2779-2790.

69. P. C. Campbell, E. B. Hawbolt, J. K. Brimacombe, Metallurgical Transactions A, Vol. 22, 1991, pp. 2791-2805.

70. T. T. Pham, E. B. Hawbolt, J. K. Brimacombe, Metallurgical and Materials Transactions A, Vol. 26, 1995, pp. 1987-1992.

71. T. T. Pham, E. B. Hawbolt, J. K. Brimacombe, Metallurgical and Materials Transactions A, Vol. 26, 1995, pp. 1993-2000.

72. C. Boppert, A. Schram, "Proc. Conf. Duplex Stainless Steels '94", Glasgow, UK, TWI, Vol. 1, 1994, Paper #74.

73. *Thermo-Calc User's Guide Ver. Q*, Foundation of Computational Thermodynamics, Stockholm, Sweden, 2003.

74. J. A. Cotton, R. D. Knutsen, B. Sundman, Materials Science Forum, Vol. 318-320, 1999, pp. 89-94.

75. G. C. Coelho, J. A. Golczewski, H. F. Fischmeister, Metallurgical and Materials Transactions A, Vol. 34, 2003, pp. 1749-1758.

76. M. Schwind, J. Kallqvist, J. -O. Nilsson, J. Agren, H. -O. Andren, Acta Materialia, Vol. 48, 2000, pp. 2473-2481.

77. J. Sopousek, T. Kruml, Acta Metallurgica, Vol. 35, 1996, pp. 689-693.

78. B. -J. Lee, Metallurgical and Materials Transactions A, Vol. 32, 2001, pp.2423-2439.

79. B. -J. Lee, Calphad, Vol. 16, 1992, pp. 121-149.

80. S. Ranganathan, P. Ramachandrarao, Calphad, Vol. 27, 2003, pp. 39-56.

ACKNOWLEDGEMENT

This work was performed at Ames Laboratory under Contract No. W-7405-Eng-82 with the U.S. Department of Energy. The United States government has assigned the DOE Report number IS-T 2322 to this thesis.